NON-EQUILIBRIUM DYNAMICS FROM FEW- TO MANY-BODY SYSTEMS

A thesis presented in partial fulfillment of the
requirements for the degree of

Doctor of Philosophy
in
Physics

at Massey University, Albany,
New Zealand

Jayson Gutierrez Cosme

2017

Abstract

We study different nonequilibrium phenomena of isolated quantum systems ranging from few- to many-body interacting bosons. Firstly, we have suggested the dynamics of the center-of-mass motion to sensitively detect unconverged numerical many-body dynamics in potential with separable quantum motion of the center of mass. As an example, we consider the time evolution of attractive bosons in a homogenous background and use it to benchmark a specific numerical method based on variational multimode expansion of the many-body wave function - the Multiconfigurational time-dependent Hartree for bosons (MCTDHB). We demonstrate that the simplified convergence criterion based on a threshold value for the least occupied mode function fails to assure qualitatively correct result while our suggested convergence test based on the center-of-mass motion correctly detects the deviation of numerical results from the exact results.

Recent technological progress in manipulating low-entropy quantum states has motivated us to study the phenomenon of interaction blockade in bosonic systems. We propose an experimental protocol to observe the expected bosonic enhancement factor in this blockade regime. Specifically, we suggest the use of an asymmetric double-well potential constructed by superposition of multiple optical tweezer laser beams. Numerical simulations using the MCTDHB method predict that the relevant states and the expected enhancement factor can be observed.

In the second half of the thesis, we have investigated the onset of quantum thermalization in a two-level generalization of the Bose-Hubbard dimer. To this end, the relaxation dynamics following a quench is studied using two numerical methods:

(1) full quantum dynamics and (2) semiclassical phase-space method. We rely on arguments based on the eigenstate thermalization hypothesis (ETH), quantum chaos as seen from the distribution of level spacings, and the concept of chaotic eigenstates in demonstrating equilibration dynamics of local observables in the system after an integrability-breaking quench. The same issue on quantum thermalization can be viewed from a different perspective using semiclassical phase-space methods. In particular, we employ the truncated Wigner approximation (TWA) to simulate the quantum dynamics. In this case, we show that the marginal distributions of the individual trajectories which sample the initial Wigner distribution are in good agreement with the corresponding microcanonical distribution.

Acknowledgments

First of all, I want to thank my supervisor Prof. Joachim Brand for being a wonderful mentor to me. I want to thank him for the countless opportunities that he has given me to pursuit interesting scientific inquiries. Most of all, I am grateful to him for taking his chances on me – a student who came all the way from a relatively obscure third world country.

I would like to thank Dr. Mikkel Andersen and Dr. Christoph Weiss for the research collaborations. I am also thankful to Dr. Alexej Streltsov for providing us access to his MCTDHB-Lab code. I also want to thank Sasha Fialko for introducing to me the topic of quantum thermalization.

I also want to express my gratitude to both current and former members of our group in CTCP for stimulating discussions: Antonio Muñoz-Mateo, Shreya Ghosh, Sasha Fialko, Lauri Toikka, Ulrich Ebling, Peter Jeszenszki, Sophie Shamailov, and Alex Ayet. I also want to thank my officemates: Lukas Wirz, Lukas Trombach, and Morten Piibeleht for providing a nice working environment. I was fortunate enough to play and enjoy table tennis games with the following people: Lukas Wirz, Lukas Trombach, Lukáš Pašteka and Peter Jeszenszki.

I want to specially mention Lukáš Pašteka and Antonio Muñoz-Mateo for all the interesting conversations we had in our coffee breaks. I have found lifelong friends in the two of you. I also want to thank the Raduban family for the special friendship.

I would also like to thank my extended family for their unrelenting support. To my parents, Eduardo and Ma. Teresa Cosme, and to my brother, Jefferson Cosme, thank you for your understanding and for always supporting me.

Most importantly, I want to thank Johnine Cosme for making my life complete. You have sacrificed a lot for me. You gave up everything and dove in headfirst to experience this roller coaster of an adventure with me and for these I am eternally grateful. This thesis is dedicated to you.

Table of Contents

List of Tables

List of Figures

Chapter 1

Introduction

The main theme of this thesis is nonequilibrium quantum dynamics of interacting bosons. In particular, we are interested in coherent quantum dynamics wherein the time evolution of the system is simply governed by the famous Schrödinger equation. These kinds of theoretical exploration are motivated by technological progress in the field of ultracold atoms. Nowadays, it has become a rather standard procedure for relevant experiments in ultracold gases to have high isolation and precise control over physical parameters. In this thesis, we have utilized the so-called the Multi-configurational Time-dependent Hartree for Bosons or MCTDHB to simulate various quantum many-body nonequilibrium problems. High degree of isolation of ultracold gases makes it possible to formulate fundamental questions about quantum statistical mechanics and quantum thermodynamics. An important question in this context is whether, and if so how, statistical properties arise during the coherent evolution in an isolated quantum system. The second half of this thesis aims to contribute in this expanding field by considering the thermalization dynamics in a one dimensional double-well trap. Let us now give a brief historical background on developments in the field of ultracold atoms that are relevant to this thesis.

In his seminal papers published in 1924 [1] and in 1925 [2], Einstein put forward a theory that describes the statistics of a system of noninteracting identical particles with integer spin. These works are extensions of an earlier work done by Bose in

1924 [3]. As such, indistinguishable particles with integer spin are now commonly called as *bosons*. Einstein has predicted that a large fraction of bosons condense and occupy the same quantum state when the system is cooled down below a critical temperature. This state of matter is now known as a Bose-Einstein condensate (BEC). Only seventy years later in 1995 the first BECs were experimentally observed by Cornell and Wieman using ^{87}Rb atoms [4] and, shortly thereafter, by Ketterle using ^{23}Na atoms [5]. The work of these three people for realizing the first-ever BEC culminated with being awarded the Nobel prize in Physics in 2001. The reason for this several decades worth of delay has to do with the fact that the particles in realistic set-ups of various experiments are actually interacting. This is in contrast to the system of noninteracting but nevertheles thermalizing bosons considered in the earlier prediction of Einstein. Eventually, this experimental challenge was solved by using dilute gases. With low densities, however, the critical temperature needed for condensation becomes lower as well. And as such, the techniques for cooling down atoms were needed to be developed first before any further progress could be made towards realizing the first BEC. The necessary technological advancement happened around the 1980s when laser cooling and magneto-optical traps (MOT) were developed for neutral atoms. For their work in laser cooling, Chu, Cohen-Tannoudji, and Phillips received the Nobel prize in Physics in 1997. These laser cooling techniques together with evaporative cooling were then later on used by Wieman, Cornell, and Ketterle to reach the critical temperature needed to observe a BEC.

Recently, both experimental and theoretical efforts have been devoted in advancing the field of ultracold atoms [6]. High tunability of experimental conditions makes ultracold atomic system an attractive option as a test-bed for both novel and well-established quantum phenomena. Specifically, for the study of coherent time-evolution of quantum many-body system, ultracold atoms can provide situations where a system is well-isolated from possible decoherence induced by the environment. The coherence time of such systems is long enough to observe interesting dynamical phenomena within short timescales. Another interesting property of cold

atoms is the possibility of trapping them in optical lattices or multi-well potentials constructed from appropriate superpositions of laser light. Furthermore, the strength and the sign of the interparticle interactions can be tuned by magnetic fields due to the presence of Feshbach resonances [7, 8]. An example of how these techniques can be collectively applied to study interesting properties of cold atomic system is the experimental work by Greiner *et al.* on the superfluid-to-Mott-insulator transition in a repulsively interacting BEC trapped in a three-dimensional optical lattice [9]. In the same year, Greiner *et al.* have also studied in one of the earlier experimental works on coherent quantum dynamics the oscillations of phase coherence as a BEC is quenched from the superfluid to the Mott-insulating regime [10]. It has become a standard procedure to compare results of optical lattice experiments with the theoretical predictions of the Bose-Hubbard model which is the tight-binding limit of the continuous system in the presence of a periodic potential [11]. Controllability in ultracold gases has come a long way since then, and nowadays it has become feasible to reliably trap and cool down a single neutral atom as experimentally demonstrated by Grünzweig *et al.* [12]. Such technological advancements in manipulating low-entropy quantum states have opened up the door for studying the emergence of many-body effects in a bottom-to-top approach [13,14]. This motivated us to study in this thesis one specific phenomenon called the interaction blockade, which can be observed in few bosons. Another interesting phenomenon in coherent quantum dynamics is the concept of equilibration and thermalization. In the pioneering experiment done by Kinoshita *et al.*, the absence of thermalization in a quasi-one-dimensional integrable system was observed [15] which then motivated the recent outburst of both theoretical and experimental explorations aimed to understand quantum ergodicity. An important theoretical work in this subject is the numerical experiments done by Rigol *et al.* on the eigenstate thermalization hypothesis and its application to a system of hard-core bosons [16]. The last half of this thesis is devoted to similar numerical experiments investigating this hypothesis and its possible connection to semiclassical concepts for a system of interacting bosons in a one dimensional double-well confinement.

1.1 Outline of this thesis

This thesis is organized as follows. In Chapter 2, we give a brief review of essential theoretical background on ultracold bosons. We first introduce the basic concepts on Bose-Einstein condensation. These include the notion of a dilute gas and a short derivation of the Gross-Pitaevskii equation using the Hartree approximation. We then discuss how to derive a corresponding tight-binding or Hubbard-like model for a system of interacting bosons trapped in optical tweezer potentials. The remaining parts of this chapter are devoted to a concise historical and theoretical review of quantum ergodicity. We specifically introduce quantum chaos as viewed from random matrix theory and the eigenstate thermalization hypothesis (ETH) which postulates how a statistical description of observables can dynamically emerge in isolated quantum systems.

In Chapter 3, we present another set of introductory materials about a couple of numerical methods utilized with the aim of capturing quantum effects possibly missed in a mean-field description provided by the Gross-Pitaevskii equation. We first give a partial derivation of the important time-evolution equations in a variational method called the Multiconfigurational time-dependent Hartree for bosons (MCTDHB). Next, we elaborate on basic ideas behind a particular phase-space method called the truncated Wigner approximation.

In Chapter 4, we suggest a sensitive convergence tool to detect unconverged nonequilibrium results of numerical methods. Specifically, the interaction-independence of the center-of-mass variance can be exploited as a convergence test for numerical simulations of interacting bosons trapped in potentials with separable center of mass motion. We demonstrate this new convergence test in numerical results obtained from the MCTDHB method. Our investigation led to an interesting discovery of unconverged yet published results on the dynamical creation of two-hump fragmented soliton-like states. Furthermore, we demonstrate that the usual convergence criterion based on the lowest eigenvalue of the single-particle density matrix fails to detect inconsistencies in the numerical results.

In Chapter 5, we discuss our proposed scheme on how the bosonic enhancement factor in the interaction blockade regime can be experimentally observed. We start with a derivation of the bosonic enhancement factor as predicted from the Bose-Hubbard model. We also obtain an analytical formula which can describe deviations from the expected $\sqrt{N}$ scaling behavior for finite on-site interaction strengths. We then test our proposal of using asymmetric double-well traps to observe the expected enhancement factor. To this end, numerical simulations for up to three interacting bosons are done using the MCTDHB method to obtain the many-body eigenvalues and wave function. Due to pathological problems that may arise in MCTDHB, we also present a careful convergence analysis of our results by showing that the relevant energy splitting remains unaffected as the number of mode functions, the main convergence parameter in MCTDHB, is increased. Our numerical findings based on MCTDHB are in good agreement with an effective Bose-Hubbard model, and suggest that our proposed scheme can be used to observe the expected $\sqrt{N}$ scaling in experiments.

The remaining two chapters are devoted to an exploration of quantum thermalization of interacting bosons trapped in a one dimensional double-well systems. In order to observe equilibration of observable in the system, an additional coupling is introduced between the two lowest levels to break the integrability of the Bose-Hubbard dimer. In Chapter 6, we study quantum thermalization in this system from the point of view of a full quantum mechanical description. That is, we obtain the eigenvalues and eigenstates of the Hamiltonian matrix corresponding to the two-level dimer model or, equivalently, a generalized version of the Lipkin-Meshkov-Glick model. Even though the energy spectrum of the system can be classified as non-chaotic based on requirements from random matrix theory, some of the eigenstates nevertheless exhibit chaotic behavior. Perhaps more important, some parts of the spectrum satisfy the ETH which can explain the dynamical equilibration of the expectation values of the mode occupation number towards microcanonical ensemble predictions. The appearance of prethermalized states is also demonstrated for initial

energies close to the middle of the spectrum.

In Chapter 7, we still study the dynamical problem of thermalization but now in the semiclassical limit of large N for the same system considered in Chapter 6. For large N, the truncated Wigner approximation can be used to simulate quantum dynamics of the observables corresponding to the mode occupation number. Here, we show for initial states that eventually relax and thermalize, that the marginal distribution of the Wigner function spreads out and occupies the available phase space. More importantly, the marginal distribution of the Wigner functions is in good agreement with the relevant ensemble predictions given by the diagonal ensemble, grand-canonical, and microcanonical distribution.

1.2 List of Publications

1. J. G. Cosme, O. Fialko, *Thermalization in closed quantum systems: Semiclassical approach*, Physical Review A, **90**, 053602, (2014). [Ref. [17]]

2. J. G. Cosme, O. Fialko, *Relaxation dynamics of ultracold bosons in a double-well potential: Thermalization and prethermalization in a nearly integrable model*, Physical Review A, **92**, 033607, (2015). [Ref. [18]]

3. J. G. Cosme, C. Weiss, J. Brand, *Center-of-mass motion as a sensitive convergence test for variational multi-mode quantum dynamics*, Physical Review A, **94**, 043603, (2016. [Ref. [19]]

4. J. G. Cosme, M. F. Andersen, J. Brand, *Interaction blockade for bosons in an asymmetric double well*, Physical Review A, **96**, 013616, (2017). [Ref. [20]]

Chapter 2

Theoretical Background

2.1 Bose-Einstein Condensates

In this section, we will discuss important concepts and theories which are commonly used in the study of Bose-Einstein condensates. But before jumping into the more realistic scenario of interacting bosons, let us first consider a simple model of non-interacting bosons with total mass M at a temperature T. Within the grand canonical ensemble, standard statistical mechanics allows us to write down the Bose-Einstein distribution function [21]

$$f(E_\nu, \mu, T) = \left[e^{(E_\nu - \mu)/(k_B T)} - 1\right]^{-1}, \tag{2.1}$$

where E_ν is the single-particle energy of the quantum mechanical state $|\nu\rangle$, μ is the chemical potential, and k_B is the Boltzmann constant. The chemical potential is determined by the number of particles such that

$$N = \sum_\nu f(E_\nu, \mu, T). \tag{2.2}$$

The chemical potential μ can not be larger than the ground state energy E_0 or otherwise the ground state mean occupation becomes negative which is, of course, unphysical. For higher temperatures, μ becomes much less than the ground state energy because the mean occupation number of any state in the system is less than unity.

An exact analytical prediction for such critical temperature can be made for non-interacting bosons and arbitrary dimension d. Equilibrium properties of the system can be calculated from a semiclassical approximation wherein the discrete energy spectrum is treated as a continuum [21]. This semiclassical approximation allows us to replace the sum in Eq. (2.2) with an integral

$$N = \sum_{\nu} f(E_\nu, \mu, T) = \int dE g(E) f(E, \mu, T) \tag{2.3}$$

where $g(E)$ is the density of states. The dependence on the details and dimensionality of the trap is reflected in the density of states $g(E) = C_\alpha E^{\alpha-1}$, where α and C_α are constant parameters that describe the external trap. For free particles in d-dimension, $\alpha = d/2$ while for d-dimensional harmonic confinement, $\alpha = d$. Note that in replacing the sum with integral in Eq. (2.3), the ground-state population of a homogenous gas N_0 is not properly accounted for because $g(0) = 0$ even though in reality N_0 can have a very large value according to Eq. (2.1). For this reason, one needs to exclude the ground state contribution in Eq. (2.3)

$$N = N_0 + \int dE g(E) f(E, \mu, T). \tag{2.4}$$

The number of bosons in the excited states can then be calculated from the integral

$$N_{\text{ex}} = \int_0^\infty dE g(E) f(E, \mu, T). \tag{2.5}$$

Simply from the form of the distribution in Eq. (2.1), it is easy to see that Eq. (2.5) reaches its maximum value for $\mu = 0$. The critical temperature T_c can then be solved by noting that this is precisely the condition at which the total number of bosons can occupy the excited states

$$N = N_{\text{ex}}(T_c, \mu = 0) = \int_0^\infty dE g(E) \left[\exp(E/kT_c) - 1\right]^{-1}. \tag{2.6}$$

The critical temperature T_c is then defined as the highest temperature at which a condensate can form. This equation can be evaluated using gamma $\Gamma(\alpha)$ and Riemann-zeta $\zeta(\alpha)$ functions such that the critical temperature is

$$kT_c = \frac{N^{1/\alpha}}{[C_\alpha \Gamma(\alpha)\zeta(\alpha)]^{1/\alpha}}. \tag{2.7}$$

Below the critical or transition temperature T_c the number of bosons in the excited states is

$$N_{\text{ex}} = C_\alpha \Gamma(\alpha)\zeta(\alpha)(kT)^\alpha. \tag{2.8}$$

Then if we divide this expression with the equation for the transition temperature given by Eq. (2.7)

$$N_{\text{ex}} = N(\frac{T}{T_c})^\alpha, \tag{2.9}$$

such that the remaining bosons must occupy the single-particle ground state $N_0(T)$ with occupation according to

$$N_0(T) = N\left[1 - \left(\frac{T}{T_c}\right)^\alpha\right]. \tag{2.10}$$

The phenomenon of Bose-Einstein condensation can be conceptually understood as the rapid increase in the population of the ground state for $T < T_c$. One signature of Bose-Einstein condensation is the macroscopic occupation of a single quantum state which happens the number of bosons in the ground state is of the same order as the total number of bosons in the system such that $N - N_0(T) \ll N$. In the case of $T = 0$, all of the bosons condense to the ground state and we have complete occupation of a single quantum state. The onset of the condensation process can be understood physically as the point when the de Broglie wavelength

$$\lambda_{\text{dB}} = \sqrt{\frac{2\pi\hbar^2}{Mk_BT}}, \tag{2.11}$$

becomes of the same order as the mean interparticle distance $d = \rho^{-1/3}$, where ρ is the density of the gas.

2.1.1 Dilute Bose gas

Here, we discuss the theory of dilute interacting Bose gases at ultracold temperatures. The Hamiltonian for a system of N interacting identical quantum particles interacting only via two-particle potentials can be written as

$$\hat{H} = \sum_{i=1}^{N}\left[-\frac{\hbar^2}{2m}\nabla_i^2 + V(\mathbf{r}_i, t)\right] + \sum_{i<j}\hat{U}(\mathbf{r}_i - \mathbf{r}_j), \tag{2.12}$$

where $\hat{U}$ is the interaction potential between two bosons. One of the main assumptions for the validity of this form of the many-body Hamiltonian is that we have neglected higher-body interactions in the system. Such assumption can be justified in experiments where the mean particle separation is larger compared to the length scale associated with the two-body interaction potential $\hat{U}$. We can further approximate the actual form of the interaction potential for dilute gasses with sufficiently low energies. At low temperatures around the sub-milliKelvin regime $\sim 10^{-3}$K, the dominant contributions in the two-body scattering processes will come from the lowest angular momentum collisions which are of the s-wave type for bosons [6]. For any finite-range interaction potential defined by some characteristic length scale a_c and if the momentum k is small enough such that $ka_c \ll 1$, one can show that the scattering amplitude $f(k)$ will only depend on the scattering length a_s according to $f(k) = -a_s/(1 + ika_s)$. In this type of scenario as first applied by Fermi for slow-moving neutrons [22] and then by Lee, Huang, and Yang in the context of quantum gases [23,24], a pseudopotential with a regularized contact interaction can be used to explain the underlying physics

$$\hat{U}(\vec{r}) = \frac{4\pi\hbar^2 a_s}{2M_r}\delta(\mathbf{r}_1 - \mathbf{r}_2)\frac{\partial}{\partial r}(r\cdots), \tag{2.13}$$

where $\mathbf{r} = \mathbf{r}_1 - \mathbf{r}_2$ is the relative coordinate and M_r is the reduced mass of two atoms (for the simplest case of having only one species of atom with mass m, $M_r = m/2$.). Feshbach resonances [7] can be utilized to adjust the sign of the s-wave scattering length a_s just like in the case of ^{85}Rb [8]. The interaction is repulsive for positive a_s and it is attractive for negative a_s. The many-body Hamiltonian for a single species of bosonic atoms with mass m using this pseudopotential is

$$\hat{H} = \sum_{i=1}^{N}\left[-\frac{\hbar^2}{2m}\nabla_i^2 + V(\mathbf{r}_i, t)\right] + \frac{4\pi\hbar^2 a_s}{m}\sum_{i<j}\delta(\mathbf{r}_i - \mathbf{r}_j)\frac{\partial}{\partial r}r, \tag{2.14}$$

2.1.2 Gross-Pitaevskii equation

One definition for classifying a generic many-body interacting Bose gas as a BEC is based on the concept of off-diagonal long range order as originally proposed by Penrose

and Onsager [25]. To this end, the single-particle density matrix is introduced

$$\begin{aligned}\rho(\mathbf{r}_1,\mathbf{r'}_1,t) &= \langle\Psi(t)|\hat{\Psi}^\dagger(\mathbf{r'}_1)\hat{\Psi}(\mathbf{r}_1)|\Psi(t)\rangle \\ &= N\int d\mathbf{r}_2 d\mathbf{r}_3\ldots d\mathbf{r}_N \Psi^*(\mathbf{r'}_1,\mathbf{r}_2,\ldots,\mathbf{r}_N,t)\Psi(\mathbf{r}_1,\mathbf{r}_2,\ldots,\mathbf{r}_N,t),\end{aligned} \tag{2.15}$$

where $|\Psi(t)\rangle$ is the many-body state, $\Psi(\mathbf{r}_1,\mathbf{r}_2,\ldots,\mathbf{r}_N,t)$ is the many-body wave function, and $\hat{\Psi}(\mathbf{r})$ is a bosonic field operator that annihilates a boson at position $\mathbf{r}$. The eigenvalues and eigenvectors of the single-particle density matrix are

$$\langle\Psi(t)|\hat{\Psi}^\dagger(\mathbf{r'}_1)\hat{\Psi}(\mathbf{r}_1)|\Psi(t)\rangle = \sum_{k=1} n_k^{\mathrm{NO}}\varphi_k^*(\mathbf{r'}_1)\varphi_k^*(\mathbf{r}_1), \tag{2.16}$$

where $\{n_k^{\mathrm{NO}}\}$ are the eigenvalues (also known as natural occupancies) and $\{\varphi_k(\mathbf{r}_1)\}$ are the eigenvectors (also known as natural orbitals). Normalization of the single-particle density matrix requires $\sum_k n_k^{\mathrm{NO}} = N$. For a BEC the largest natural occupancy has the same order as the total number of particles, i.e., $\max(\{n_k^{\mathrm{NO}}\}) \sim N$. The notion of off-diagonal long-range order (ODLRO) can be introduced by writing the single-particle density matrix as a Fourier transform of the momentum distribution $n(\mathbf{p})$,

$$\rho(\mathbf{r}_1,\mathbf{r'}_1,t) = \frac{1}{V}\int d\mathbf{p} n(\mathbf{p})\exp\left(\frac{i}{\hbar}\mathbf{p}\cdot(\mathbf{r}_1-\mathbf{r'}_1)\right), \tag{2.17}$$

where V is the volume. In homogenous systems, the existence of ODLRO is equivalent to having a BEC. This can be seen as follows. For a uniform gas, the single-particle functions are trivially given by plane wave solutions $\varphi_k(\mathbf{r}) \sim \exp(i\mathbf{p}_k\cdot\mathbf{r}/\hbar)$. An important feature of a BEC is the macroscopic occupation of a single-particle ground state with momentum $\mathbf{p_0} = 0$

$$n(\mathbf{p}) = N_0\delta(\mathbf{p_0}) + \ldots, \tag{2.18}$$

where $N_0 \approx N$ for a BEC. It then immediately follows from Eq. (2.17) that

$$\rho(\mathbf{r}_1,\mathbf{r'}_1,t)_{|\mathbf{r}-\mathbf{r'}|\to\infty} = \frac{N_0}{V} \neq 0. \tag{2.19}$$

This is precisely what it means to have ODLRO present in the system since the single-particle density matrix approaches a non-zero value as $|\mathbf{r}-\mathbf{r'}| \to \infty$.

While true BEC can exist in three-dimensions, the Mermin-Wagner theorem states that off-diagonal long-range order is absent in one dimensional systems both for zero and for finite temperatures. In this thesis, we are mostly interested in a quasi-one dimensional system where the transverse confinement is significantly larger than the longitudinal confinement. Nonetheless, it is possible and successful to use approximations derived for BEC quasi-one dimensional settings even though there is no true BEC in this case. The mean-field approximation according to the Gross-Pitaevskii equation provides a powerful tool in understanding phenomenon observed in quasi-one dimensional experiments. In what follows, we shall derive the Gross-Pitaevskii equation from a variational formulation without any assumption of true condensation in the system.

For weak interactions $g = 4\pi\hbar^2 a_s/m$, we can use the Hartree-Fock ansatz where we assume that all N particles are in the single-particle energy state in order to expand the many-body wave function as a simple product of such single-particle function

$$\Psi(\mathbf{r}_1, \mathbf{r}_2, \ldots, \mathbf{r}_N, t) = \prod_{j=1}^{N} \phi(\mathbf{r}_j, t), \tag{2.20}$$

where $\phi(\mathbf{r}_j, t)$ is the single-particle function. This can be rewritten in terms of the bra and ket notation as

$$|\Psi\rangle = [|\phi\rangle]^N. \tag{2.21}$$

Both the many-body wave function and the single-particle function are normalized to unity, i.e., $\langle\Psi|\Psi\rangle = \langle\phi|\phi\rangle = 1$. Moreover, we assume that the wave function and its first derivative both vanish at the boundaries. Using the method of Lagrange multipliers, we aim to extremize the functional

$$F[\Psi] = \langle\Psi|\hat{H}|\Psi\rangle - \mu\langle\Psi|\Psi\rangle, \tag{2.22}$$

where $\hat{H}$ is the many-body Hamiltonian Eq. (2.14) and μ is the Lagrange multiplier that ensures that $|\Psi\rangle$ is always normalized to unity. We first find the expression for

each term in $\langle\Psi|\hat{H}|\Psi\rangle$. The kinetic energy part is

$$\begin{aligned}\langle E_{\text{kin}}\rangle &= \langle\Psi|\frac{-\hbar^2}{2m}\nabla^2|\Psi\rangle = \sum_{i=1}^{N}\frac{\hbar^2}{2m}\int d\mathbf{r}|\nabla\phi(\mathbf{r},t)|^2 \\ &= \frac{N\hbar^2}{2m}\int d\mathbf{r}|\nabla\phi(\mathbf{r},t)|^2 = \frac{-N\hbar^2}{2m}\int d\mathbf{r}\phi^*(\mathbf{r},t)\nabla^2\phi(\mathbf{r},t).\end{aligned} \tag{2.23}$$

The second term involving the external potential can be easily written as

$$\langle E_{\text{pot}}\rangle = N\int d\mathbf{r}\phi^*(\mathbf{r},t)V(\mathbf{r})\phi(\mathbf{r},t). \tag{2.24}$$

The interaction term is a bit more involved

$$\langle E_{\text{int}}\rangle = \langle\Psi|\frac{g}{2}\sum_{i,j\neq i}^{N}\delta(\mathbf{r}_i-\mathbf{r}_j)|\Psi\rangle. \tag{2.25}$$

Invoking simple combinatorial arguments allows us to identify that there are $\binom{N}{2} = \frac{N(N-1)}{2}$ identical terms in the restricted double sum for the interaction term. Then, we can further simplify Eq. (2.25)

$$\begin{aligned}\langle E_{\text{int}}\rangle &= \frac{N(N-1)}{2}\int d\mathbf{r}_i d\mathbf{r}_j g\delta(\mathbf{r}_i-\mathbf{r}_j)|\phi(\mathbf{r}_j,t)|^2|\phi(\mathbf{r}_i,t)|^2 \\ &= \frac{N(N-1)}{2}\int d\mathbf{r}g|\phi(\mathbf{r},t)|^4.\end{aligned} \tag{2.26}$$

We take the first order variation of the functional F due to infinitesimal change in $\phi(\mathbf{r},t) \to \phi(\mathbf{r},t)+\delta\phi(\mathbf{r},t)$. More importantly, the variation of the functional with respect to the infinitesimal change must vanish, i.e., $\frac{\delta F}{\delta\phi^*(\mathbf{r},t)} = 0$. Each term in the functional gives, respectively,

$$\frac{\delta\langle E_{\text{kin}}\rangle}{\delta\phi^*(\mathbf{r},t)} = -\frac{N\hbar^2}{2m}\int d\mathbf{r}\nabla^2\phi(\mathbf{r},t), \tag{2.27}$$

$$\frac{\delta\langle E_{\text{pot}}\rangle}{\delta\phi^*(\mathbf{r},t)} = N\int d\mathbf{r}V(\mathbf{r})\phi(\mathbf{r},t), \tag{2.28}$$

$$\frac{\delta\langle E_{\text{int}}\rangle}{\delta\phi^*(\mathbf{r},t)} = gN(N-1)\int d\mathbf{r}|\phi(\mathbf{r},t)|^2\phi(\mathbf{r},t). \tag{2.29}$$

For the term with the Lagrange multiplier μ, we have

$$\frac{\delta\langle\Psi|\Psi\rangle}{\delta\phi^*(\mathbf{r},t)} = N\left(\int d\mathbf{r}|\phi(\mathbf{r},t)|^2\right)^{N-1}\int d\mathbf{r}\frac{\delta\phi^*(\mathbf{r},t)}{\delta\phi^*(\mathbf{r},t)}\phi(\mathbf{r},t) \tag{2.30}$$
$$= N\int d\mathbf{r}\phi(\mathbf{r},t).$$

Combining all these terms yields

$$\frac{\delta F}{\delta\phi^*(\mathbf{r},t)} = 0 = \int d\mathbf{r}N\left[\frac{-\hbar^2}{2m}\nabla^2 + V(\mathbf{r}) + (N-1)g|\phi(\mathbf{r},t)|^2 - \mu\right]\phi(\mathbf{r},t). \tag{2.31}$$

The above equality is satisfied when the integrand is zero and this effectively gives us the Hartree equation

$$\frac{-\hbar^2}{2m}\nabla^2\phi(\mathbf{r},t) + V(\mathbf{r})\phi(\mathbf{r},t) + g(N-1)|\phi(\mathbf{r},t)|^2\phi(\mathbf{r},t) = \mu\phi(\mathbf{r},t). \tag{2.32}$$

For large N, we recover the Gross-Pitaevskii equation after replacing the factor in the interaction term $(N-1) \to N$.

2.2 Tight-Binding Model

Let us now proceed to a short introduction of basic concepts on discretized models often described by a Hubbard-like Hamiltonian. The introductory material in this section is particularly useful for the systems studied in Chapters 5, 6, and 7.

2.2.1 Localized wave functions

In solid-state physics, Bloch wave functions are single-particle functions for a system experiencing a spatially periodic potential. These Bloch functions are, in general, delocalized in space but localized wave functions called Wannier functions can be constructed from an appropriate linear superposition of such Bloch functions. The Wannier functions are then localized at each site defined by the minima of the potential. Similar concepts on the use of Wannier functions as a suitable basis for many-body wave function expansion can be applied in the context of ultracold atoms trapped in optical lattice potential as originally done in Ref. [11].

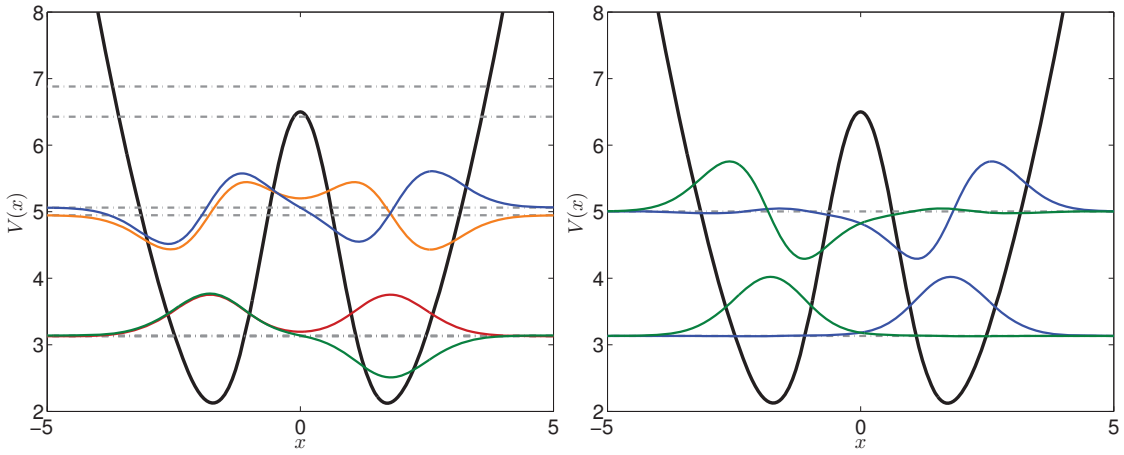

Figure 2.1: Sketch of a double-well potential and its eigenstates and possible localized wave functions.(Left) Four lowest single-particle eigenstates of a double-well potential (black) with their corresponding eigenvalues (dashed-dotted horizontal lines). (Right) Similar to the one on the left but now the localized wave functions are shown. Note that the eigenstates and localized wave functions are offset by the corresponding value of the single-particle energies and on-site energies, respectively.

Although not strictly the same, an analogous approach for constructing localized wave functions can be implemented to describe discretized models for multi-well systems [26]. In particular, consider a double-well potential as shown in Fig. 2.1. The single-particle eigenstates can be obtained denoted by $\{\psi_1, \psi_2, \dots\}$ with the corresponding single-particle energies $\{\epsilon_1, \epsilon_2, \dots\}$. The single-particle Schrödinger equation in this case reads

$$\left(-\frac{\hbar^2}{2m}\nabla^2 + V(\mathbf{r})\right)\psi_j(\mathbf{r}) = \epsilon_j\psi_j(\mathbf{r}), \tag{2.33}$$

where m is the mass of a boson and $V(\mathbf{r})$ is the confining potential. Symmetry restriction dictates that the ground state $\psi_1(\mathbf{r})$ must be an even function of space. On the other hand, the first excited state $\psi_2(\mathbf{r})$ needs to have a node in one the spatial axis indicating an excitation in that direction. This means that the first excited state is antisymmetric or an odd function in the axis of excitation. Note that if the effective barrier separating the left well from the right well is high enough then the two lowest single-particle states are quasi-degenerate, as seen, for example,

in Fig. 2.1. This motivates the use of symmetric and anti-symmetric superposition of the two lowest single-particle functions as a new basis set for representing the many-body Hamiltonian,

$$\phi^0_{\{L,R\}}(\mathbf{r}) = \frac{1}{\sqrt{2}}\left(\psi_1(\mathbf{r}) \pm \psi_2(\mathbf{r})\right). \tag{2.34}$$

Due to the general features of the two lowest single-particle functions as described above, this type of superposition will create a pair of localized wave functions $\phi^0_L(\mathbf{r})$ and $\phi^0_R(\mathbf{r})$ localized in the left well and right well, respectively. This procedure is reminiscent of the aforementioned way of constructing Wannier functions in periodic potentials. It is, of course, possible depending on the system that the remaining high-lying single-particle states become relevant [26]. For example in Fig. 2.1, the energy levels of the second and third single-particle states are both still below the barrier and so it is possible to excite these states for quantum tunneling scenarios with strong enough intra-well interaction couplings. Similar to Eq. (2.34), we can also make symmetric and antisymmetric superpositions of the second and third excited states $\psi_3(\mathbf{r})$ and $\psi_4(\mathbf{r})$, respectively, to construct localized wave functions with higher energies than $\phi^0_{\{L,R\}}(\mathbf{r})$ as shown in Fig. 2.1

$$\phi^1_{\{L,R\}}(\mathbf{r}) = \frac{1}{\sqrt{2}}\left(\psi_3(\mathbf{r}) \pm \psi_4(\mathbf{r})\right). \tag{2.35}$$

2.2.2 Optical potentials

Let us now consider optical dipole potentials generated by either a single or a combination of Gaussian laser beams. The electric field amplitude of such laser beam propagating along the z-direction can be written as [27]

$$|E(r,z)| = \frac{E_0}{\sqrt{1+\left(\frac{z}{z_R}\right)^2}}\exp\left(-\frac{r^2}{w_0^2\left(1+\left(\frac{z}{z_R}\right)^2\right)}\right), \tag{2.36}$$

where r is the radial coordinate, E_0 is the field amplitude, w_0 is the beam waist, and $z_R = \pi w_0^2/\lambda$ is the Rayleigh range with λ as the wavelength of the laser light. For a

single-beam dipole trap described by Eq. (2.36) with the laser frequency far detuned from an optical transition, the ac Stark shift gives rise to a potential of the form [28]

$$V(\mathbf{r}) = -\frac{V}{1+\frac{z^2}{z_R^2}} \exp\left(\frac{-2r^2}{w_0^2(1+\frac{z^2}{z_R^2})}\right). \tag{2.37}$$

In this thesis, we only consider potentials from red-detuned lasers meaning V is positive and corresponds to the maximum depth at the origin. Note that a laser is considered red-detuned if its driving frequency is below the atomic resonance. The opposite of which is called blue-detuned wherein the driving frequency is above the atomic resonance. If we are only interested in low-lying energy states and nonequilibrium phenomenon wherein the edges of the potential are not so relevant, we can expand Eq. (2.37) to lowest order of r and z [28]

$$V(\mathbf{r}) \approx -V + \frac{2V}{w_0^2} r^2 + \frac{V}{z_R^2} z^2, \tag{2.38}$$

where the radial or transverse frequencies are $\hbar\omega_r = \sqrt{8E_{w_0}V}$ and the axial or longitudinal frequency is $\hbar\omega_z = \sqrt{4E_{z_R}V}$, with $E_{w_0} = \hbar^2/(2mw_0^2)$ and $E_{z_R} = \hbar^2/(2mz_R^2)$. This is one way of generating harmonic oscillator potentials for ultracold atoms as seen from the harmonic nature of the effective potential in Eq. (2.38).

Dimensionality plays a vital role as the coupling constant describing two-body collisions can be effectively rewritten depending on the dimensions of the system. For three dimensions, the form of the coupling constant $g = 4\pi\hbar^2 a_s/m$, where a_s is the s-wave scattering length and m is the mass of a boson, is sufficient to capture the relevant physics in the dilute regime. For a quasi-one dimensional system where the effects of the external confinement can be modeled by a three-dimensional harmonic oscillator potential Eq. (2.38), the frequencies of the trap in the transverse directions $\omega_\perp = \omega_x = \omega_y$ are tighter or larger than the frequency in the remaining direction ω_z. If we then consider the scenario when $a_\perp = \sqrt{\hbar/(m\omega_\perp)} \gg a_s$, it is more likely to get excitations along the axis with the weakest confinement and for sufficiently strong transverse confinement the transverse excitations become effectively frozen. In this case, within the regularized interaction potential Eq. (2.13), a one-dimensional

scattering amplitude can be obtained leading to a scattering length given by $a_{1\mathrm{D}} = -(a_\perp^2/2a_s)(1 - Ca_s/a_\perp)$ where C is some dimensionless constant [29]. Then, the effective one dimensional interaction potential is given by $U(z - z') = g_{1\mathrm{D}}\delta(z - z')$ where the effective one dimensional coupling constant is $g_{1\mathrm{D}} = g/\left(2\pi a_\perp^2(1 - Ca_s/a_\perp)\right)$ [29]. This suggests that the strength of the effective 1D interaction coupling can be tuned either by varying the 3D scattering length a_s or by changing the width of the transverse confinement $a_\perp$.

2.2.3 Effective Hubbard-like model

For dilute gases at ultracold temperatures, the second-quantized form of the many-body Hamiltonian for N interacting bosons can be written as

$$\begin{aligned}\hat{H} = &\int d\mathbf{r}\hat{\Psi}^\dagger(\mathbf{r})\left(-\frac{\hbar^2}{2m}\nabla^2 + V(\mathbf{r})\right)\hat{\Psi}(\mathbf{r}) \\ &+ \frac{1}{2}\int \hat{\Psi}^\dagger(\mathbf{r})\left(\int d\mathbf{r}'\hat{\Psi}^\dagger(\mathbf{r}')U(\mathbf{r} - \mathbf{r}')\hat{\Psi}(\mathbf{r}')\right)\hat{\Psi}(\mathbf{r}).\end{aligned} \tag{2.39}$$

Here, we assume that only two-body collisions are relevant and we only consider low energies such that the interparticle interaction can be characterized by the s-wave scattering length of the atoms a_s. Moreover, we assume that the gas is dilute which means

$$\sqrt{|\overline{n}a_s^2|} \ll 1 \tag{2.40}$$

where $\overline{n}$ is the average density of the gas [26]. These conditions enable us to use the short ranged pseudopotential given by Eq. (2.13) to model the interaction potential $U(\mathbf{r} - \mathbf{r}')$. This set of assumptions allows us to express the second-quantized Hamiltonian as

$$\hat{H} = \int d\mathbf{r}\hat{\Psi}^\dagger(\mathbf{r})\left(-\frac{\hbar^2}{2m}\nabla^2 + V(\mathbf{r})\right)\hat{\Psi}(\mathbf{r}) + \frac{g}{2}\int \hat{\Psi}^\dagger(\mathbf{r})\hat{\Psi}^\dagger(\mathbf{r})\hat{\Psi}(\mathbf{r})\hat{\Psi}(\mathbf{r}), \tag{2.41}$$

where the coupling constant is $g = 4\pi\hbar^2 a_s/m$. For double-well systems, we can then use the set of localized functions constructed from appropriate symmetric and

antisymmetric superpositions of single-particle functions, as done in Eqs (2.34) and (2.35), to expand the bosonic field operator

$$\hat{\Psi}(\mathbf{r}) = \sum_{j,\ell} \hat{b}_j^\ell \phi_j^\ell(\mathbf{r}), \tag{2.42}$$

where $\phi_j^\ell(\mathbf{r})$ is a localized wave function with on-site energy index of $\ell \in \{0, 1, \dots\}$ and well index $j \in \{L, R\}$ corresponding to the left and right wells, respectively. In this thesis, we shall restrict our results up to $\ell \in 0, 1$ only. The bosonic creation and annihilation operators follow the usual commutation relations

$$\begin{aligned} [\hat{b}_j^\ell, \hat{b}_{j'}^{\ell'\dagger}] &= \delta_{jj'}\delta_{\ell\ell'} \\ [\hat{b}_j^\ell, \hat{b}_{j'}^{\ell'}] &= [\hat{b}_j^{\ell\dagger}, \hat{b}_{j'}^{\ell'\dagger}] = \delta_{jj'}\delta_{\ell\ell'}. \end{aligned} \tag{2.43}$$

Substituting Eq. (2.42) to the second-quantized Hamiltonian Eq. (2.41) give the multi-level or generalized Hubbard-like Hamiltonian which describes the discretized limit of the system

$$\hat{H} = \sum_\ell \left(\hat{H}_\ell + \sum_{\ell' \neq \ell} \hat{H}_{\ell\ell'} \right), \tag{2.44}$$

where

$$\hat{H}_\ell = -J^\ell \sum_{j \neq j'} \hat{b}_j^{\ell\dagger} \hat{b}_{j'}^\ell + \sum_j U_j^{\ell\ell} \hat{n}_j^\ell (\hat{n}_j^\ell - 1) + \sum_j E_j^\ell \hat{n}_j^\ell, \tag{2.45}$$

and

$$\hat{H}_{\ell\ell'} = \sum_j U_j^{\ell\ell'} \left(2\hat{n}_j^\ell \hat{n}_j^{\ell'} + \hat{b}_j^{\ell\dagger} \hat{b}_j^{\ell\dagger} \hat{b}_j^{\ell'} \hat{b}_j^{\ell'} \right). \tag{2.46}$$

Here, we introduce the number operator $\hat{n}_j^\ell = \hat{b}_j^{\ell\dagger} \hat{b}_j^\ell$. The on-site energy is

$$E_j^\ell = \int d\mathbf{r} \phi_j^{\ell*}(\mathbf{r}) \left[-\frac{\hbar^2}{2m} \nabla^2 + V(\mathbf{r}) \right] \phi_j^\ell(\mathbf{r}). \tag{2.47}$$

The tunneling term is

$$J^\ell = -\int d\mathbf{r} \phi_j^{\ell*}(\mathbf{r}) \left[-\frac{\hbar^2}{2m} \nabla^2 + V(\mathbf{r}) \right] \phi_{j'}^\ell(\mathbf{r}) \tag{2.48}$$

where $j' \neq j$. Note that we have neglected in Eq. (2.46), the inter-level coupling terms of the form $\hat{b}_j^{\ell\dagger} \hat{b}_j^{\ell\dagger} \hat{b}_j^\ell \hat{b}_j^{\ell'}$ which physically corresponds to peculiar co-tunneling of

two bosons in one site at level ℓ to a state where one boson remains in that state and the other boson gets transferred to a different level ℓ' (or vice versa). Numerically, the integrals corresponding to these terms will have almost zero values for well-localized wave functions because the corresponding integrand is antisymmetric about the minima of the wells. Thus, we only consider the interaction couplings corresponding to

$$U_j^{\ell\ell'} = \int d\mathbf{r} |\phi_j^{\ell}|^2 |\phi_j^{\ell'}|^2. \tag{2.49}$$

In general, the Hubbard parameters comprising of J_ℓ, $U_j^{\ell\ell'}$, and E_j^ℓ are obtained by evaluating the integrals above either numerically or analytically after some approximations [26]. In the simplest possible limit of a one-level approximation where the higher energy levels $\ell > 0$ are well separated from the lowest level $\ell = 0$, the Hamiltonian in Eq. (2.44) simplifies to the Bose-Hubbard dimer or the Lipkin-Meshkov-Glick Hamiltonian given by Eq. (2.45) [30]. If we have an optical lattice instead of a double-well potential then one can construct an actual set of Wannier functions and the discretized model simplifies to the standard single-band Bose-Hubbard model [11].

2.3 Quantum ergodicity in closed quantum systems

The emergence of statistical properties and thermalization in classical systems can be understood from the concept of classical chaos and how it can lead to ergodicity. A classical system is considered ergodic if most of the trajectories uniformly cover the available phase-space in a constant-energy manifold. Here, the long-time averages become equivalent to appropriate microcanonical ensemble predictions. On the other hand, if a system with M number of canonical degrees-of-freedom has exactly the same M number of integrals of motion, meaning their corresponding Poisson brackets with the Hamiltonian vanish, then the dynamics of trajectories become regular as opposed to being chaotic. In such cases, the system becomes non-ergodic and only a limited area of phase space gets explored by the ensemble of trajectories.

The challenge of formulating similar ideas of thermalization in quantum mechanical systems has been already recognized even in the early days of the development of quantum mechanics through one of von Neumann's works [31]. The main difficulty lies in identifying a convincing quantum mechanical counterpart of classical chaos. A fundamental challenge comes from the fact that time evolution according to the Schrödinger equation is linear and unitary. But non-linearity is an essential ingredient for classical chaos and so, the usual notion and definition of chaos in classical systems become invalid for isolated quantum mechanical systems.

In this section, a short overview is given about the developments that led to one of the leading candidates for a theory of quantum ergodicity - the *eigenstate thermalization hypothesis*. First, we discuss a framework for describing quantum chaos using random matrix theory (RMT). Afterwards, we introduce the concept of eigenstate thermalization hypothesis and how it can describe the dynamical emergence of statistical properties in closed quantum systems. A more detailed review on the issue of thermalization in quantum systems can be found in Ref [32].

2.3.1 Quantum chaos

One test for nonintegrability in quantum systems is the statistics of the energy level spacings. The Berry-Tabor conjecture states that the energy level spacing of quantum systems whose classical counterparts are integrable will possess Poissonian statistics [33]. On the other hand, the Bohigas-Giannoni-Schmidt conjecture says that the energy level spacing of quantum systems whose classical counterparts are non-integrable will follow one of the three possible ensembles from random matrix theory (RMT) which are the Gaussian Orthogonal Ensemble (GOE) for time-reversal-invariant systems, the Gaussian Unitary Ensemble (GUE) for systems with broken time-reversal symmetry, and the Gaussian Symplectic Ensemble (GSE) for systems with rotational symmetry. [34].

Some of the more important developments in the study of quantum chaos can be traced back to the pioneering works of Wigner and Dyson when they considered

the problem of understanding the spectra of complex atomic nuclei (for a review on this see Ref. [35]). These works have paved the way to the formulation of RMT. The argument was for complex quantum mechanical systems, obtaining the exact eigenstates and eigenvalues can easily become computationally unfeasible and therefore, it is more practical to focus on statistical properties of the spectra, instead. Another key idea by Wigner is to treat an exponentially complex Hamiltonian as a matrix, the elements of which are drawn from some random distribution. It is an important requirement, however, that the random Hamiltonian matrix still follows the necessary symmetry of the actual physical system such as time reversal invariance, for example.

To exemplify one of the basic concepts of RMT which is the statistics of the eigenenergies, let us consider the following two-level system

$$\mathcal{H} = \begin{pmatrix} \epsilon_1 & V/\sqrt{2} \\ V^*/\sqrt{2} & \epsilon_2 \end{pmatrix}. \tag{2.50}$$

For simplicity, let us assume that the system has time reversal symmetry such that V is real. Then the eigenvalues of the matrix can be easily obtained as

$$E_{1,2} = \frac{\epsilon_1 + \epsilon_2}{2} \pm \frac{1}{2}\sqrt{(\epsilon_1 - \epsilon_2)^2 + 2|V|^2} \tag{2.51}$$

Moreover, the matrix elements ϵ_1, ϵ_2, and V are random numbers taken from some Gaussian distribution which has zero mean and variance σ. We can then construct a distribution for the energy level spacing $E_1 - E_2 = \omega$

$$\begin{aligned} P(\omega) &= \frac{1}{(2\pi)^{3/2}\sigma^3} \int\int\int d\epsilon_1 d\epsilon_2 dV \, \delta\left((E_1 - E_2) - \omega\right) \exp\left(-\frac{\epsilon_1^2 + \epsilon_2^2 + V^2}{2\sigma^2}\right) \quad (2.52) \\ &= \frac{1}{(2\pi)^{3/2}\sigma^3} \int\int\int d\epsilon_1 d\epsilon_2 dV \, \delta\left(\sqrt{(\epsilon_1 - \epsilon_2)^2 + 2V^2} - \omega\right) \exp\left(-\frac{\epsilon_1^2 + \epsilon_2^2 + V^2}{2\sigma^2}\right) \end{aligned}$$

We first make a change of variable $\epsilon_2 = \epsilon_1 + \sqrt{2}\xi$ and then evaluate the integral over ϵ_1 which is just a Gaussian integral to get

$$P(\omega) = \frac{1}{(2\pi)^{3/2}\sigma^3} \int\int d\xi dV \, \delta\left(\sqrt{2\xi^2 + 2V^2} - \omega\right) \exp\left(-\frac{\xi^2 + V^2}{2\sigma^2}\right) \tag{2.53}$$

The rest of the integration can be done by transform to cylindrical coordinates $V = r\cos(\phi)$ and $\xi = r\sin(\phi)$. This will yield

$$P(\omega) = \frac{\omega}{2\sigma^2}\exp\left(-\frac{\omega^2}{4\sigma^2}\right). \tag{2.54}$$

The main feature of this distribution is the so-called level repulsion in which $P(\omega) = 0$ for arbitrarily close or almost degenerate energy levels, $\omega = 0$. This exact result for a 2×2 matrix originally calculated by Wigner motivated him to surmise an approximate formula for the distribution of the level spacing for Gaussian-like distribution

$$P(\omega) = a_\beta \omega^\beta \exp(-(b_\beta)\omega^2), \tag{2.55}$$

where the constants a_β and b_β are known constants depending on the symmetry of the Hamiltonian. For example $\beta = 1$ corresponds to the Gaussian Orthogonal Ensemble (GOE) which models a time-reversal symmetric system.

An analysis based on the RMT level spacing statistics is based on the assumption that the local density of states of a system is equal to one. Each model can have different density of states and therefore, in order to get a fair comparison between different models, a procedure called *unfolding* needs to be implemented. The main goal of this unfolding procedure is to transform the energy levels such that the mean density of states is set to unity. However for many-body quantum systems, this unfolding procedure can be cumbersome and computationally expensive. Oganesyan and Huse later proposed the use of the ratio of consecutive energy gaps instead of the energy gaps themselves when computing for distributions [36]. First let us arrange the energy levels in increasing order $\{E_n\} = \{E_1, E_2, \ldots, E_N\}$ where $E_1 < E_2 < \cdots < E_N$. Then, the level spacing is just $\omega_n = E_{n+1} - E_n$ and the ratio of level spacing is $r_n = \omega_{n+1}/\omega_n$. Specifically, Oganesyan and Huse looked at the distribution of the ratios

$$\tilde{r}_n = \min\left(r_n, \frac{1}{r_n}\right). \tag{2.56}$$

For integrable many-body quantum systems, the distribution for the ratio of level spacing between consecutive level spacing $P(\tilde{r})$ follows the Poisson distribution,

$$P_{\mathrm{POI}}(\tilde{r}) = \frac{2}{(1+\tilde{r}^2)}. \tag{2.57}$$

While for chaotic Hamiltonian with time reversal symmetry, the ratios $\tilde{r}_n$ are distributed according to the GOE ensemble whose analytic expression was first derived by Atas, *et al.* [37]

$$P_{\mathrm{GOE}}(\tilde{r}) = \frac{27}{4}\frac{\tilde{r}+\tilde{r}^2}{(1+\tilde{r}+\tilde{r}^2)^{5/2}}. \tag{2.58}$$

2.3.2 Eigenstate thermalization hypothesis

As first noted by von Neumann [31], thermalization in quantum systems must be looked at a different perspective by considering the unitary time evolution of observables rather than the wave function or the density matrix of the system. One of the crucial points missed by von Neumann, however, is the importance of integrability or the lack thereof in the phenomenon of quantum ergodicity. In the following discussion, we will outline the general arguments of one of the more commonly accepted theories called *eigenstate thermalization hypothesis* (ETH) that might explain how observables thermalize in isolated quantum systems. The original idea behind this hypothesis can be traced back to works done in the 1990's by Deutsch [38] and Srednicki [39–41].

Consider an isolated quantum system initially prepared in a state $|\psi_0\rangle$. Note that for simplicity we shall only consider initial pure states in the remaining discussion. However, the arguments below can be generalized and also applied to initial mixed states. The system evolves in time according to a time-independent Hamiltonian $\hat{H}$ with eigenvectors $|m\rangle$ and eigenvalues E_m. The many-body wave function at any given time can be obtained from

$$|\psi(t)\rangle = \sum_m C_m e^{-iE_m t}|m\rangle, \tag{2.59}$$

where we set $\hbar = 1$ and the coefficients are $C_m = \langle m|\psi_0\rangle$. The density matrix of the full system starts out as a pure state and will remain so for the rest of the time evolution. This fact presents itself as one of the bottlenecks in understanding thermalization in closed quantum systems because of the impossibility of the density matrix to become a mixed and thermal density matrix. For this reason, it was argued

by von Neumann [31] that one needs to look at observables which effectively restricts our observation to only a part of the entire system or a subsystem. If we look at the time dependence of a physically relevant observable $\hat{O}$, we can express it in terms of the eigenvectors of the Hamiltonian

$$\begin{aligned} O(t) \equiv \langle\psi(t)|\hat{O}|\psi(t)\rangle &= \sum_{m,n} C_m^* C_n e^{i(E_m - E_n)t} O_{mn} \\ &= \sum_m |C_m|^2 O_{mm} + \sum_{m,n\neq m} C_m^* C_n e^{i(E_m - E_n)t} O_{mn}, \end{aligned} \tag{2.60}$$

where $O_{mn} = \langle m|\hat{O}|n\rangle$ and in the second line we simply separate the terms dependent on the off-diagonal matrix elements of O_{mn}. Then, an observable $\hat{O}$ thermalizes if the long-time average of the expectation value of $\hat{O}$ is close to a microcanonical expectation value and if the temporal fluctuations of this expectation value about the microcanonical prediction are small. ETH postulates that such thermalization is possible for nonintegrable systems in the sense of RMT (no degeneracies or at most they are suppressed with system size) because the matrix elements of an observable can be written as [41]

$$O_{mn} = O(\overline{E})\delta_{mn} + e^{-S(\overline{E})/2} f_O(\overline{E}, \omega) R_{mn}, \tag{2.61}$$

where $\overline{E} = (E_m + E_n)/2$, $\omega = E_n - E_m$, and $S(E)$ is the entropy at energy E. The functions $O(\overline{E})$ and $f_O(\overline{E}, \omega)$ are both smooth and as such the microcanonical expectation value at energy $\overline{E}$ is exactly equal to $O(\overline{E})$. Also, the matrix elements R_{mn} are real or complex random variables with zero mean and unit variance. The physical concepts which motivate the use of this expression as an ansatz for the matrix elements of an operator are explained below. But roughly speaking, the first term is important to get good agreement with the microcanonical ensemble prediction while the form of the second term corresponding to the off-diagonal elements is conjectured as such in order to get exponentially small temporal fluctiations of the operator. However, it is important to mention that there is no rigorous proof supporting the ETH. However, the validity of the ETH has been numerically tested for few-body

observables (the operator of the observable only acts on a small subsystem) in different lattice or discretized models. An example of which is the numerical experiment done by Rigol, *et al.*, for a system of hard-core bosons in a lattice with integrability-breaking terms [16].

For nonintegrable systems, the ETH ansatz according to Eq. (2.61) yields a long-time average of the expectation value of an observable given by

$$\overline{O} = \lim_{t_0\to\infty} \int_0^{t_0} dt O(t) = \sum_m |C_m|^2 O_{mm} = \mathrm{Tr}(\hat{\rho}_{\mathrm{DE}}\hat{O}), \tag{2.62}$$

where $\hat{\rho}_{\mathrm{DE}}$ is the density matrix of the diagonal ensemble $\hat{\rho}_{\mathrm{DE}} = \sum_m |C_m|^2 |m\rangle\langle m|$. This result can be straightforwardly obtained from Eq. (2.60) where the long-time average of the second term vanishes due to dephasing. This dephasing mechanism can be understood as the process at which for long times, time evolution mixes the phases of the off-diagonal terms in Eq. (2.60) such that their contributions effectively have factors of random phases and thus they eventually cancel out [42]. The corresponding statistical prediction according to the microcanonical ensemble for the expectation value is

$$O_{\mathrm{ME}} = \mathrm{Tr}(\hat{\rho}_{\mathrm{ME}}\hat{O}), \tag{2.63}$$

where $\hat{\rho}_{\mathrm{ME}}$ is the density matrix of the microcanonical ensemble. This expectation value can be expressed in terms of the eigenvectors $|m\rangle$ as

$$O_{\mathrm{ME}} = \mathcal{N}^{-1} \sum_{|E_m - E_0| < \Delta E} O_{mm}, \tag{2.64}$$

where $\mathcal{N}$ is the number of eigenstates within a narrow energy window ΔE centered around the initial average energy of the system E_0. Finally, if we use Eq. (2.61) to rewrite Eqs. (2.62) and (2.64), we get

$$\overline{O} \approx O(\overline{E}) \approx O_{\mathrm{ME}}, \tag{2.65}$$

which means the long-time average of an expectation value of an operator is close to a microcanonical ensemble prediction. This can be considered as the main statement of

the ETH. Now as for the second condition of thermalization related to small temporal fluctuations about the microcanonical value, the ETH ansatz Eq. (2.61) gives [32]

$$\begin{aligned}\sigma_O^2 &= \lim_{t_0\to\infty}\frac{1}{t_0}dt\left((O(t))^2-(\overline{O})^2\right) \\ &= \sum_{m,n\neq m}|C_m|^2|C_n|^2|O_{mn}|^2 \leq \max|O_{mn}|^2 \propto \exp(-S(\overline{E})),\end{aligned} \tag{2.66}$$

suggesting that the temporal fluctuations become exponentially small as the system size grows.

Chapter 3

Numerical Methods

3.1 Multiconfigurational time-dependent Hartree for bosons

The multiconfigurational time-dependent Hartree for bosons (MCTDHB) method is one of the many numerical methods that aim to solve many-body quantum problems that goes beyond the mean-field approximation provided by the Gross-Pitaevskii theory. In this section, we introduce the basic concepts involved in the MCTDHB theory. If the reader is interested in a more rigorous derivation of the underlying theory of the MCTDHB algorithm, Ref. [43] provides a detailed discussion.

3.1.1 MCTDHB wave function

The main goal of any many-body numerical methods is to solve the Schrödinger equation for an interacting system. Specifically for N interacting bosons in dilute conditions, the many-body Hamiltonian can be written as

$$\hat{H} = \sum_{i=1}^{N} \hat{h}(\mathbf{r}_i) + \sum_{i<j} g\delta(\mathbf{r}_i - \mathbf{r}_j), \tag{3.1}$$

where $\mathbf{r}_i$ denotes the position coordinate of the i-th boson, $\hat{h}(\mathbf{r}) = -\frac{\hbar^2}{2m}\nabla^2 + V(\mathbf{r},t)$ is the single-particle Hamiltonian for same species of bosons with mass m, and g is the strength of the two-body contact interaction between the bosons. Within the MCTDHB formalism, the wave function can be expanded in bra and ket notation as follows

$$\begin{aligned} |\Psi(t)\rangle &= \sum_{\vec{n}} C_{\vec{n}}(t)|\vec{n},t\rangle \\ &= \sum_{n_1}\cdots\sum_{n_M} C_{n_1,n_2,\ldots,n_M}\prod_{k=1}^{M}\frac{1}{\sqrt{n_k!}}[\hat{b}_k^\dagger(t)]^{n_k}|\text{vac}\rangle \end{aligned} \tag{3.2}$$

where the time-dependent expansion coefficients are given by the vector $C_{\vec{n}}(t) \equiv \vec{C}$. Here, all possible combinations of occupying the available M single-particle modes is represented by $\vec{n} = \{n_1, n_2, \ldots, n_M\}$. This means that $\sum_{i=1}^{M} n_i = N$ where N is the total number of bosons in the system. The size of the Hilbert space for this basis set expansion is $\frac{(N+M-1)!}{N!(M-1)!}$. Here, the bosonic creation operators follow

$$\begin{aligned} \hat{b}_k^\dagger(t) &= \int d\mathbf{r}\phi_k(\mathbf{r},t)\hat{\Psi}^\dagger(\mathbf{r},t) \\ [\hat{b}_k^\dagger,\hat{b}_j^\dagger] &= [\hat{b}_k,\hat{b}_j] = 0 \\ [\hat{b}_k,\hat{b}_j^\dagger] &= \delta_{k,j}. \end{aligned} \tag{3.3}$$

Note that we have introduced the bosonic field operator $\Psi^\dagger(\mathbf{r},t) = \sum_j \hat{b}_j^\dagger(t)\phi_j^*(\mathbf{r},t)$ that creates a boson at position $\mathbf{r}$ and time t. The time-dependent single-particle functions are orthonormalized

$$\int d\mathbf{r}\phi_k(\mathbf{r},t)\phi_j^*(\mathbf{r},t) = \delta_{kj}. \tag{3.4}$$

The many-body Hamiltonian Eq. (3.1) can be expressed in terms of the bosonic creation and annihilation operators as follows

$$\hat{H} = \sum_{k,j}\hat{b}_k^\dagger\hat{b}_j h_{kj} + \frac{1}{2}\sum_{k,j,q,i}\hat{b}_k^\dagger\hat{b}_j^\dagger\hat{b}_q\hat{b}_i W_{kjqi}, \tag{3.5}$$

where the relevant integrals are given by

$$h_{kj} = \int d\mathbf{r}\phi_k^*(\mathbf{r},t)\hat{h}(\mathbf{r},t)\phi_j(\mathbf{r},t), \tag{3.6}$$
$$W_{kjqi} = g\int d\mathbf{r}\phi_k^*(\mathbf{r},t)\phi_j^*(\mathbf{r},t)\phi_q(\mathbf{r},t)\phi_i(\mathbf{r},t).$$

The main convergence parameter in MCTDHB is the number of single-particle modes M used in the many-body wave function expansion. In principle, the representation becomes exact in the limit of $M \to \infty$ as this will span the entire Hilbert space. In the opposite limit of $M = 1$, only one mode is occupied by all of the bosons and the Gross-Pitaevskii limit of macroscopically occupying one state is recovered. In practice, however, the expansion needs to be truncated in order to make any sensible numerical implementation of the theory. The claim is that in allowing both the expansion coefficients $\{C_{\vec{n}}(t)\}$ and also the single-particle functions $\{\phi_k(\mathbf{r},t)\}$ to dynamically evolve in time according to some variational optimization, one can get away with using fewer number of modes M in representing the quantum many-body wave function.

3.1.2 Time-evolution of the MCTDHB wave function

Within the framework of Lagrangian formalism, the functional action of the time-dependent Schrödinger equation is [43]

$$S[\{C_{\vec{n}}(t)\},\{\phi_k(\mathbf{r},t)\}] = \int dt\Big\{\langle\Psi|\hat{H} - i\frac{\partial}{\partial t}|\Psi\rangle - \sum_{k,j=1}^{M}\mu_{k,j}(t)[\langle\phi_k|\phi_j\rangle - \delta_{kj}]\Big\}, \tag{3.7}$$

where the time-dependent Langrange multipliers $\mu_{k,j}(t)$ ensures that the time-dependent single-particle functions $\phi_k(\mathbf{r},t)$ remain orthonormal for the entirety of the time evolution. We then take the variation separately with respect to $\{C_{\vec{n}}(t)\}$ and $\{\phi_k(\mathbf{r},t)\}$. These will eventually lead to a set of coupled equations of motion the details on the derivation of which can be found in Ref. [43]. At this point, it is important to write

down the expressions for the reduced single-particle density matrix

$$\begin{aligned}\rho(\mathbf{r}_1,\mathbf{r'}_1,t) &= \langle\Psi(t)|\hat{\Psi}^\dagger(\mathbf{r'}_1)\hat{\Psi}(\mathbf{r}_1)|\Psi(t)\rangle \\ &= N\int d\mathbf{r}_2 d\mathbf{r}_3\ldots d\mathbf{r}_N \Psi^*(\mathbf{r'}_1,\mathbf{r}_2,\ldots,\mathbf{r}_N,t)\Psi(\mathbf{r}_1,\mathbf{r}_2,\ldots,\mathbf{r}_N,t) \\ &= \sum_{k,q=1}^{M}\rho_{kq}(t)\phi_k^*(\mathbf{r'}_1,t)\phi_k(\mathbf{r}_1,t),\end{aligned} \tag{3.8}$$

where $\rho_{kq}(t)$ are matrix elements of the reduced single-particle density matrix $\rho(t)$, and also the reduced two-particle density matrix

$$\begin{aligned}\rho(\mathbf{r}_1,\mathbf{r}_2,\mathbf{r'}_1,\mathbf{r'}_2,t) &= \langle\Psi(t)|\hat{\Psi}^\dagger(\mathbf{r'}_1)\hat{\Psi}^\dagger(\mathbf{r'}_2)\hat{\Psi}(\mathbf{r}_1)\hat{\Psi}(\mathbf{r}_2)|\Psi(t)\rangle \\ &= N(N-1)\int d\mathbf{r}_3\ldots d\mathbf{r}_N \Psi^*(\mathbf{r'}_1,\mathbf{r'}_2,\ldots,\mathbf{r}_N,t)\Psi(\mathbf{r}_1,\mathbf{r}_2,\ldots,\mathbf{r}_N,t) \\ &= \sum_{k,s,q,j=1}^{M}\rho_{ksqj}(t)\phi_k^*(\mathbf{r'}_1,t)\phi_s^*(\mathbf{r'}_2,t)\phi_q(\mathbf{r}_1,t)\phi_j(\mathbf{r}_2,t),\end{aligned} \tag{3.9}$$

where $\rho_{ksqj}(t)$ are matrix elements of the reduced two-particle density matrix. The expression of the matrix elements $\rho_{kq}(t)$ and $\rho_{ksqj}(t)$ and how they can be calculated from the time-dependent expansion coefficients $C_{\vec{n}}$ and the permanents can be found in Ref. [43]. In terms of the numerical implementation of the MCTDHB method, the so-called mean-fields ρ_{kq}, ρ_{ksqj}, h_{kq}, and W_{ksqj} are updated every time step in the numerical integration. Performing the corresponding variation

$$\frac{\partial S[\{C_{\vec{n}}(t)\},\{\phi_k(\mathbf{r},t)\}]}{\partial C_{\vec{n}}^*(t)} = \frac{\partial S[\{C_{\vec{n}}(t)\},\{\phi_k(\mathbf{r},t)\}]}{\partial \phi_k^*(\mathbf{r},t)} = 0 \tag{3.10}$$

leads to the set of coupled non-linear equations

$$\begin{aligned}\mathbf{H}(t)\mathbf{C}(t) &= i\frac{\partial\mathbf{C}(t)}{\partial t} \\ i\frac{\partial}{\partial t}|\phi_i\rangle &= \hat{\mathbf{P}}\left[\hat{h}|\phi_i\rangle + g\sum_{k,s,q,j=1}^{M}\{\rho^{-1}\}_{ik}\rho_{ksqj}\phi_s^*(x)\phi_j(x)|\phi_q\rangle\right]\end{aligned} \tag{3.11}$$

where $\mathbf{H}(t) = \{H_{\vec{n}\vec{m}}(t) = \langle\vec{n},t|\hat{H}|\vec{m},t\rangle\}$ and $\mathbf{C}(t) = \{C_{\vec{n}}(t)\}$. The projector $\hat{\mathbf{P}} = 1 - \sum_{m=1}^{M}|\phi_m\rangle\langle\phi_m|$ guarantees that the single-particle functions are orthogonal to their time derivatives, i.e., $\langle\phi_i|\frac{\partial}{\partial t}|\phi_j\rangle = 0$.

The relevance of the single-particle or mode functions in the MCTDHB wave function expansion can be assessed by examining the eigenvalues of the single-particle density matrix commonly known as the natural occupancies n_k^{NO}

$$\langle\Psi(t)|\hat{\Psi}^{\dagger}(\mathbf{r}'_1)\hat{\Psi}(\mathbf{r}_1)|\Psi(t)\rangle = \sum_{k=1}^{M} n_k^{\mathrm{NO}}\varphi_k^*(\mathbf{r}'_1)\varphi_k^*(\mathbf{r}_1), \tag{3.12}$$

where $\sum_k n_k^{\mathrm{NO}} = N$ and $\varphi_k(\mathbf{r}_1)$ are the so-called natural orbitals which are eigenvectors of the reduced single-particle density matrix. Convergence of the multi-mode expansion can be invoked depending on how fast the natural occupancies are decreasing in value. Recall that the reduced single-particle density matrix and more importantly its eigenvalues are related to the notion of long-range order used to classify Bose-Einstein condensation or possibly fragmentation. In the case of a BEC, the leading order or highest natural occupancy is expected to be of the same order as the total number of bosons, i.e., $\max(n_k^{\mathrm{NO}}) \approx N$. On the other hand for fragmented systems, at least two natural orbitals are significantly occupied meaning two or possible more natural occupancies have large values.

Finally, we briefly discuss the applicability and limitations of the MCTDHB method. A chapter of this thesis is devoted to a systematic benchmarking of MCTDHB for systems with attractively interacting bosons. In that work, we found out that MCTDHB will have difficulties simulating scenarios where there are diverging length scales in the system. An example of which is the case when the center-of-mass wave function is ballistically expanding in time while the relative motion practically remains unchanged for long times. The length scales associated to these two quantities will diverge from one another as the system evolves in time. Unfortunately, the behavior for this type of dynamical problem is found to be difficult for MCTDHB to correctly capture as will be discussed in much more detail later on. On the other hand, for the dynamics of repulsively interacting bosons confined by some external trap, MCTDHB is generally expected to exhibit good convergence. Moreover, problems involving systems with inherently few number of relevant single-particle modes are naturally good candidates for MCTDHB to solve. For example in double well

systems, if the barrier is high enough the two lowest single-particle eigenstates are well separated from the rest of the spectrum. As such, MCTDHB has been used in the past to study correction to the single-band or single-level approximation in optical lattices or multi-well systems, respectively [44–53]. In terms of the numerical implementation, the dimensionality of the system plays an important role in the computational feasibility of the method. For continuous systems or models, it is imperative to represent the system by some grid according to a specific discretization procedure. Ultimately, the number of points needed to obtain convergent results with respect to this discretization will obviously increase with the dimension of the system in consideration. This factor together with the possibility that one may need to use a considerable amount of single-particle modes in order to converge the MCTDHB wave function representation can put a strong limitation to the type of dynamical problem that can be studied using MCTDHB.

3.2 Truncated Wigner approximation

We have utilized a particular phase-space method based on the Wigner representation for our work in understanding quantum thermalization in a one-dimensional double-well potential from a semiclassical perspective as presented in Chapter 7. In this section, we give a brief introduction to the truncated Wigner representation and how it can be implemented numerically in order to approximate the quantum evolution in a system. A more detailed review on phase-space methods for quantum dynamics can be found in Refs. [54, 55].

3.2.1 Wigner distribution

The description of quantum mechanics using phase space variables as in classical physics has proven to be a quite powerful tool both in gaining new insights and in solving the time evolution of a quantum mechanical system. One of the motivations

for representing quantum mechanics in terms of phase space distributions is the possibility to find a connection between quantum and statistical fluctuations. Perhaps the most well-known phase space or quasiprobability distribution is the so-called Wigner distribution formulated by Wigner in 1932 [56]. The key idea of phase space representations is to represent quantum operators as complex numbers spanning the phase space of canonical variables. Within the Wigner representation, this can be done in various ways such as the coordinate-momentum representation or the coherent state representation [55]. Due to the relevance in our work, we shall focus on the coherent state representation for the rest of this thesis. In order to map an arbitrary quantum operator $\hat{O}(\hat{a}, \hat{a}^\dagger)$ to its corresponding classical phase space counterpart $O_W(a, a^*)$ with a and a^* being complex numbers (c-numbers), the following Weyl transformation is used [54, 55]

$$O_W(a, a^*) = \frac{1}{2^M} \int \int d\eta^* d\eta \langle a - \frac{\eta}{2} | \hat{O}(\hat{a}, \hat{a}^\dagger) | a + \frac{\eta}{2} \rangle e^{-|a|^2 - \frac{1}{4}|\eta|^2} e^{\frac{1}{2}(\eta^* a - \eta a^*)}, \tag{3.13}$$

where M is the Hilbert space size, $\hat{a}$ and $\hat{a}^\dagger$ are bosonic annihilation and creation operators, respectively, and $|\alpha\rangle$ is a coherent state $\hat{a}|\alpha\rangle = a|\alpha\rangle$. The Wigner distribution $W(a, a^*)$ is then defined as simply the Weyl transform of the density matrix $\hat{\rho}$

$$W(a, a^*) = \frac{1}{2^M} \int \int d\eta^* d\eta \langle a - \frac{\eta}{2} | \hat{\rho} | a + \frac{\eta}{2} \rangle e^{-|a|^2 - \frac{1}{4}|\eta|^2} e^{\frac{1}{2}(\eta^* a - \eta a^*)}. \tag{3.14}$$

One of the interesting properties of the Wigner function is that it is not necessarily positive for certain quantum states like in the case of a number or Fock state. This is the reason for why it is often times referred to as a quasiprobability distribution as opposed to an actual probability distribution which is always positive. A simple trick in mapping coherent state operators to their corresponding Wigner-Weyl transform is by means of the Bopp representation [54, 55]

$$\begin{aligned} \hat{a}_j^\dagger &\to a_j^* - \frac{1}{2} \frac{\partial}{\partial a_j} \\ \hat{a}_j &\to a_j + \frac{1}{2} \frac{\partial}{\partial a_j^*}, \end{aligned} \tag{3.15}$$

where $[\hat{a}_i, \hat{a}_j^\dagger] = \delta_{ij}$ and $\{a_i, a_j^*\}_C = \delta_{ij}$. The coherent state Poisson bracket $\{A, B\}_C$ can be regarded as the classical analogue of the commutator and it is given by

$$\{A, B\}_C = A\Lambda_C B = \sum_j \left(\frac{\partial A}{\partial a_j}\frac{\partial B}{\partial a_j^*} - \frac{\partial A}{\partial a_j^*}\frac{\partial B}{\partial a_j} \right), \tag{3.16}$$

where Λ_C is called the symplectic coherent state operator

$$\Lambda_C = \sum_j \left(\frac{\overleftarrow{\partial}}{\partial a_j}\frac{\overrightarrow{\partial}}{\partial a_j^*} - \frac{\overleftarrow{\partial}}{\partial a_j^*}\frac{\overrightarrow{\partial}}{\partial a_j} \right) \tag{3.17}$$

It is particularly useful in preparation for the subsequent discussion on the time evolution of quantum operators to write down the expression for the Wigner-Weyl transform of the commutator between two quantum operators $\hat{\Omega} = [\hat{\Omega}_1, \hat{\Omega}_2]$:

$$\Omega_W = \{\Omega_{1,W}, \Omega_{2,W}\}_{\mathrm{MBC}}\,, \tag{3.18}$$

where the so-called Moyal bracket is

$$\{\dots\}_{\mathrm{MBC}} = 2\sinh\left[\frac{1}{2}\{\dots\}_C\right]. \tag{3.19}$$

As a simple example on how to use the Bopp representation to map quantum operators into phase space variables, consider the number operator $\hat{n} = \hat{a}^\dagger\hat{a}$. The Wigner-Weyl transform for this operator can be obtained by

$$(\hat{a}^\dagger\hat{a})_W = \hat{a}^\dagger\hat{a}1 = \left(a^* - \frac{1}{2}\frac{\partial}{\partial a}\right)\left(a + \frac{1}{2}\frac{\partial}{\partial a^*}\right)1 = |a|^2 - \frac{1}{2}. \tag{3.20}$$

Another relevant example would be the two-body operators akin to the on-site interaction term in the Bose-Hubbard model

$$(\hat{a}^\dagger\hat{a}^\dagger\hat{a}\hat{a})_W = \left(a^* - \frac{1}{2}\frac{\partial}{\partial a}\right)^2\left(a + \frac{1}{2}\frac{\partial}{\partial a^*}\right)^2 1 = |a|^4 - 2|a|^2 + \frac{1}{2}. \tag{3.21}$$

In this formalism, the expectation value of an operator can then be calculated from the Wigner function according to

$$\langle\hat{O}\rangle_W \equiv \langle O_W\rangle = \int \prod_j da_j(t)da_j^*(t)O_W(\mathbf{a}(\mathbf{t}))W(\mathbf{a}(\mathbf{t})), \tag{3.22}$$

where for brevity we used the short-hand notation in expressing the dependence on the phase space variables $\mathbf{a}(\mathbf{t}) = \{a_0(t), a_1(t), \dots, a_{M/2}(t), a_0^*(t), a_1^*(t), \dots, a_{M/2}^*(t)\}$.

3.2.2 Time-evolution of observables

We outline here one way of deriving the time evolution of expectation values of observables based on the rigorous discussions found in Ref. [55]. Consider the Hamiltonian of a quantum system $\hat{H}(\hat{a}, \hat{a}^\dagger) \equiv \hat{H}$. The time evolution of the density matrix is described by the von Neumann equation

$$i\hbar \frac{\partial \hat{\rho}}{\partial t} = \left[\hat{H}, \hat{\rho}\right]. \tag{3.23}$$

In general, the Wigner-Weyl transform of this Hamiltonian can be obtained using the prescription discussed above such that $(\hat{H}(\hat{a}, \hat{a}^\dagger))_W = H(a, a^*)_W \equiv H_W$. By taking the Wigner-Weyl transform of both sides of the von Neumann equation, we get the time-evolution of the Wigner function according to

$$i\hbar \frac{\partial W}{\partial t} = \{H_W, W\}_{\mathrm{MBC}} = 2H_W \sinh\left[\frac{\Lambda_C}{2}\right] W \tag{3.24}$$

Up to this point, everything is still exact and no approximation has been made. However, in order to numerically solve the time evolution equation, one needs to make a truncation which is called the truncated Wigner approximation. Note that the Moyal bracket can be expanded in powers of $1/N$ (or equivalently writing the Taylor series expansion for the sinh-function). If only the leading order is retained then we find

$$i\hbar \frac{\partial W}{\partial t} \approx \{H_W, W\}_C, \tag{3.25}$$

which is just the classical Liouville equation for the density matrix. This assumption makes it apparent that the truncated Wigner approximation is expected to work for systems with large number of occupation $N \gg 1$. The equations of motion are obtained by noting that the Wigner function is conserved along the classical trajectories satisfying

$$i\hbar \frac{\partial a_j}{\partial t} = \frac{\partial H_W}{\partial a_j^*} \tag{3.26}$$

Within this approximation scheme, the expectation value of an operator at a specific time can be calculated as,

$$\langle \hat{O}(t) \rangle = \int da_0 da_0^* W(\mathbf{a(0)}) O_W(\mathbf{a(t)}), \tag{3.27}$$

where $W(\mathbf{a}(\mathbf{0}))$ is the initial Wigner function and $da_0 da_0^* = \prod_j da_j(0) da_j^*(0)$. In practice, $\langle \hat{O}(t) \rangle$ is obtained by solving the set of coupled differential equations according to Eq. (3.26) using an ensemble of initial conditions (trajectories), which accurately samples the quantum noise of a chosen initial state and then averaging the results afterwards.

It is possible to go beyond the first approximation given by the TWA by expanding the Moyal bracket up to the third order in Λ_C [55]:

$$i\hbar \frac{\partial W}{\partial t} \approx \{H_W, W\}_C + \frac{1}{8} \sum_{i,j,k} \left(\frac{\partial^3 H_W}{\partial a_i \partial a_j^* \partial a_k^*} \frac{\partial^3 W}{\partial a_i^* \partial a_j \partial a_k} - \frac{\partial^3 H_W}{\partial a_i^* \partial a_j \partial a_k} \frac{\partial^3 W}{\partial a_i \partial a_j^* \partial a_k^*} \right). \tag{3.28}$$

It becomes apparent from this expression that Hamiltonian containing at most quadratic in $\hat{a}$ and $\hat{a}^\dagger$ such as the quantum harmonic oscillator will be rendered exact by the TWA since the terms with third order derivatives will vanish.

Chapter 4

Center-of-mass motion as a sensitive convergence test for variational multi-mode quantum dynamics

4.1 Introduction

Recent advances in the field of ultracold atoms have made it possible to observe the quantum dynamics of few to many particles under unitary time evolution [6]. The opportunity to explain and predict novel effects motivates computational approaches, which face the challenge of vast complexity [57, 58]. Variational multi-mode dynamics seeks to reduce the computational complexity by expanding the wave function with a small number M of optimised mode functions [59–62]. Specifically adapted for bosonic particles is the multi-configurational time-dependent Hartree method for bosons (MCTDHB) [43]. It provides a hierarchy of approxmations beyond the Hartree or Gross-Pitaevskii mean-field theory [63], to which it reduces for $M = 1$. The ability to represent fragmented Bose-Einstein condensates and correlated wave functions for

$M > 1$ is the defining feature of the approach. While the limit of large M formally recovers the multi-particle Schrödinger equation, it is often impossible to verify convergence through increasing M due to prohibitive computational requirements. This motivates the search for independent convergence checks.

Here we test the convergence of MCTDHB simulations by exploiting the artificial coupling of the center-of-mass (COM) and relative motion in the truncated multi-mode expansion. In harmonic external potentials and homogeneous gauge fields, the COM dynamics of a many-particle system is independent of the particle interactions by the generalised Kohn's theorem [64, 65]. Including time-dependent, anisotropic, rotating, or absent trapping potentials of any number of spatial dimensions, this result covers a wide range of experimentally relevant scenarios, where the exact quantum mechanical time evolution of the COM can be easily obtained. Since a convergent simulation is typically required to reproduce the exact COM dynamics, a comparison between both results serves as a sensitive convergence test.

An interesting scenario for quantum dynamics with ultra-cold atoms is provided by attractive bosons in narrowly confining elongated traps, where bright matter-wave solitons of 10^2 to 10^4 atoms have been observed [66–71]. Fragmentation of the Bose-Einstein condensate can be anticipated from theoretical arguments [72], even though experiments have been largely consistent with Gross-Pitaevskii ($M = 1$) theory. The tendency to form many-particle bound states [73], which are themselves well approximated by the Hartree approximation [74], further motivates the use of multi-mode expansions, and several MCTDHB-based studies have been published [75–77]. In this work we find a pathologically slow convergence of the MCTDHB expansion for untrapped or weakly-trapped attractive bosons where the COM length scale becomes of the same order or larger than the typical length scale of relative motion. Specifically, we find that predictions for the dynamical creation of the two-humped, two-fold fragmented states of attractive bosons named "fragmentons" in Ref. [75] were based on unconverged MCTDHB simulations and are inconsistent with the exact COM dynamics. We further find that previously proposed internal convergence checks of

MCTDHB fail to reliably detect unconverged results, including the popular strategy of setting a threshold for the smallest eigenvalue of the single-particle density matrix to estimate the relevance of the least important mode [59, 60, 78].

4.2 Multi-mode expansion for one-dimensional bosons

For definiteness, we consider the dynamics of N bosons of mass m in one dimension with the Hamiltonian

$$\hat{H} = \sum_{i=1}^{N} h(x_i, t) + g(t) \sum_{i<j} \delta(x_i - x_j) = \hat{H}_R + \hat{H}_r, \tag{4.1}$$

where $h(x,t) = -\frac{\hbar^2}{2m}\frac{\partial^2}{\partial x^2} + \frac{1}{2}m\omega(t)^2 x^2$, and $g < 0$ is the coupling parameter of attractive interactions [29]. Due to the harmonic trapping potential the problem is separable and the COM Hamiltonian $H_R = -\frac{\hbar^2}{2Nm}\frac{\partial^2}{\partial R^2} + \frac{1}{2}Nm\omega(t)^2 R^2$ formally defines a single-particle problem in the COM coordinate $R = N^{-1}\sum_i x_i$. The Hamiltonian of relative motion H_r depends only on the $N-1$ distances between particles and commutes with H_R. Thus the time evolution of any observables that are purely related to the COM coordinate is completely independent of the interaction strength. This is very useful for checking the convergence of multi-mode simulations.

The MCTDHB method is based on the variational ansatz for the quantum state

$$|\Psi(t)\rangle = \sum_{n_1,\ldots,n_M} C_{n_1,\ldots,n_M}(t) \prod_{k=1}^{M} \frac{1}{\sqrt{n_k!}} [\hat{b}_k^\dagger(t)]^{n_k} |\mathrm{vac}\rangle, \tag{4.2}$$

with $N = \sum_{k=1}^{M} n_k$ particles. Both the expansion coefficients and the single-particle functions $\phi_k(x,t) = \langle x|\hat{b}_k^\dagger(t)|\mathrm{vac}\rangle$ are time dependent and their evolution equations follow from a variational principle (for details see Ref. [43]). The main parameter determining the accuracy and computational effort of MCTDHB simulations is the number of single-particle modes M. The COM variance $\sigma_R^2 \equiv \langle (R - \langle R\rangle)^2\rangle$ can be obtained from (4.2) through the two-particle density $\rho^{(2)}(x,y) = \langle \hat{\psi}^\dagger(x)\hat{\psi}^\dagger(y)\hat{\psi}(x)\hat{\psi}(y)\rangle$

as [79],

$$\sigma_R^2(t) = \int \frac{x^2 + (N-1)xy}{N^2(N-1)} \rho^{(2)}(x, y; t)\, dxdy. \tag{4.3}$$

Since the expansion (4.2) refers to single-particle quantities rather than the separated COM and relative coordinates, it does not trivially respect the separability. The simulated time evolution of the COM variance will thus be exact in two limits: When the expansion (4.2) is fully converged, or when particle interactions vanish ($g = 0$). In the latter case the MCTDHB time evolution reduces to uncoupled single-particle Schrödinger equations, which can be solved accurately within the chosen discretisation scheme [43]. A simple convergence test is thus obtained by re-running a given simulation with $g = 0$. If the interacting simulation is fully converged, the resulting time evolution of the COM must agree in both cases.

4.3 Interaction dependence of the center-of-mass (COM) variance

It follows from very general principles that observables linked only to the COM wave function are independent of the interaction strength for at most harmonic potentials (meaning $V(x) \propto x^p$ where $p \in \{0, 1, 2\}$) or constant gauge fields. Here we demonstrate this explicitly for the COM variance and a many particle system governed by the Hamiltonian of Eq. (1). For this purpose we write an arbitrary initial quantum state as

$$|\Psi_0\rangle = \sum_{\mu,\nu} c_{\mu\nu} |\chi_\mu\rangle |\Phi_\nu\rangle, \tag{4.4}$$

where $\{|\chi_\mu\rangle\}$ is a complete basis set which depends only on the COM and $\{|\Phi_\nu\rangle\}$ is a complete basis set which depends on the $N-1$ relative motion degrees-of-freedom. We further write the time evolution of the many-body wavefunction as ($\hbar = 1$)

$$|\Psi(t)\rangle = e^{-i(\hat{H}_R + \hat{H}_r)t} |\Psi_0\rangle. \tag{4.5}$$

In Eq. (4.5), the total Hamiltonian was written as $\hat{H} = \hat{H}_R + \hat{H}_r$, where $\hat{H}_R$ is the COM Hamiltonian and the remaining terms, including the interaction-dependent operators, form $\hat{H}_r$. Then we can explicitly write

$$\begin{aligned} |\Psi(t)\rangle &= e^{-i(\hat{H}_R+\hat{H}_r)t} \sum_{\mu,\nu} c_{\mu\nu} |\chi_\mu\rangle |\Phi_\nu\rangle \\ &= \sum_{\mu,\nu} c_{\mu\nu} \Big(e^{-i\hat{H}_R t} |\chi_\mu\rangle \Big) e^{-i\hat{H}_r t} |\Phi_\nu\rangle. \end{aligned} \tag{4.6}$$

The dynamics of the second moment of the COM wave function is obtained as

$$\begin{aligned} &\langle \Psi(t)|\hat{R}^2|\Psi(t)\rangle \\ &= \sum_{\mu',\nu'} \sum_{\mu,\nu} c^*_{\mu'\nu'} c_{\mu\nu} \langle \chi_{\mu'}| e^{i\hat{H}_R t} \hat{R}^2 e^{-i\hat{H}_R t} |\chi_\mu\rangle \\ &\times \Big(\langle \Phi_{\nu'}| e^{i(\hat{H}_r - \hat{H}_r)t} |\Phi_\nu\rangle \Big) \\ &= \sum_{\mu',\mu,\nu} c^*_{\mu'\nu} c_{\mu\nu} \Big(\langle \chi_{\mu'}| e^{i\hat{H}_R t} \hat{R}^2 e^{-i\hat{H}_R t} |\chi_\mu\rangle \Big) \end{aligned} \tag{4.7}$$

.

From the last line of Eq. (4.7) it can be seen that the result is independent of the interaction strength during the time evolution. The time evolution of the COM variance thus depends only on the initial state (through the expansion coefficients $c_{\mu\nu}$) and the external potential through the COM Hamiltonian $\hat{H}_R$. This fact can be used as a sanity check for MCTDHB simulations, which, if fully converged, should produce the same time evolution for the COM variance for different values of the interaction strength.

4.4 Proof of the bounds for the width of the single-particle density

In this section, we are going to prove the bounds for the variance of the exact single-particle density manifested in the shaded region in Fig. 4.4 of the main text. For

systems with a Hamiltonian that is separable in the COM and relative motion coordinate, we can conveniently introduce the following change-of-variables for the COM coordinate R:

$$R = \sum_{j=1}^{N} x_j/N \tag{4.8}$$

and for the relative motion coordinate with $i \geq 2$ [80]:

$$r_i = \sqrt{\frac{i-1}{i}}\left(x_i - \frac{1}{i-1}\sum_{k=1}^{i-1} x_k\right). \tag{4.9}$$

This means that the many-body wave function is given by

$$\Psi(x_1, x_2, \ldots, x_N) = \chi(R)\Phi(r_2, r_3, \ldots, r_N). \tag{4.10}$$

This allows us to write the single-particle density profile as

$$\rho(x_N) = \int_{-\infty}^{\infty} \prod_{j=1}^{N-1} dx_j F(R) G(r_2, r_3, \ldots, r_N), \tag{4.11}$$

where,

$$F(R) = |\chi(R)|^2 \tag{4.12}$$

and

$$G(r_2, r_2, r_3, \ldots, r_N) = |\Phi(r_2, r_3, \ldots, r_N)|^2 \tag{4.13}$$

Note that we can express r_N as:

$$r_N = \frac{N}{\sqrt{N^2 - N}}(x_N - R). \tag{4.14}$$

Then we can transform the integration from $\prod_{j=1}^{N-1} dx_j \to |\mathcal{J}| \prod_{j=2}^{N-1} dr_j dR$, where $\mathcal{J}$ is the corresponding Jacobian. The single-particle density becomes

$$\begin{aligned} \rho(x_N) = |\mathcal{J}| \int_{-\infty}^{\infty} \prod_{j=2}^{N-1} dr_j dR \; F(R) \\ \times G(r_2, r_3, \ldots, \frac{N}{\sqrt{N^2 - N}}(x_N - R)). \end{aligned} \tag{4.15}$$

The $(N-2)$ integrations over dr_j can now be done separately and be used to define a new function

$$H(x_N - R) = |\mathcal{J}| \int_{-\infty}^{\infty} \prod_{j=2}^{N-1} dr_j \times \\ G(r_2, r_3, \ldots, \frac{N}{\sqrt{N^2-N}}(x_N - R)), \tag{4.16}$$

which allows us to write the single-particle density as

$$\rho(x_N) = \int_{-\infty}^{\infty} dR\, F(R) H(x_N - R). \tag{4.17}$$

One can see that indeed the single-particle density profile is just a convolution between the $|\chi(R)|^2$ and another function H that is associated with the relative-motion wave function.

The function H can be further interpreted as the mean-density for a fixed COM position. This can be justified by following Ref. [74]. We write the single-particle density in this case as

$$\rho(x'_N|R) = \int_{-\infty}^{\infty} dx_1 \ldots dx_N \delta\left(R - \sum_{k=1}^{N} x_k/N\right) \\ \times \delta(x'_N - x_N) \left|\Phi\left(\frac{x_2 - x_1}{\sqrt{2}}, \sqrt{\frac{2}{3}}(x_3 - \frac{1}{2}(x_2 + x_1)), \right.\right. \\ \left.\left. \ldots, \sqrt{\frac{N-1}{N}} x_N - \sqrt{\frac{1}{N^2-N}} \sum_{k=1}^{N-1} x_k\right)\right|^2. \tag{4.18}$$

The integration over dx_N can be easily done due to the presence of the δ-function leading to

$$\rho(x'_N|R) = \int_{-\infty}^{\infty} dx_1 \ldots dx_{N-1} \delta\left(R - \sum_{k=1}^{N-1} \frac{x_k + x'_N}{N}\right) \\ \times \left|\Phi\left(\frac{x_2 - x_1}{\sqrt{2}}, \sqrt{\frac{2}{3}}(x_3 - \frac{1}{2}(x_2 + x_1)), \right.\right. \\ \left.\left. \ldots, \sqrt{\frac{N-1}{N}} x'_N - \sqrt{\frac{1}{N^2-N}} \sum_{k=1}^{N-1} x_k\right)\right|^2. \tag{4.19}$$

Again we transform the integration variables using Eq. (4.9) such that $\prod_{j=1}^{N-1} dx_j \to |\mathcal{J}| \prod_{j=2}^{N} dr_j$, where we define

$$r_N = \sqrt{\frac{N-1}{N}}\left(x'_N - \frac{1}{N-1}\sum_{k=1}^{N-1} x_k\right). \tag{4.20}$$

This yields

$$\rho(x'_N|R) = |\mathcal{J}| \int_{-\infty}^{\infty} \prod_{j=2}^{N} dr_j \left|\Phi\left(r_2, \ldots, r_N\right)\right|^2 \tag{4.21}$$
$$\times\, \delta\left(R - x'_N - r_N\sqrt{\frac{N-1}{N}}\right).$$

Lastly, we integrate over the dr_N to find that indeed H is equal to $\rho(x_N|R)$,

$$\rho(x'_N|R) = H(x'_N - R) \tag{4.22}$$

It is straightforward to show that the variances add in a convolution provided that at least one of the functions is centered at the origin (in our case the COM wave function):

$$\begin{aligned}\sigma_n^2 &= \int_{-\infty}^{\infty} (x - \langle x\rangle)^2 (F * H) dx \\ &= \sigma_R^2 + \sigma_r^2\end{aligned} \tag{4.23}$$

where $\sigma_R^2 = \int_{-\infty}^{\infty} x^2 F(x) dx$, $\sigma_r^2 = \int_{-\infty}^{\infty} (x - \langle x\rangle)^2 H(x) dx$ and the functions F and H are normalized to unity. From Eq. (4.23), it can be deduced that the width of the exact single-particle density will always be greater than the width of the COM wave function, $\sigma_R^2 \leq \sigma_n^2$ and the equality is satisfied in the limit of large interaction coupling $g \to \infty$ ($\sigma_r^2 \to 0$). Moreover, the variance of the relative motion density for an untrapped state is smaller than the untrapped case, i.e., $\sigma_r^2 \lessapprox \sigma_{\text{sol}}^2$, where $\sigma_{\text{sol}}^2 = \hbar^4\pi^2/[3g^2m^2(N-1)^2]$ is an excellent approximation of the untrapped relative motion variance that becomes exact for large N [74]. This means that the bounds for the exact single-particle density must be

$$\sigma_R^2 \leq \sigma_n^2 \lessapprox \sigma_R^2 + \sigma_{\text{sol}}^2. \tag{4.24}$$

4.5 Exact solution of the two-particle problem

It is instructive to review some of the exact results for $N = 2$ bosons as we shall use this system later to further test our proposed convergence criterion. The ground state of $N = 2$ particles in a time-independent harmonic trap with frequency ω_0 is described by a product of the center-of-mass (COM) and relative motion wave functions: $\Psi(R, r) = \psi_0(R)\phi_0(r)$. The analytical form of the COM wave function is

$$\psi_0(R) = \left(\frac{2m\omega_0}{\pi\hbar}\right)^{1/4} e^{-m\omega_0 R^2/\hbar} \tag{4.25}$$

where $R = (x_1 + x_2)/2$. On the other hand, the relative motion wave function with the normalization constant A and harmonic oscillator length scale, $\lambda_0 = \sqrt{\hbar/m\omega_0}$, can be obtained as

$$\phi_0(r) = Ae^{-r^2/4\lambda_0^2} U\left(-\frac{\nu}{2}, \frac{1}{2}, \frac{r^2}{2\lambda_0^2}\right), \tag{4.26}$$

where $r = (x_2 - x_1)$ is the relative coordinate, $U(a, b, x)$ is the confluent hypergeometric function of the second kind and ν comes from the discontinuity in the first derivative due to the delta interaction [81]. Explicitly, ν is calculated by solving the transcendental equation

$$\nu = \frac{gm\lambda_0}{\hbar^2\sqrt{2}} \frac{\Gamma(1 - \nu/2)}{\Gamma(1/2 - \nu/2)}. \tag{4.27}$$

The ground-state energy is given by

$$\begin{aligned} E_0^{2,\text{exact}} &= E_{\text{rel}} + E_{\text{COM}} \\ &= \hbar\omega_0\left(\nu + \frac{1}{2}\right) + \frac{\hbar\omega_0}{2} = \hbar\omega_0(\nu + 1), \end{aligned} \tag{4.28}$$

and the exact results for the natural occupancy are obtained by numerically diagonalizing of the single-particle density matrix

$$\begin{aligned} \langle\hat{\psi}^\dagger(x)\hat{\psi}(y)\rangle &= 2\int dz \Psi^*(x, z, t = 0)\Psi(y, z, t = 0) \\ &= 2\int dz \psi_0^*((x + z)/2)\phi_0^*(x - z) \\ &\quad \times \psi_0((y + z)/2)\phi_0(y - z). \end{aligned} \tag{4.29}$$

After turning off the trap, the Gaussian COM wave function expands. In particular, the time evolution of the COM wave function represents the textbook example of Gaussian wave propagation [82]

$$\psi(R,t) \propto \left(1 + i\frac{\hbar t}{m\lambda_0^2}\right)^{-1/2} \times \exp\left(-\frac{R^2}{\lambda_0^2[1 + i\hbar t/(m\lambda_0^2)]}\right). \tag{4.30}$$

The COM wave function spreads leading to a variance increasing quadratically in time

$$\sigma_R^2(t) = \frac{\lambda_0^2}{4}\left[1 + \left(\frac{\hbar t}{m\lambda_0^2}\right)^2\right]. \tag{4.31}$$

The relative motion after trap release, on the other hand, is dominated by the bound state of the attractive δ interactions. Indeed, since the δ function has exactly one bound state, near the origin the relative motion wave function will approach this bound state in the long-time limit and possible other contributions from scattering state will disperse. The initial relative motion wave function can be expressed in terms of the bound state and scattering states: $\phi_0(r) = c_\mathrm{b}\phi_\mathrm{BS}(r) + \int dk e^{ikr} c_k$, where the bound state is $\phi_\mathrm{BS}(r) = \sqrt{\frac{m|g|}{2\hbar^2}}\exp\left(\frac{-m|g||r|}{2\hbar^2}\right)$. Then, the expected variance of the relative motion wave function in the long time limit must be $\sigma_r^2 \geq \sigma_\mathrm{BS}^2 = \int dr r^2 |\phi_\mathrm{BS}(r)|^2 = 2\hbar^4/m^2g^2$.

4.6 Details of the numerical simulations

Numerical simulations were performed with the open-source QiwiB implementation of MCTDHB [83], using standard Runge Kutta time evolution and representing spatial derivatives with five point stencil finite differences. For $N = 2$, we have performed simulations on a 1400 point equidistant grid with different values of the coupling constant g using $L = 30\lambda_0$ as the computational box length for $gm\lambda_0/\hbar^2 \geq -0.7794$ and $L = 14\lambda_0$ for stronger interactions. While for $N = 100$, we have used a 2000 point equidistant grid with $L = 30\lambda_0$ for $gm\lambda_0/\hbar^2 \geq -0.0714$ and $L = 10\lambda_0$ for

stronger interactions. For the time-evolution of the COM variance, we have used 600 point equidistant grid with $L = 25\lambda_0$ for both $M = 9$ and $M = 10$ simulations. We have assured ourselves that the results are converged with respect to changes in these parameters and those of time and space discretization. In addition, we have compared the QiwiB results against an independent implementation of MCTDHB [84], which produced identical results at the reported accuracy. The simulations of the quench dynamics are performed in two steps: (1) relaxation to the ground state of the harmonic trap and (2) time propagation after turning off the trap.

4.7 Simulating quench dynamics

As an example of how we can use the dynamics of the COM as a convergence test, we consider the quantum time evolution of a bright soliton state following Ref. [75]. The initial state is prepared as a simple product state ($M = 1$) of $N = 1000$ bosons with $\phi_1(x, 0) \propto \mathrm{sech}(x/\ell)$, where ℓ is a unit length scale, and the time evolution is simulated with MCTDHB in the absence of a trap [i.e. $\omega = 0$ in Eq. (4.1)] and with $gm\ell/\hbar^2 = -0.008$. The time evolution diagrams of the single-particle density with $M = 1$ and $M = 2$ shown in panels (a) and (b) of Fig. 4.1 are consistent with the previously published results (see Fig. 1 case III in Ref. [75]). The COM variance shown in Fig. 4.1(d) deviates strongly from the exact time evolution and demonstrates that the MCTDHB results are unconverged.

Streltsov *et al.* [75] used the simulation result of Fig. 4.1(b) as evidence for the dynamical formation of two-hump fragmented states. They argued that the simulation corresponds to an interaction quench where the initial state, which is a Gross-Pitaevskii-level approximation to a bright matter wave soliton, is suddenly subjected to increased interactions. While a splitting into two equal-sized fragments or solitons is energetically not possible in the Gross-Pitaevskii equation ($M = 1$), a fragmented Fock state of the form $|N/2, N/2\rangle$ with overlapping two-hump functions $\phi_{1/2}$ is energetically allowed and can be described within the expansion (4.2) with $M = 2$

modes [75]. This argument is consistent with the splitting of the single-particle density into two rapidly parting fragments seen in Fig. 4.1(b), but the exact time evolution of the COM variance is not. The outward motion of the fragments starting shortly after $t = 6\,m\ell^2/\hbar$ goes in hand with a rapid increase of the COM variance as seen by the thin (red) line in 4.1(d), growing to almost two orders of magnitude larger than the exact dynamics of σ_R^2 at $t = 10\,m\ell^2/\hbar$. This leads us to the conclusion that dynamical fragmentation cannot happen in just the way that was described in Ref. [75], but it leaves open the question whether other dynamical processes might favour the formation of "fragmentons". The results of our $M = 3$ simulation [Fig. 4.1(c), (d)], which was not done in [75], shows significant changes compared to the $M = 2$ case and further demonstrates that two modes are not sufficient to describe the exact quantum dynamics. Careful examination of the early-time dynamics of the COM variance in Fig. 4.1(d) reveals an interesting observation: MCTDHB consistently (for $M = 1, 2, 3$) predicts an initial decrease of the COM variance while the exact σ_R^2 increases monotonically. This illustrates the artificial coupling of the COM with the contracting relative coordinates in MCTDHB. However, importantly, the graphs for $M = 2$ and 3 are on top of each other until $t \approx 1\,m\ell^2/\hbar$. Without the knowledge of the exact COM dynamics, judging from the observed succession of MCTDHB results under the assumption that the expansion (4.2) is convergent, one would come to the erroneous conclusion that the observed contraction of the COM variance at early times was a reliable and converged result. The obvious discrepancy with the exact result implies that a conventional convergence check based on observing the absence of change while increasing the mode number M fails in this example. Many more modes would be required to converge the expansion (4.2), which is unfeasible. For this reason it is particularly important to be able to solve the COM dynamics exactly in order to detect these artefacts of the simulation.

In order to better understand the convergence properties of MCTDHB for attractive bosons we consider a closely related, exactly solvable, and experimentally realisable scenario where two bosons are initially prepared in the ground state of a

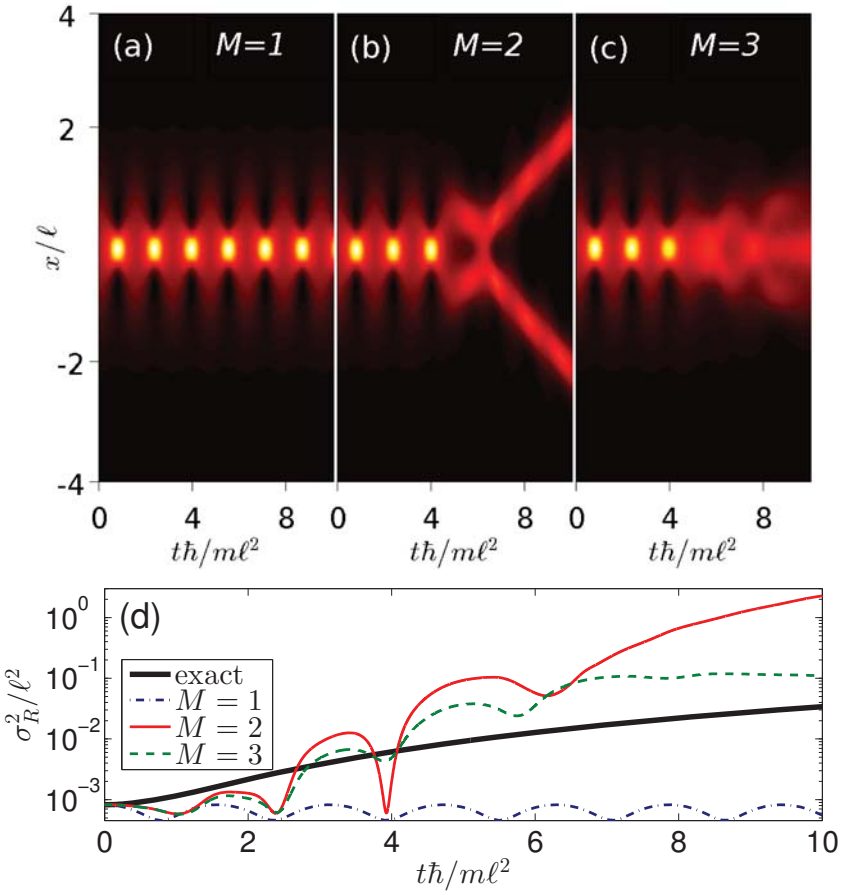

Figure 4.1: (Color online) Time evolution of $N = 1000$ attractive bosons prepared in a product initial state corresponding to a mean-field soliton following Streltsov *et al.* [PRL 100, 130401 (2008)]. (a) – (c) The time evolution of the single-particle density $\langle\hat{\psi}^\dagger(x)\hat{\psi}(x)\rangle$ from MCTDHB simulations for different mode numbers. The $M = 2$ simulation (b) was used [PRL 100, 130401 (2008)] as evidence for the dynamical formation of two-humped fragented quantum states called "fragmentons". (d) The time evolution of the COM variance is compared to the exact result (thick line) from a $g = 0$ simulation.

harmonic trap with frequency ω_0 and released from the trap at $t = 0$. Simulating the dynamics with up to $M = 10$ modes provides a wealth of internal information that

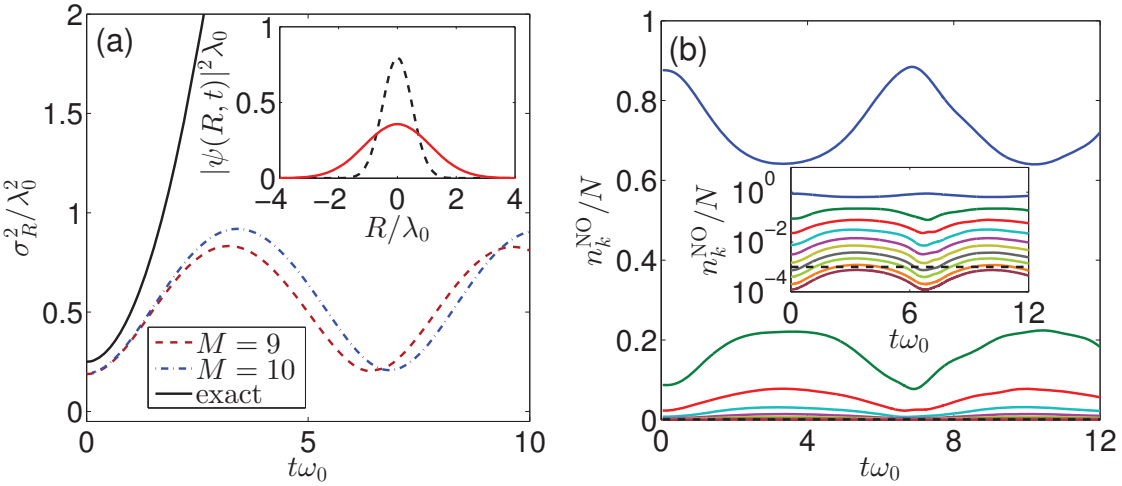

Figure 4.2: Time evolution of $N = 2$ particles after sudden release from a harmonic trap; $gm\lambda_0/\hbar^2 = -3.16$. (a) Center-of-mass variance exact time evolution $\sigma_R^2 = \lambda_0^2(2N)^{-1}[1 + (\hbar t/m\lambda_0^2)^2]$ (full line) and MCTDHB simulation with $M = 10$ modes (broken line) showing unphysical breathing oscillations. Left inset: COM wave function before ($t = 0$, broken line) and after trap release ($t\omega_0 = 2$, full line). (b) Eigenvalues of the single-particle density matrix for the MCTDHB simulation. Right inset: Semi-logarithmic scale showing that the lowest occupancy is below the threshold value 10^{-3} for all times.

can be used to assess the convergence properties of MCTDHB. Figure 4.2 shows the results of an unconverged MCTDHB simulation with $M = 10$ modes.

4.8 Natural occupancy criterion

The relevance of mode functions in the MCTDHB expansion is assessed by examining the eigenvalues $n_k^{\rm NO}$ of the single-particle density matrix, also known as natural occupancies, from $\langle\hat\psi^\dagger(x)\hat\psi(y)\rangle = \sum_{k=1}^{M} n_k^{\rm NO}\varphi_k^*(x)\varphi_k(y)$, where $\sum_k n_k^{\rm NO} = N$ and eigenvalues are ordered by size $n_1^{\rm NO} \geq \cdots \geq n_M^{\rm NO} \geq 0$. A rapidly decreasing sequence of eigenvalues in the exact single-particle density matrix is expected to signal

convergence of the multi-mode expansion (4.2) [59]. Since exact results are usually not available, instead it has become popular to draw conclusions from the natural populations obtained from the variational MCTDHB simulation. A commonly used criterion assumes that the simulation is converged if the smallest relative population lies below a threshold value [1] and recently $n_M^{\mathrm{NO}}/N < 10^{-3}$ has been used for ultra-cold atom experiments [48, 78, 85, 86] (10^{-2} in Ref. [87]). Recently, an alternative convergence check has been proposed where the truncation error during time-evolution is estimated directly, but the scheme has not been implemented yet [88].

The results shown in Fig. 4.2 provide an example where the threshold criterion fails, while comparison of the COM dynamics with exact results clearly shows that the simulation is not converged. Beyond the possibility that simply a smaller threshold value may need to be set, we argue that the logic behind the threshold criterion is flawed because it ignores the possibility that (a) a large number of natural orbitals with very small occupancies can still have an important sum contribution to the density matrix, (b) the natural occupancy of the M-th mode may be underestimated by the variational approach, and (c) the nonlinear evolution equations of MCTDHB may amplify small inaccuracies in the fractional occupancies into large deviations of observables at later times. While good-natured examples were reported in the literature [89, 90] where these problems do not arise, all three possibilities play a role in the breakdown of the criterion for attractive bosons. Specifically, the variational MCTDHB calculation of the trapped ground state (initial state in Fig. 4.2) yields a smallest natural occupancy of $n_{10}^{\mathrm{NO}}/N = 1.2 \times 10^{-4}$ ($M = 10$) compared to the almost four times larger exact value of $n_{10}^{\mathrm{NO}}/N = 4.5 \times 10^{-4}$ (exact), supporting concern (b). It validates point (a) that the cumulative contribution of natural orbitals beyond the 10 highest occupied, $1 - N^{-1} \sum_{i=1}^{10} n_i^{\mathrm{NO}} = 1.4 \times 10^{-3}$ (exact), is an order of magnitude larger than the MCTDHB value for the 10^{th} natural occupancy, confirming that the latter is a poor estimate for the former. Even though these numbers are several orders of magnitudes smaller than unity and a reasonably faithful representation of

[1] In fact, near zero eigenvalues are not desirable and may create numerical instabilities, since the MCTDHB algorithm relies on inverting the single-particle density matrix [43, 60]

the true quantum state might be expected, a 23% deviation of the COM variance from the exact value indicates a poorly converged result instead. Finally re-running the MCTDHB simulation with a slightly modified initial state (optimised to $M = 9$ modes) we indeed find a sensitive dependence on initial conditions as anticipated in point (c) where a change in the breathing frequency and amplitude will lead to completely different values of σ_R^2 after a few periods.

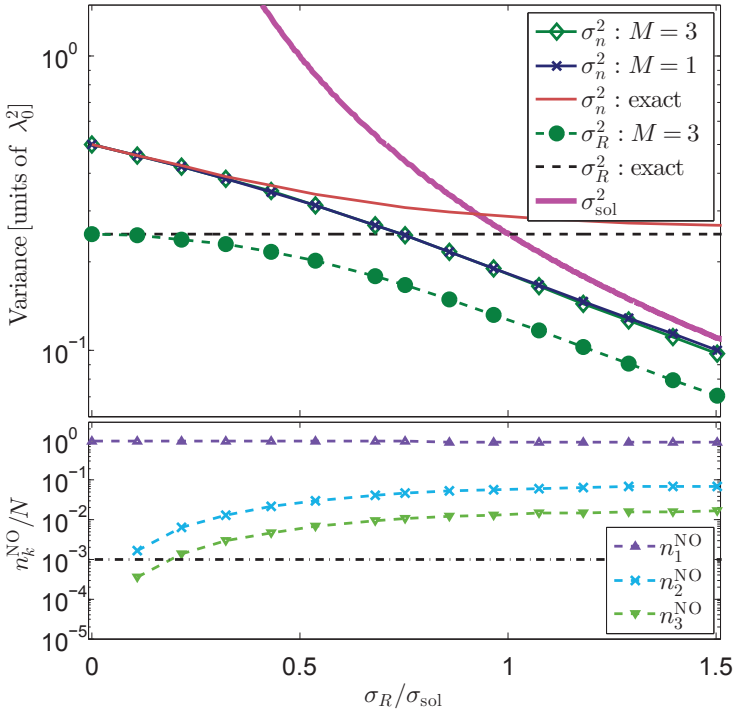

Figure 4.3: Ground state properties of harmonically trapped attractive bosons in one dimension for $N = 2$ particles as a function of the length-scale ratio $\sigma_R/\sigma_{\rm sol}$. The top panel shows the COM variance σ_R^2 and the variance of the single-particle density σ_n^2 from exact and simulated MCTDHB results. For comparison also the soliton variance $\sigma_{\rm sol}^2$ is shown. This relative motion length scale is clearly seen to influence the variational $M = 3$ result in the limit of weak trapping potential.

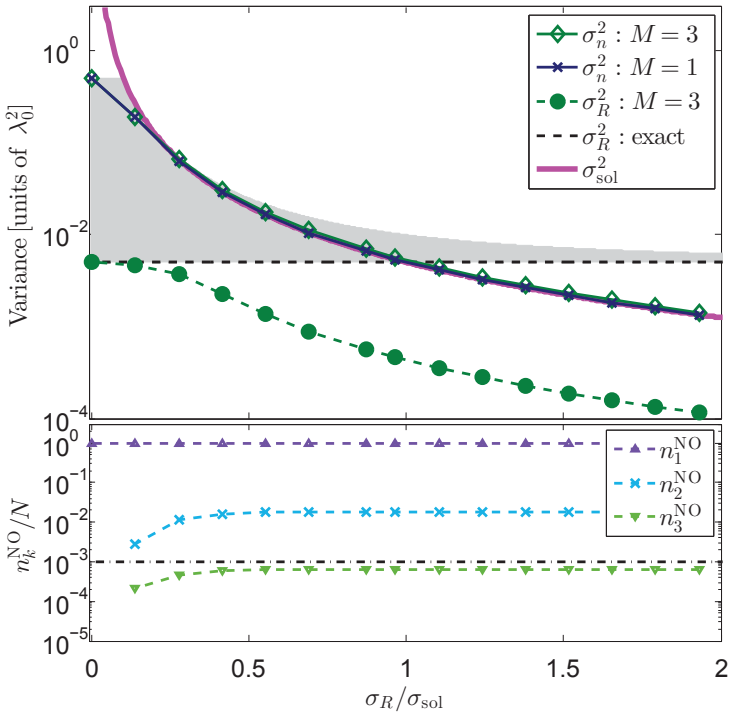

Figure 4.4: Same as Fig. 4.3 with $N = 100$ bosons. The shaded region depicts the known limits for σ_n^2: $\sigma_R^2 \leq \sigma_n^2 \lessapprox \sigma_R^2 + \sigma_{\text{sol}}^2$.

4.9 Role of the particle number

It is instructive to consider the convergence properties of MCTDHB in dependence of the available parameters. In contrast to the repulsive Bose gas, which has a dimensionless interaction parameter [91], the interaction strength scales out for untrapped attractive bosons and the only remaining dimensionless parameter is the particle number N [73]. A second dimensionless parameter is available in a harmonic trap by comparing relevant length scales. The ratio $\sigma_R/\sigma_{\text{sol}}$ allows for a meaningful comparison of results between varying particle number and is thus used for comparing ground state calculations of attractive bosons in Figs. 4.3 and 4.4. Here, $\sigma_R^2 = \lambda_0^2/(2N)$ is the ground state COM variance in the harmonic trap and $\sigma_{\text{sol}}^2 = \hbar^4\pi^2/[3g^2m^2(N-1)^2]$ is the variance of the soliton particle density $\propto \text{sech}^2(\pi x/[2\sqrt{3}\sigma_{\text{sol}}])$ obtained for the

untrapped ground state with $M = 1$ [72], a characteristic length scale determined by particle interactions.

The MCTDHB results for the variance of the single-particle density σ_n^2 and COM variance σ_R^2 of Figs. 4.3 and 4.4 show good agreement with exact results only for $\sigma_R/\sigma_{\mathrm{sol}} \ll 1$, which is a weakly-interacting or strong-trap limit where the harmonic potential dominates all length scales of the quantum state. As soon as the interacting length scale σ_{sol} becomes comparable to or smaller than the COM length scale, significant deviations from exact results occur for the numerically obtained σ_n^2 and σ_R^2. In the weak-trap regime $\sigma_R \gg \sigma_{\mathrm{sol}}$, the deviation can become arbitrarily large.

So could the failure of the MCTDHB approximation be detected by internal criteria, i.e. without comparing to exact results? This appears possible for $N = 2$ particles, where the threshold of 10^{-3} for the lowest occupancy would signal un-converged results for $\sigma_R/\sigma_{\mathrm{sol}} \gtrsim 0.2$. Inspecting the sequence of numerical results with increasing M further indicates that convergence is very slow (see Fig. 4.7). The situation is far worse with $N = 100$ particles, where increasing M further may not be an option due to limited computational resources [2]. Analysis of the natural occupancies provides the consistent picture of an almost pure Bose-Einstein condensate, with the least occupancy well below the threshold. Further, the main observable σ_n^2 displays little variation between $M = 1$ and $M = 3$ on the scale of Fig. 4.4 and clearly shows the same trend as function of $\sigma_R/\sigma_{\mathrm{sol}}$. We are thus led to the conclusion that the detection of spurious results from MCTDHB is much more difficult and may even be impossible without exact results to compare with, for particle numbers of the order of 100 or larger.

[2] Indeed, the number of terms in the expansion (4.2) is given by the binomial coefficient $\binom{N+M-1}{N}$, which changes scaling from $\sim N$ for $M = 2$ to $\sim c^N$ for $M \approx N$, where c depends weakly on N with $2 \leq c \leq 2e$.

4.10 MCTDHB simulations with $N = 2$ particles

Previously, we have demonstrated the ambiguity of the studying the eigenvalues of the single-particle density matrix, the natural occupancies, for a specific MCTDHB simulation. For $N = 2$ particles we are able to vary the number of modes M over a good range, which permits a conventional study of convergence with respect to mode number. It is further possible to analyse the shape of the two-particle wave function in the MCTDHB approximation, which sheds some light on the unphysical coupling of relative and COM motion in the truncated multi-mode expansion.

4.10.1 Convergence of MCTDHB results with increasing M

We test the convergence by checking whether relevant quantities, e.g. the variational ground-state energy, remain unchanged as the number of modes M is increased. The results in Table 4.1 are still varying at the level of several percent between $M = 8$ and $M = 10$ and thus indicate, correctly, that the MCTDHB expansion converges very slowly and is not yet fully converged with 10 modes. While this way of testing convergence is reliable and has produced the correct answer, varying M from one to ten modes is a luxury that can only be afforded for small particle numbers N. In simulations with hundreds to thousands of particles (e.g. [75, 77, 92]), the options for choosing M are severely limited due to the unfavorable scaling of numerical effort when both N and M are large.

We have also considered how the dependence of the COM variance of the trapped ground state on the interaction strength g changes for different numbers of modes M. For brevity, we introduce the dimensionless interaction parameter where $\tilde{g} = gm\lambda_0/\hbar^2$. For $N = 2$, this coupling constant is related to the ratio between relevant length scales via $\tilde{g} = -0.55\ \sigma_R/\sigma_{\mathrm{sol}}$, where the prefactor changes with N. Figure 4.5 compares the COM variance from MCTDHB calculations with the exact result $\sigma_R^2 = \lambda_0^2/4$ from Eq. (2) of the main text. It is apparent that the MCTDHB results deviate severely from the exact values for strongly attractive interaction, and that convergence

	$\tilde{g} = -3.1623$			$\tilde{g} = -2$		
M	$E/\hbar\omega_0$	n_0^{NO}/N	n_1^{NO}/N	$E/\hbar\omega_0$	n_0^{NO}/N	n_1^{NO}/N
1	-0.5787	1	0	-0.0915	1	0
3	-1.1451	0.9342	0.0536	-0.1356	0.9613	0.0316
5	-1.3817	0.9062	0.0701	-0.2244	0.9483	0.0392
8	-1.5546	0.8846	0.0825	-0.2788	0.9387	0.0451
10	-1.6213	0.8761	0.0872	-0.3005	0.9355	0.0470
Exact	-1.9527	0.8251	0.1142	-0.3993	0.9202	0.0563

Table 4.1: Ground state energy E and the two largest natural occupancies from MCTDHB calculations of $N = 2$ trapped bosons.

of the MCTDHB expansion with increasing the number of modes M is exceedingly slow.

In Fig. 4.6, we present the dependence of the natural occupancy on the interaction parameter. A couple of remarks pointing to the ambiguity of this convergence indicator are in order. First, by looking at the results for $M = 10$ and $\tilde{g} = -10$ one is tempted to conclude that MCTDHB has already converged since three orbitals are below 0.1%. But, we know from Fig. 4.5 that for the same interaction strength the MCTDHB COM variance is still far from the exact value. Second, it can be seen that all the natural occupancies, except for the highest one, are shifted up as the number of single-particle modes M is increased. This further exemplifies the failure of the convergence requirement based on the lowest occupancy. For example, the 5th lowest natural occupancy at $\tilde{g} = -2$ is below 0.1% for $M = 5$, while this is not true for $M = 10$, where the 5th single-particle mode is now above the cut-off value.

Lastly, we look at the rate of convergence for observables, in particular the ground state energy and the single-particle density variance, as depicted in Fig. 4.7. We

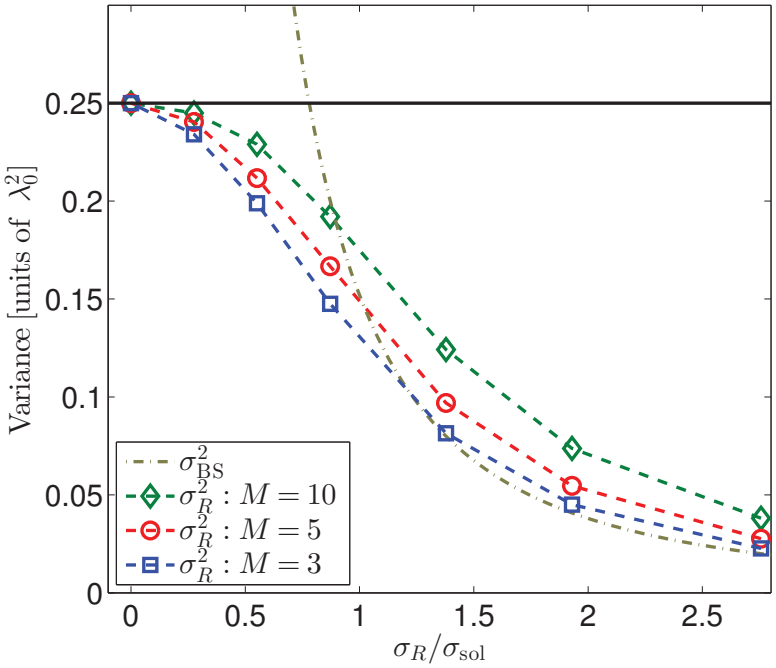

Figure 4.5: COM variance for the trapped ground state for $N = 2$ as a function of the length-scale ratio $\sigma_R/\sigma_{\rm sol}$ from MCTDHB simulations for different values of M (symbols). The solid horizontal line denotes the exact ground-state COM variance $\sigma_R^2 = \lambda_0^2/4$. For comparison, the dash-dotted line shows the exact relative-coordinate variance $\sigma^2_{\rm BS}$ of the two-particle bound state.

find that the MCTDHB results approach the exact values with a slow power law as a function of the number of single-particle modes M, i.e. $|O_{\rm exact} - O_M| \sim M^\nu$. The empirical exponent ν lies between -1 and $-\frac{1}{2}$, which indicates slightly faster convergence than the $-\frac{1}{2}$ leading exponent of the full-CI expansion of two 1D bosons with point interaction in a fixed harmonic oscillator basis [93]. We note that this power-law behavior only sets in for mode numbers larger than $M = 6$ in this case and the convergence rate is significantly slower for smaller M. This may be because the variational optimisation of the modes is particularly effective for small M. It also means, however, that in the pre-power-law regime of $M < 6$ increasing the number of modes brings even less effect than the empirical power law would suggest that governs larger regimes of M. Unfortunately, for particle numbers in the hundreds or larger,

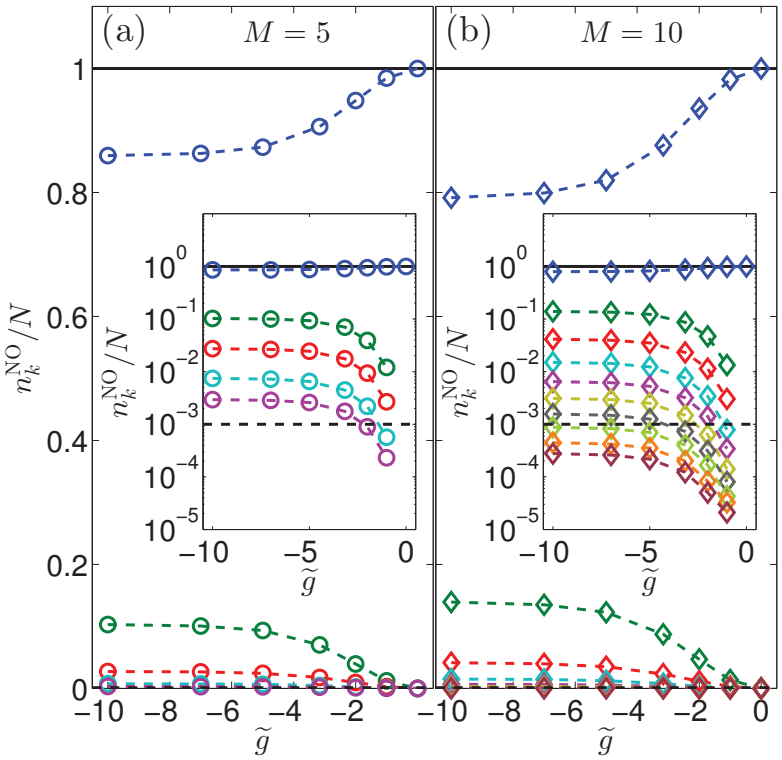

Figure 4.6: Natural occupancies n_k^{NO} for the MCTDHB calculations of Fig. 4.5 for (a) $M = 5$ and (b) $M = 10$. The dashed horizontal line denotes the convergence criterion of $0.1\% = 10^{-3}$ ($N = 2$).

the scaling of computational resources practically limits the application of MCTDHB exactly to the small M regime.

4.10.2 Delocalization of COM: Unphysical coupling of COM and relative motion

In order to understand how MCTDHB deals with the competing length scales and why it violates the separation of COM and relative motion, it is instructive to plot the two-particle density, as shown in Fig. 4.8 for $N = 2$. In these plots, the diagonal ($x = y$) represents the COM coordinate R and the antidiagonal ($x = -y$) the relative motion coordinate r. While the left hand panels relate to the ground state of $\tilde{g} = -1$,

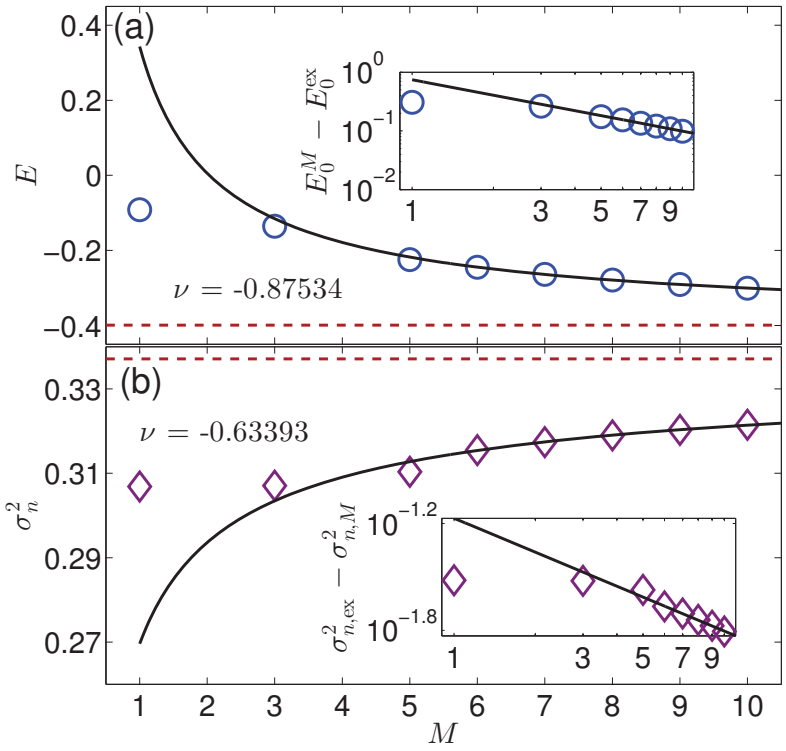

Figure 4.7: Convergence with increasing number of modes M for $N = 2$ with $\tilde{g} = -2$: (a) Ground-state energy and (b) single-particle density variance. Dashed horizontal lines correspond to the exact values. Symbols denote the MCTDHB results for different M. The exponent of the power law fit, ν, is also shown. (Inset) Log-log plot of the absolute difference between the exact and MCTDHB results.

the right hand panels relate to a later time $t\omega_0 = 30$ after trap release. Here the COM wave function has expanded significantly according to Eq. (4.31), whereas the relative-motion bound state is hardly changed. The upper two panels show the exact result and panel Fig. 4.8(b) clearly demonstrates the diverging length scales. Note the changing spatial scale between panels Figs. 4.8(a) and 4.8(b).

The middle panels Figs. 4.8(c) and 4.8(d) present the $M = 1$ (Gross-Pitaevskii) result. At this level, the COM and relative motion length scales are identical because the product form of the state with a single mode function $|\Psi(x, y)|^2 = |\phi(x)|^2|\phi(y)|^2$ together with the inversion symmetry of the problem forces a four-fold symmetry and leaves no option to distinguish the two diagonal directions. For long times, the wave

function expands in both directions and the COM and relative motion length scales are identical.

The lower panels Figs. 4.8(e) and 4.8(f) report an MCTDHB simulation with $M = 5$ modes. The trapped ground state in Fig. 4.8(e) is approximated better than with $M = 1$, although some more detailed features are missing. The long-time profile in Fig. 4.8(f) shows five separated peaks with each one exhibiting a four-fold symmetry and resembling the $M = 1$ result, albeit on a different scale. As the MCTDHB expansion is a sum over symmetrized product states, different numbers of modes M will produce up to M peaks with diagonal – off diagonal symmetry. Thus for given M, the COM and relative motion are strongly coupled and expansion dynamics, where the COM length scale grows over time, will not be captured correctly. Furthermore, this discretised behavior due to finite M leads to an impractical number of M needed to correctly model the limit of a delocalised COM but localised relative motion.

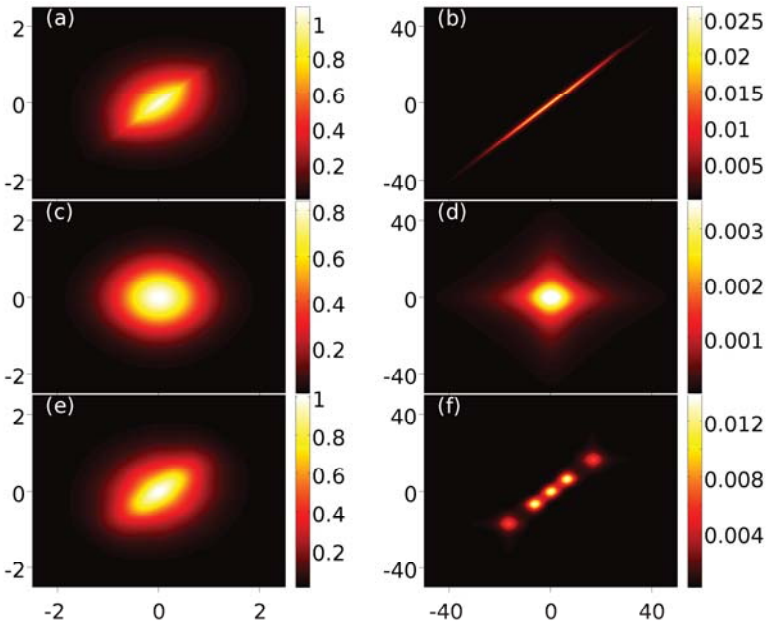

Figure 4.8: Two-particle density $\rho^{(2)}(x, y) = 2|\Psi(x, y)|^2$ for $N = 2$ with $\tilde{g} = -1$ at different times: Left [(a),(c),(e)] $t\omega_0 = 0$ and right [(b),(d),(f)] $t\omega_0 = 30$. Comparison between [(a),(b)] exact, [(c),(d)] Gross-Pitaevskii ($M = 1$), and [(e),(f)] $M = 5$.

4.11 Discussion and Conclusions

Why is MCTDHB unable to capture the physics of the weak trap regime while the Hartree approximation ($M = 1$) is known to reproduce the exact, untrapped ground state energy to leading order for large N [74], and previous work has found MCTDHB to converge nicely at large N [90]? The Hartree approximation fails to describe the delocalisation of the COM in the untrapped limit [72] because the variational principle, conditioned to minimise the total energy, finds the best compromise in localising the single available mode function $\phi_1(x)$. When a finite number $M > 1$ is used in the multi-mode expansion, it is still energetically advantageous to localise the mode functions. Indeed, an infinite number of mode functions is needed to represent a state with delocalised COM but bound relative motion (see Fig. 4.7).

In conclusion, we have demonstrated how easily obtainable, accurate results for the COM variance were useful in detecting unconverged results and in demonstrating the failure of several popular internal convergence checks of MCTDHB. The possible dynamical creation of "fragmentons" is re-opened for discussion as numerical evidence in Ref. [75] turned out spurious. Our findings call for a systematic re-evaluation of the available convergence criteria for numerical quantum dynamics and what is required to claim "numerically exact" results [45, 78, 87, 94, 95]. The comparison of COM dynamics with independent, exact results may be useful for other numerical methods of quantum dynamics and is available in any spatial dimensions and for any particle statistics as long as external potentials are at most harmonic.

Chapter 5

Interaction blockade for bosons in an asymmetric double well

5.1 Introduction

The high controllability of ultracold atoms provide a natural testbed for observing both novel and well-established quantum many-body phenomena [6]. Exquisite control in the level of single neutral atoms has been demonstrated in experiments such as single-atom trapping [12], laser cooling to the quantum mechanical ground state [96, 97], and demonstration of the Hong-Ou-Mandel effect [98]. These technological developments in the manipulation of low-entropy quantum states have paved the way for unique opportunities to observe the emergence of many-body effects as the number of atoms is gradually increased [13, 14].

The strength of the interaction between particles often dictates the nonequilibrium properties as a consequence of its effect on the available quantum states in a many-body system. Such an example for electrons in quantum dots is the Coulomb blockade phenomenon wherein an applied gate voltage enables exactly one electron to tunnel into the dot [99–102]. For neutral atoms, a similar phenomenon can be seen in the so-called Rydberg blockade where only a single atom out of many is excited within a blockade radius due to strong dipole-dipole interaction between atoms in

Rydberg states [103–107]. When a similar blockade phenomenon is achieved by short-range interactions between neutral atoms, e.g. for tunneling dynamics in a double-well potential, it is known as *interaction blockade* [108–115]. It is a direct analog of the Coulomb blockade in electronic transport, except that the blockade is mediated by the van-der-Waals interactions between neutral atoms instead of the Coulomb force. A particular example is a double-well potential with a small number of strongly-interacting atoms. Tilting the double-well can offset intra-well interactions and gives rise to discrete plateaus in the population of a well corresponding to integer particle numbers [114]. The plateaus originate in the finite energy cost for adding a particle to a well and the need to satisfy a resonance condition to allow particles to coherently move between the wells. When the resonance condition is met, coherent oscillations of a single particle between the wells are possible, and the oscillation frequency is proportional to the splitting of energy eigenstates at an avoided level crossing.

An interesting question concerns the frequency of coherent oscillations in the blockade regime where only a single particle is allowed to tunnel due to the presence of strong interactions. Simple quantum mechanical arguments imply that the oscillation frequency scales with the square root of the number of particles present if the particles are bosons. Such a bosonic enhancement factor of $\sqrt{N}$ was observed in Rydberg blockade experiments when N excitable atoms were present by measuring the Rabi frequency [104–107]. In interaction blockade experiments with double-well potentials, however, the bosonic enhancement factor has not been observed directly so far. Instead, a different particle-number dependence of the oscillation frequency was observed [115]. The reason is attributed to the fact that the shape of the double-well potential, in particular the effective tunneling barrier, changes when adjusting the tilt to compensate for the interaction energy brought by different particle numbers [115, 116]. The motivation for the current work is to propose an improved experimental design that can overcome these limitations and allow for the bosonic enhancement factor to be measured directly from the frequency of coherent oscillations.

In this work, we study few-body dynamics in an asymmetric double well. We demonstrate by means of numerical simulations the feasibility of observing the expected $\sqrt{N}$ scaling behavior of the oscillation frequencies, or equivalently the energy splittings, in the interaction blockade limit. Specifically, we propose to use an asymmetric double well configuration formed by superimposing multiple optical tweezer potentials. We then simulate the full quantum system for up to $N = 3$ bosons in the three-dimensional trapping geometry using the multiconfigurational time-dependent Hartree method for bosons (MCTDHB) [43], obtaining good agreement with a reduced description in terms of an effective Bose-Hubbard dimer model. The paper is organized as follows: Section 5.2 contains a brief introduction of the interaction blockade phenomenon as understood from the Bose-Hubbard model and an analytical prediction from this dimer model for deviations from the expected $\sqrt{N}$ behavior due to finite interaction strengths; Section 5.4.1 describes important considerations in constructing the three-dimensional optical tweezer potentials used in our study; Section 5.4.3 presents the main numerical results on the avoided level crossings for $N = 2$ and $N = 3$ together with the nature of the relevant resonance states and how the energy splittings compare with the bosonic enhancement factor predicted in the interaction blockade regime. This section also contains fidelity calculations and time-dependent results for $N = 2$ aimed at validating our suggested protocol; Section 5.5 gives a short summary of our findings, technical details for possible experiments, and an outlook. We have also included an appendix for a short description of the MCTDHB method and a discussion of implemented convergence checks for the numerical approach as well as the determination of effective interaction parameters.

5.2 Bose-Hubbard model

The phenomenon of interaction blockade in ultracold gases was first observed experimentally in an array of double wells [114]. The simplest theoretical description is obtained in a tight-binding model, which leads to a two-mode Bose-Hubbard (or

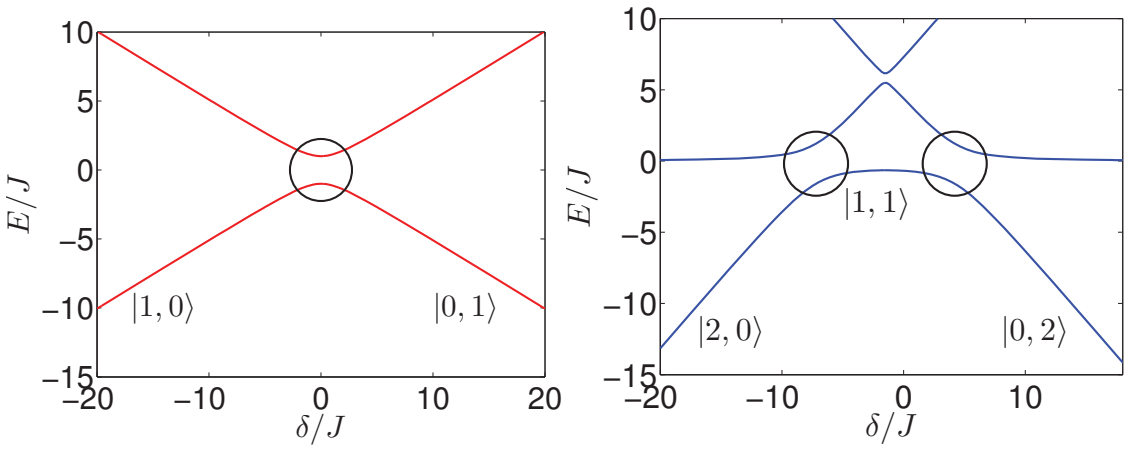

Figure 5.1: Level structure within the Bose-Hubbard model for (left) $N = 1$ and (right) $N = 2$. Rapid quench to the position of the anti-crossing will induce coherent oscillations with a frequency proportional to the inverse of the energy splitting. The parameters are: $U_L/J = 7$, $U_R/J = 4$.

Lipkin-Meshkov-Glick model [30]) type Hamiltonian [114] given by

$$\hat{H} = -\sum_{\ell \neq \ell'} J \hat{b}_\ell^\dagger \hat{b}_{\ell'} + \sum_\ell \frac{U_\ell}{2} \hat{n}_\ell (\hat{n}_\ell - 1) + \sum_\ell \epsilon_\ell \hat{n}_\ell, \tag{5.1}$$

where $\hat{b}_\ell^\dagger$ and $\hat{b}_\ell$ are bosonic creation and annihilation operators with $\ell \in \{L, R\}$ denominating the left and right well, respectively, and $\hat{n}_\ell$ is the number operator on site ℓ. The tunneling between the two wells is characterized by J, the on-site interaction coupling is U_ℓ, and the on-site single-particle energy is ϵ_ℓ.

For a fixed value of U_ℓ/J, avoided level crossings can be found between different eigenstates of the system when the double well is tilted, which corresponds to a relative shift of the on-site single-particle energies $\delta \equiv \epsilon_L - \epsilon_R$. Examples for $N = 1$ and $N = 2$ are shown in Fig. 5.1. Away from the avoided crossings, the levels simply correspond to integer occupation numbers in each well. Rapidly ramping the shift δ into the middle of any one of the avoided crossings marked by circles in Fig. 5.1 will initiate coherent oscillations that correspond to a single particle tunneling between the two wells.

As we will see in detail below, an interesting effect in the interaction blockade

regime is that the scaling of the multiparticle energy splitting is given by the bosonic enhancement factor:

$$\Delta E = \sqrt{N} 2J, \tag{5.2}$$

where $\Delta E \equiv E_2 - E_1$ is the energy difference between the the first-excited and ground-state energies for N bosons. Note however that Eq. (5.2) is only formally true in the limit of infinite interaction strength on one of the sites $U_\ell/J \to \infty$. In order to show this, we express the Hamiltonian matrix using Fock states $|N-n, n\rangle$, where $n \in [0, N]$ is the number of bosons in the right well and $N - n$ is the remaining bosons on the left well. The basis states are arranged in order of increasing number of bosons in the right well, i.e., $|N-n, n\rangle \in \{|N, 0\rangle, |N-1, 1\rangle, \ldots, |0, N\rangle\}$. The full Hamiltonian matrix corresponding to Eq. (5.1) reads

$$H = \left(\begin{array}{c|c} A & B \\ \hline B^\dagger & H_{\mathrm{res},N} \end{array}\right) \tag{5.3}$$

where

$$A = \begin{pmatrix} \frac{U_L N(N-1)}{2} + \frac{N\delta}{2} & -J\sqrt{N} & \cdots & 0 \\ -J\sqrt{N} & \ddots & \cdots & \vdots \\ \vdots & \vdots & \ddots & \vdots \\ 0 & \cdots & \cdots & U_L + \frac{U_R(N-2)(N-3)}{2} + (2 - \frac{N}{2})\delta \end{pmatrix} \tag{5.4}$$

$$B = \begin{pmatrix} 0 & 0 \\ \vdots & \vdots \\ \vdots & \vdots \\ -J\sqrt{2(N-1)} & 0 \end{pmatrix} \tag{5.5}$$

$$H_{\mathrm{res},N} = \begin{pmatrix} \frac{U_R(N-1)(N-2)}{2} - \frac{(N-2)\delta}{2} & -J\sqrt{N} \\ -J\sqrt{N} & \frac{U_R N(N-1)}{2} - \frac{N\delta}{2} \end{pmatrix} \tag{5.6}$$

Focussing on the lower right corner of the matrix in Eq. (5.3), it becomes apparent that the diagonal elements become degenerate when $\delta = U_R(N-1)$. Under this condition the energy of a state with a single boson in the left well matches or becomes resonant

with the energy of the interacting bosons all being in the right well. If, additionally $U_L/J \to \infty$, the rest of the matrix decouples and, after subtracting the degenerate energy value of the diagonal elements, the low-energy Hamiltonian reduces to the 2×2 matrix

$$H_{\mathrm{res},N} = \begin{pmatrix} 0 & -J\sqrt{N} \\ -J\sqrt{N} & 0 \end{pmatrix}, \tag{5.7}$$

which has eigenvalues reproducing the energy difference of Eq. (5.2).

The eigenstates of the resonant Hamiltonian (5.7) correspond to the ground and first-excited states of the system. They are symmetric and asymmetric superposition of the Fock states $|0, N\rangle$ and $|1, N-1\rangle$, respectively. This means that if an initial state $|\Psi(t=0)\rangle$ is either $|0, N\rangle$ or $|1, N-1\rangle$, the dynamical behavior is expected to exhibit coherent oscillations between these two states. For example if $|\Psi(t=0)\rangle = |0, N\rangle$, the time evolution of the many-body wave function follows from

$$\begin{aligned} |\Psi(t)\rangle &= e^{-iHt/\hbar}|\Psi(t=0)\rangle \\ &= \cos(\sqrt{N}Jt/\hbar)|0, N\rangle - i\sin(\sqrt{N}Jt/\hbar)|1, N-1\rangle. \end{aligned} \tag{5.8}$$

The state in Eq. (5.8) physically represents the tunneling of a single boson between the two wells.

It should be noted that the conditions of resonance $\delta = U_R(N-1)$, and large interactions $U_L/J \to \infty$, are difficult to satisfy in symmetric double-wells where $U_R = U_L$ because the large required tilt δ would necessarily lead to a distortion of the potential. It is therefore sensible to consider an asymmetric double-well potential, as will be done in the following section.

If the conditions for the reduction to the 2×2 matrix (5.7) are not strictly met, avoided level crossings can still be found at appropriate values of the tilt δ where coherent oscillations are possible with a frequency given by $\Delta E/2\hbar$. Experimental realisations with finite on-site interaction energy U_ℓ, e.g., were reported in Refs. [114, 115]. It turns out that the blockade criteria can be "softened" by using finite but sufficiently strong interaction strengths $U_L/J \gg 1$, which leads to an enhancement factor very close to $\sim \sqrt{N}$ as shown in Fig. 5.2.

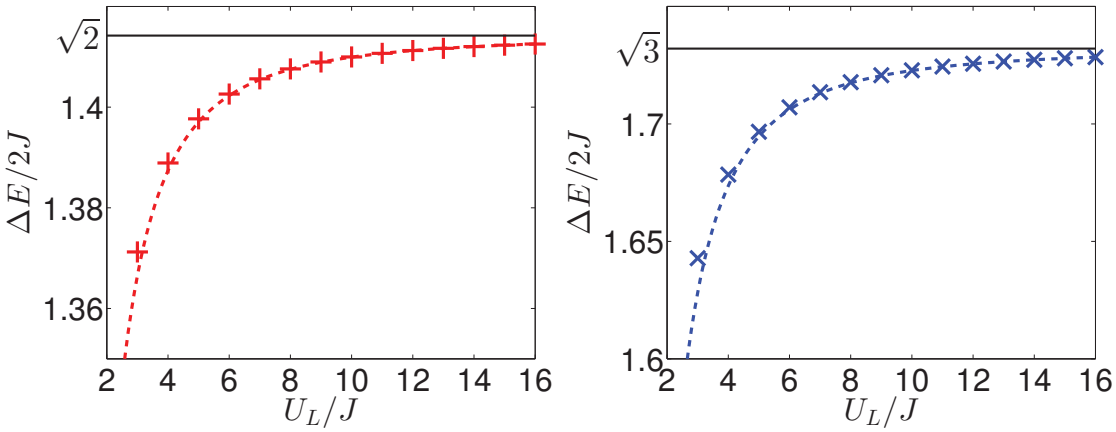

Figure 5.2: Energy splittings at tunneling resonances involving single boson tunneling for $N = 2$ (left) and $N = 3$ (right). Markers correspond to numerical results from exact diagonalization of the full Hamiltonian. Solid lines correspond to the expected $\sqrt{N}$ scaling in the interaction blockade limit. Broken lines denote the result of first-order perturbation in Eq. (5.15). Other parameter: $U_R = 4U_L/7$.

The deviation of the energy splittings $\Delta E/2J$ from from the $\sqrt{N}$ behavior due to finite U_L/J can be understood using perturbation theory as follows. The Hamiltonian matrix in Eq. (5.3) can be partitioned according to the vertical and horizontal lines and the energy eigenvalues E and eigenstates can be found by solving:

$$H \begin{pmatrix} x \\ y \end{pmatrix} \equiv \left(\begin{array}{c|c} A & B \\ \hline B^\dagger & H_{\mathrm{res},N} \end{array} \right) \begin{pmatrix} x \\ y \end{pmatrix} = E \begin{pmatrix} x \\ y \end{pmatrix}, \tag{5.9}$$

which in terms of y reduces to:

$$Ey = \left[H_{\mathrm{res},N} + B^\dagger (E - A)^{-1} B \right] y. \tag{5.10}$$

The second term on the right hand side of Eq. (5.10) can be treated as a perturbative correction to $H_{\mathrm{res},N}$. Since U_L is large, we can further approximate that the leading order contribution of $(E - A)^{-1}$ will come from the lowest eigenvalue of A, which can be approximated by $A_{mm} = U_L + U_R$. Moreover, we approximate the eigenvalue E on the right hand side of Eq. (5.10) as the eigenvalues of $H_{\mathrm{res},N}$ which are $E^{(0)} =$

$\{-J\sqrt{N}, J\sqrt{N}\}$. This turns the problem into solving the eigenvalue problem

$$Ey = \begin{pmatrix} \frac{J^2 2(N-1)}{E^{(0)}-A} & -J\sqrt{N} \\ -J\sqrt{N} & 0 \end{pmatrix}. \tag{5.11}$$

This can be easily solved by hand and the eigenvalues are

$$\frac{E}{J} = \frac{(N-1)}{\left(\frac{E^{(0)}}{J} - \frac{A}{J}\right)} \pm \sqrt{N + \frac{(N-1)^2}{\left(\frac{E^{(0)}}{J} - \frac{A}{J}\right)^2}}. \tag{5.12}$$

After substituting the appropriate $E^{(0)}$, the energies are

$$\frac{E_\pm}{J} = \frac{(N-1)}{\left(\pm\sqrt{N} - \frac{A}{J}\right)} \pm \sqrt{N + \frac{(N-1)^2}{\left(\pm\sqrt{N} - \frac{A}{J}\right)^2}}. \tag{5.13}$$

Then, the energy splitting between the ground- and first-excited states $\Delta E = E_+ - E_-$ is

$$\frac{\Delta E}{2J} = \frac{(N-1)\sqrt{N}}{N - A^2/J^2} + \frac{1}{2}\left[\sqrt{N + \frac{(N-1)^2}{\left(\sqrt{N} - A/J\right)^2}} + \sqrt{N + \frac{(N-1)^2}{\left(\sqrt{N} + A/J\right)^2}}\right]. \tag{5.14}$$

This expression can be further simplified by binomial expansion of the two terms inside the square brackets and retaining the two lowest order terms. Finally, the energy splitting according to a first-order approximation for finite U_ℓ/J reads

$$\Delta E/2J \approx \sqrt{N}\left[1 - \frac{1}{2}\left(\frac{N^2-1}{N^2}\right)\eta^2 + \mathcal{O}(\eta^4)\right], \tag{5.15}$$

where the small parameter in the above series expansion is given by

$$\eta \equiv \frac{\sqrt{N}J}{(U_L + U_R)}, \tag{5.16}$$

which is obviously small for large interaction coupling strength U_L that we consider here. Note that $\eta \to 0$ in the limit $U_L/J \to \infty$ such that we recover the expected bosonic enhancement factor $\sqrt{N}$ as per Eq. (5.2). Good agreement between the prediction of Eq. (5.15) and the numerical result from exact diagonalization is seen in Fig. 5.2

The bosonic enhancement factor can be verified in experiments from measurements of the period of coherent oscillations between states representing the tunneling of a single particle between the wells [115]. For the simplest case of $N = 1$, a boson will undergo coherent oscillations according to $\langle \hat{n}_L(t) \rangle = \cos^2(Jt/\hbar)$, such that the single-particle tunneling period is just $t_{\text{Tun}}^{N=1} = h/(2J)$.

For interacting bosons with finite but large U_L/J, observing coherent oscillations between $|0, N\rangle$ and $|1, N-1\rangle$ is still possible in the presence of appropriate avoided level crossings. To see this, consider the Hamiltonian H with eigenvalues $\{E_k\}$ and eigenstates $\{|k\rangle\}$ wherein $|1\rangle$ ($|2\rangle$) denotes the ground (first-excited) state with E_1 (E_2) ground-state (first-excited state) energy. We can write the time evolution of an initial many-body state $|\Psi(0)\rangle = |n_0\rangle$ as

$$\begin{aligned} |\Psi(t)\rangle &= e^{-iHt/\hbar}|n_0\rangle \\ &= e^{i\Delta Et/(2\hbar)}C_{n_0}^1|1\rangle + e^{-i\Delta Et/(2\hbar)}C_{n_0}^2|2\rangle \\ &+ \sum_{k' \notin \{1,2\}} e^{-iE_{k'}t/\hbar}e^{-i\xi t/\hbar}C_{n_0}^{k'}|k'\rangle, \end{aligned} \tag{5.17}$$

where $C_{n_0}^k = \langle k|n_0\rangle$ and we shift the many-body energies by $\xi = -(E_2+E_1)/2$ in order to have $E_2+\xi = \Delta E/2$ and $E_1+\xi = -\Delta E/2$. Let us now consider an initial localized state, say for example $|n_0\rangle = |0, N\rangle$, which has a large overlap with the symmetric superposition of the two lowest eigenstates $|0, N\rangle \approx (|1\rangle + |2\rangle)/\sqrt{2}$. In addition, the corresponding antisymmetric superposition is $|1, N-1\rangle \approx (|1\rangle - |2\rangle)/\sqrt{2}$. These would mean that the overlaps are small $\{|C_{n_0}^{k'}|\} \ll 1$ between the initial state and the remaining eigenstates $k' \notin \{1, 2\}$. In this case, the rest of the terms in the last line of Eq. (5.17) has negligible contribution and thus, the wave function will evolve as

$$|\Psi(t)\rangle \approx \cos\left(\frac{\Delta Et}{2\hbar}\right)|0, N\rangle - i\sin\left(\frac{\Delta Et}{2\hbar}\right)|1, N-1\rangle. \tag{5.18}$$

Notice how this expression resembles Eq. (5.8) but with a subtle yet important distinction that in Eq. (5.18), we are not approximating the Hamiltonian with the 2×2 matrix Eq. (5.7). But instead, we have to obtain the many-body energy splitting

$\Delta E = E_2 - E_1$ from the full Hamiltonian H. From Eq. (5.18), we find that the tunneling period can be approximated by $t^N_{\rm Tun} = h/(\Delta E)$.

One of the key aspects not captured by the simple Bose-Hubbard theory is that the tunneling parameter J may change when particle number is changed due to the need to adjust the tilt δ to locate the resonances. The effect becomes particularly severe in symmetric double well systems obtained in optical lattices, where $U_L \approx U_R \gg J$ as in Refs. [114, 115]. The inadvertent change of J was considered the reason for observing a faster oscillation frequency than the expected $\sqrt{2}$ enhancement for doubly occupied sites in Ref. [115].

5.3 Effective Bose-Hubbard parameters

In this section, we briefly discuss the recipe for calculating the effective Bose-Hubbard parameters according to Ref. [28]. The first step is to obtain a set of $\tilde{M}$ single-particle eigenfunctions $\{\psi_1, \psi_2, \ldots, \psi_{\tilde{M}}\}$ for a specific realization of the 3D potential. Specifically for our simulations, we are using the sinc-DVR basis [28] with the same grid size and box size as described in Section 5.4.2. We seek linear combinations of these states to write the localized or "Wannier" function as

$$\phi_\ell(\mathbf{r}) \equiv \phi(\mathbf{c}, \mathbf{r}) = \sum_{i=1}^{\tilde{M}} c_i^\ell \psi_i(\mathbf{r}), \tag{5.19}$$

where $\mathbf{c} \cdot \mathbf{c} = 1$. Following the prescription for construction of localized Wannier functions in [28], we calculate the localization functional

$$\mathcal{L}(\psi_i, \psi_j) = \int dy\ dz \int_{-\infty}^{x_{\rm cut}} dx \psi_i^*(\mathbf{r}) \psi_j(\mathbf{r}), \tag{5.20}$$

where $x_{\rm cut}$ defines the left well say the position of the local maxima at $x = 0$. Both $\mathbf{c}$ and the set of single-particle states must satify the condition

$$\max\ \mathcal{L}[\phi(\mathbf{c}, \mathbf{r}), \phi(\mathbf{c}, \mathbf{r})]. \tag{5.21}$$

Alternatively, this condition can be written as

$$\max\ \mathbf{c} \cdot \mathbb{L} \cdot \mathbf{c}, \tag{5.22}$$

where we define the localization matrix as

$$\mathbb{L}_{ij} = \mathcal{L}[\psi_i(\mathbf{r}), \psi_j(\mathbf{r})]. \tag{5.23}$$

Thus, the vector $\{c_i^\ell\}$ in Eq. (5.19), which maximizes the localization in the ℓ-site, is one of the $\tilde{M}$ eigenvectors of the localization matrix. In this work, we truncate this expansion and use only the two lowest single-particle eigenstates, i.e., $\tilde{M} = 2$. For a symmetric double-well potential, we recover for the $\mathbf{c}$ vectors the symmetric and anti-symmetric superposition of the two lowest-lying single-particle energy states, $(1,1)^{\mathrm{T}}/\sqrt{2}$ and $(1,-1)^{\mathrm{T}}/\sqrt{2}$, respectively. This procedure allows us to construct the two localized Wannier functions ϕ_ℓ for arbitrary choice of potentials. We can then obtain the effective Bose-Hubbard parameters using the two lowest single-particle modes. The tunneling term is obtained from

$$J = \int d\mathbf{r} \phi_\ell^*(\mathbf{r}) \left[\frac{-\hbar^2}{2m} \nabla^2 + V(\mathbf{r}) \right] \phi_{\ell'}(\mathbf{r}), \tag{5.24}$$

where $\ell \neq \ell'$. The on-site energies are given by

$$\epsilon_\ell = \int d\mathbf{r} \phi_\ell^*(\mathbf{r}) \left[\frac{-\hbar^2}{2m} \nabla^2 + V(\mathbf{r}) \right] \phi_\ell(\mathbf{r}). \tag{5.25}$$

The on-site interactions are given by

$$U_\ell = \frac{4\pi\hbar^2 a_s}{m} \int d\mathbf{r} |\phi_\ell(\mathbf{r})|^4. \tag{5.26}$$

where a_s is the s-wave scattering length and for our simulations we use $a_s = 5.45$ nm.

5.4 Interaction blockade in asymmetric double well

We now show that one can use an asymmetric double well to observe the $\sqrt{N}$ bosonic enhancement factor according to Eq. (5.2). Specifically, we propose to disentangle the single-particle coupling parameter J from the tilt δ by using an asymmetric double well potential formed from the optical dipole potential of three laser beams (optical tweezers) far red-detuned off the closest atomic resonance such that they provide conservative attractive potentials for the atoms proportional to the local light intensity.

Two closely spaced laser beams will combine to form a wide (right) well while the other laser beam will serve as a narrow (left) well separated by a small barrier. An example of such configuration is depicted in Fig. 5.3. We further suggest to probe the avoided level crossings by changing the intensity of the laser beam farthest (right-most) from the effective barrier. Tuning this intensity will almost only affect the right-most region of the potential, effectively adjusting the bias ϵ_R, while leaving the barrier region responsible for the single-particle coupling J mostly unaffected. Another advantage of using an asymmetric configuration is that the effective on-site interaction energy in the wide well will be naturally smaller than the other well, i.e., $U_R < U_L$. Thus, the resonance condition can be achieved with relatively little change on the depth of the right-most potential when compared to the symmetric double well case.

5.4.1 Optical tweezer potential

Here, we discuss one possible experimental realization of such an asymmetric double well trap. In particular, we consider a superposition of multiple 3D optical dipole potentials modeled by [28]

$$V(\mathbf{r}) = -\sum_{i=1}^{P} \frac{V_i}{1+\frac{z^2}{z_R^2}} \exp\left[-\frac{2((x-x_i)^2+y^2)}{w_0^2\left(1+\frac{z^2}{z_R^2}\right)}\right] + mgy, \tag{5.27}$$

where m is the mass of the bosonic atom, g is the gravitational acceleration $g = 9.81\ \mathrm{m/s^2}$, P is the number of laser beams utilized in the trap, $\{V_i\}$ ($\{x_i\}$) are the depths (positions) of each beam, w_0 is the beam waist, and $z_R = \pi w_0^2/\lambda$ is the Rayleigh range, with λ being the wavelength of the laser. The double-well shape in the 3D potential Eq. (5.27) is introduced along the x-direction. We also include the gravitational potential along the y-direction for the sake of completeness even though the overall effect is relatively small. In the following discussion, we have used experimentally relevant parameters for the mass m of a ^{85}Rb atom, the beam waist

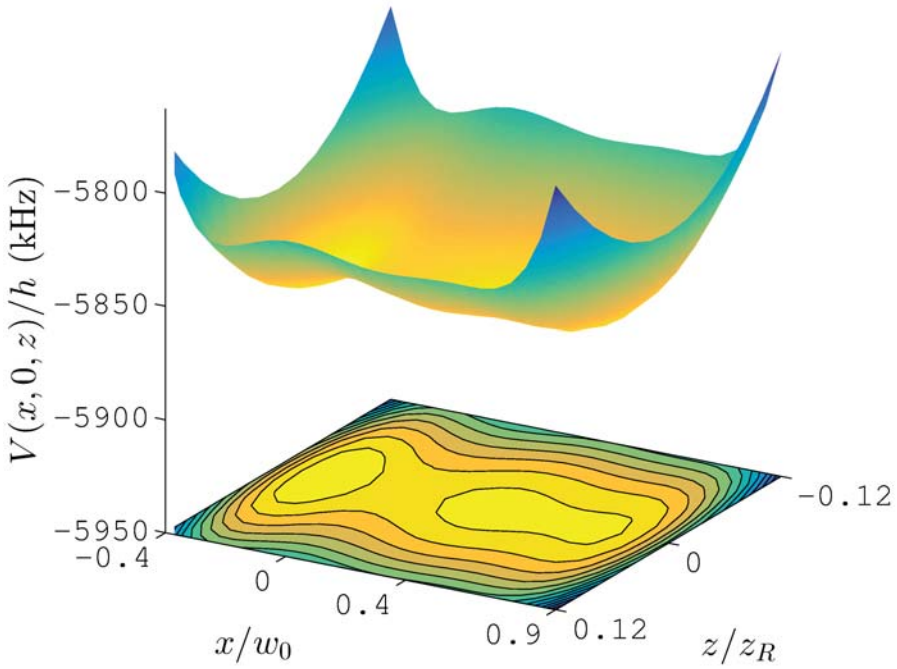

Figure 5.3: Asymmetric double well optical tweezer at the $x-z$ plane. Shown is the potential $V(r)$ of Eq. (5.27) formed with $P = 3$ laser beams for parameter values: $\{V_i/h\}$ (kHz) $= \{4659.775,\ 4137.962,\ 4585.886\}$ and $\{x_i/w_0\} = \{-0.658,\ 0.264,\ 1.176\}$.

$w_0 = 1.015\ \mu$m, and the laser wavelength $\lambda = 1.064\ \mu$m. Since the background s-wave scattering length for ^{85}Rb is negative [117,118], the scattering length has to be tuned via Feshbach resonance [8] and instead we use $a_s = 5.45$ nm. Although not presented here, we have checked that the main findings of our work are robust against changing the isotope by repeating our calculations for ^{87}Rb.

The parameter space becomes fairly complex when we consider at three or more optical tweezer beams in the system because of the different possible combinations of depths $\{V_i\}$ and positions $\{x_i\}$ of the beams. To narrow down the search for suitable trap parameters we first consider a symmetric double well with a potential along the

x-axis ($y = z = 0$) given by

$$V(x,0,0) = -V_0\left[\exp(\frac{-2(x+d)^2}{w_0^2}) + \exp(\frac{-2(x-d)^2}{w_0^2})\right], \tag{5.28}$$

where here we set $V_1 = V_2 = V_0$. Note that at a separation of $d = w_0/2$ the two wells will merge. In practice, there are two important considerations that need to be taken care of: (i) reaching the interaction blockade regime of $U \gg J$, and (ii) the energy splitting is large enough to be experimentally observed. For the first condition, we choose $U/J \sim 10$. For the second condition we choose a minimum energy splitting of $\Delta E/h \sim 200$ Hz, which corresponds to 5 ms of oscillation period, being motivated by experimental requirements. The effective Bose-Hubbard parameters (J, U) are calculated following the prescriptions of Ref. [28] with further details given in Sec. 5.3. We find that a suitable choice of $V_0/h = V_1/h = 5$ MHz satisfies both conditions. In Fig. 5.4, we show the single-particle energy splitting ΔE and interaction energies U_ℓ as a function of the double well separation.

The same two constraints for the symmetric configuration will also apply for the asymmetric double well when exploring the parameter space. We impose an additional criterion for the separation between the second and third laser beams: it must be separated as far as possible but the single-particle functions must still be delocalized between the combined well. In practice, the aforementioned conditions will effectively fix the spacings $\{x_i\}$ and the intensities of the beams forming the wide well $\{V_i\}$.

5.4.2 MCTDHB and Convergence

The numerical simulations are performed using the MCTDHB method. Our calculations are done using the implementation in the MCTDHB-Laboratory package [84]. Here, we briefly describe the theory behind MCTDHB. We also discuss how we ascertain the numerical convergence of the MCTDHB results.

The MCTDHB method uses a variational ansatz for the many-body wave function,

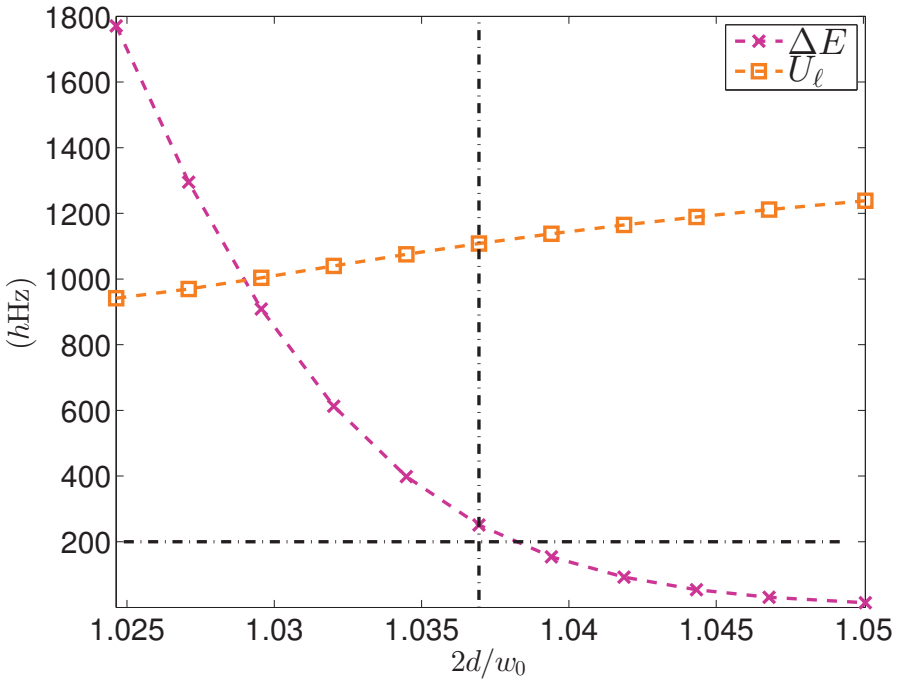

Figure 5.4: Single-particle energy splitting ΔE for $N = 1$ and intra-well interaction energy $U_\ell = U_L = U_R$ of a symmetric double with two optical tweezer beams as a function of the beam separation d with $V_0/h = 5$ MHz. The horizontal dashed-dotted line represents the minimum energy splitting for experimentally observable single-particle tunneling.

which must be properly symmetrized for bosons

$$|\Psi(t)\rangle = \sum_{n_1} \cdots \sum_{n_M} C_{n_1,n_2,\ldots,n_M}(t) \prod_{k=1}^{M} \frac{1}{\sqrt{n_k!}} [\hat{b}_k^\dagger(t)]^{n_k} |\text{vac}\rangle, \tag{5.29}$$

where ϕ_k is the set of single-particle functions $\phi_k(x,t) = \langle x|\hat{b}_k^\dagger(t)|\text{vac}\rangle$. Using Lagrangian formulation, the functional action reads

$$\begin{aligned} &S[\{C_{\vec{n}}(t)\}, \{\phi_k(x,t)\}] \\ &= \int dt \Big\{ \langle\Psi|\hat{H} - i\frac{\partial}{\partial t}|\Psi\rangle \\ &- \sum_{k,j=1}^{M} \mu_{k,j}(t)[\langle\phi_k|\phi_j\rangle - \delta_{kj}] \Big\}, \end{aligned} \tag{5.30}$$

where the Lagrange coefficients μ_{kj} ensure orthonormality of the single particle functions. Variations with respect to the time-varying expansion coefficients and $\{\phi_k\}$ yield a set of coupled equations of motion, which are numerically solved. Further details on the derivation can be found in [43]. The main convergence parameter in MCTDHB simulations is the number of single-particle modes M used in the expansion of the many-body wave function. The importance of the single-particle functions used to expand the MCTDHB wave function can be evaluated from the eigenvalues n_k^{NO} of the single-particle density matrix, sometimes called as natural occupancies, $\langle\psi^\dagger(x)\psi(y)\rangle = \sum_{k=1}^{M} n_k^{\mathrm{NO}}\phi_k^*(x)\phi_k(y)$. In the subsequent discussion, we have normalized the trace of the density matrix to unity, i.e., $\sum_k n_k^{\mathrm{NO}} = 1$. Furthermore, the excited eigenstates and eigenvalues shown in Fig. 5.8 are obtained from the time-dependent Hamiltonian matrix calculated when performing the variational optimization of the $C_{\vec{n}}$ vectors with respect to the ground-state wave function. We have checked that the eigenenergies obtained this way are consistent with those calculated from the variationally optimized first-excited state wave functions. This procedure of obtaining the eigenspectrum using improved relaxation method has been recently applied in another work based on MCTDHB simulations [53].

To exemplify how we test for numerical convergence of our results, we discuss below a specific example for $N = 2$. Relaxation towards the variationally optimized ground-state wave function is done within MCTDHB through imaginary time propagation [43]. For our MCTDHB simulations, we have used a fast Fourier transform based grid with $\{N_x, N_y, N_z\} = \{60, 30, 30\}$ number of grid points in a box defined by $x/w_0 \in [-0.5, 1.0]$, $y/w_0 \in [-0.4, 0.4]$, and $z/w_0 \in [-0.4, 0.4]$. We have checked that relevant properties of the low-lying energy states such as the energy splitting ΔE are converged with respect to this discretization. Another important consideration here is the unphysical nature of the contact (or delta) interaction for 3D systems. That is, one can show that the scattering length evaluates to zero for dimensions greater than one when calculated via the standard T-matrix formalism [119, 120]. A simple workaround to this problem, which is tailor-made for numerical methods in truncated

Hilbert space like in MCTDHB, is to renormalize the coupling constant of the interaction potential according to the energy cut-off considered in the calculation [119]. We present in Table 5.1 the values of the renormalized interaction couplings Λ used in our MCTDHB simulations.

	$M=2$	$M=3$	$M=4$
$\tilde{\Lambda}$	0.0707128	0.0718848	0.0731065
	$M=5$	$M=6$	$M=7$
$\tilde{\Lambda}$	0.0743990	0.0749100	0.0754298

Table 5.1: Dimensionless renormalized interaction strength $\tilde{\Lambda} = \Lambda m w_0^2/\hbar^2$, where Λ is the renormalized coupling strength of the contact interaction, for various M.

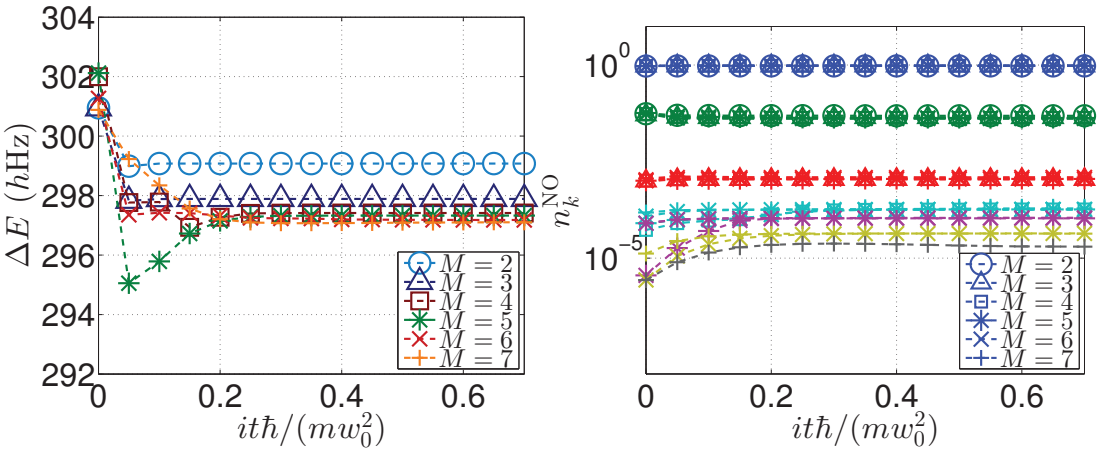

Figure 5.5: Relaxation using imaginary time propagation within MCTDHB for $N=2$ (^{87}Rb) at the avoided crossing. (Left) the energy difference between the ground and first-excited state. (Right) Natural occupancies of the ground-state single-partice density matrix.

Since we are interested in the energy splitting between the two lowest energy states, we show in Fig. 5.5 the energy difference ΔE as a function of imaginary

time for different single-particle modes M. It can be seen that already for $M = 4$ and $M = 5$, the energy splitting has nicely converged. Moreover, this also confirms that the renormalization procedure described above has worked. The time-evolution of the natural occupancies of the ground-state single-particle density matrix is also shown in Fig. 5.5. The convergence towards the relaxed energy splitting coincides with an increase in the fourth lowest natural occupancy. This observation reveals the importance of using at least $M = 4$ modes in MCTDHB to simulate the stationary states of the system. It is insightful to look at the natural orbitals for $M = 4$ shown in Fig. 5.6. The symmetry of the external potential along the y-direction is trivially reflected in the symmetric nature of the orbitals about the y-axis. The x-direction or the axis of asymmetry is more interesting since here we can see from the nature of the two lowest occupied natural orbitals that MCTDHB needs at least $M = 4$ modes in order to capture the finer details of the external potential brought about by the fact that two optical tweezers actually form the wider well. This is apparent from the presence of nodal structures in the region occupied by the wide well as depicted in the plots in the bottom panel of Fig. 5.6. Multi-mode generalizations of a bosonic Josephson junction [121–124] have been explored in various works demonstrating the importance of going beyond the two-mode approximation provided by the two lowest single-particle modes in order to predict novel quantum phenomena [18, 26, 44–46, 50, 111, 125].

Recently, pathologically slow convergence of MCTDHB results was demonstrated for nonequilibrium dynamics of attractively interacting bosons in the absence of an external trap [19]. However, for the system considered in this work, convergence from using a relatively fewer number of single-particle modes M is to be expected due to tight three-dimensional trapping geometry leading to a large separation of the two lowest single-particle energies from the rest of the spectrum as seen from Fig. 5.7. Moreover, the bosons are repulsively interacting and the external trap is always present in our simulations. Good agreement with the Bose-Hubbard results for $N = 2$ as shown in Fig. 5.8 further validates the applicability of MCTDHB for

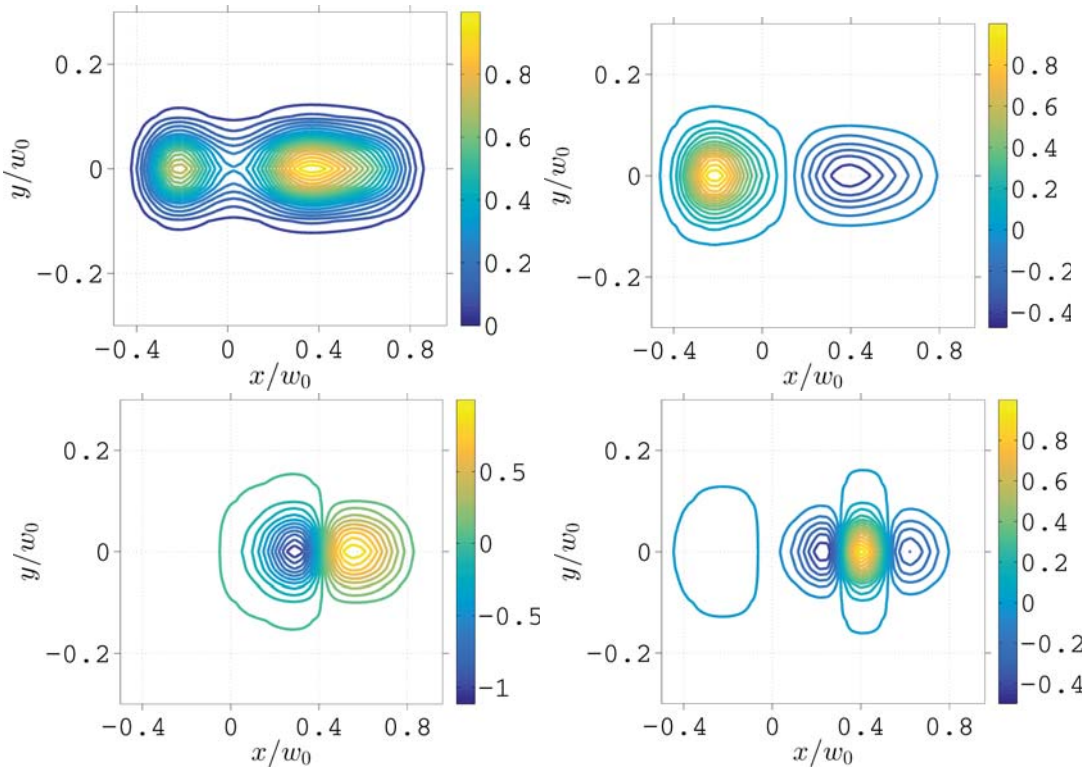

Figure 5.6: Slice of the natural orbitals for the ground-state at the avoided crossing of $N = 2$ and $M = 4$ at $z = 0$ as a function of x and y. Top-Left: highest occupied orbital; Top-Right: second highest occupied orbital; Bottom-Left: third highest occupied orbital; Bottom-Right: least occupied orbital. We have checked that the general features of the four highest occupied orbitals remain unchanged even for $M = 7$.

the type of problem considered here.

5.4.3 Few particle quantum simulations

To illustrate our suggested scheme, we choose a particular set of parameters $\{x_i, V_i\}$. Afterward, the tunneling resonance for a single boson is located by tuning the depth of the narrow well V_1. The single-particle energies as a function of V_1 are shown in Fig. 5.7. For the asymmetric double well, the single-particle energy splitting between the two lowest states is $\Delta E/h = 2J/h = 240.14$ Hz, which leads to a tunneling period

of $t_{\mathrm{Tun}} = 4.16$ ms. It can also be seen in the left panel of Fig. 5.7 that the second- and third-excited states are well separated from the ground and first-excited states. This motivates us to use the MCTDHB scheme [43] for fully 3D numerical simulations when $N > 1$. The MCTDHB method expands a multi-particle wave function in an occupation number basis constructed from a small number M of optimised orthonormal single-particle functions. A short description of the MCTDHB method and additional details on the numerical convergence can be found in Section 5.4.2. An alternative method is to diagonalize the corrresponding Bose-Hubbard Hamiltonian for N bosons using the effective Bose-Hubbard parameters calculated according to the prescription of Ref. [28] as the beam depth is being varied. The Bose-Hubbard parametrization for the asymmetric double well is discussed briefly in Section 5.3. In this context, the full $(N+1) \times (N+1)$ Hamiltonian matrix is constructed and diagonalized in the Fock state basis.

For the MCTDHB calculations, the three-dimensional nature of the system requires a careful treatment of the short-range interaction

$$\hat{U}(\mathbf{r}_i - \mathbf{r}_j) = \Lambda \delta(\mathbf{r}_i - \mathbf{r}_j), \tag{5.31}$$

where Λ is the renormalized coupling constant, used in our simulations (see Refs. [119, 120] and references therein). As discussed in Section 5.4.2, the main convergence parameter in MCTDHB is the number of single-particle modes M used to represent the MCTDHB many-body wave function. To this end, for each choice of M, we follow the renormalization procedure utilized in Refs. [119, 126, 127] when renormalizing the interaction strength with respect to the exact ground-state energy of interacting bosons in a 3D harmonic oscillator [81] solved using the same spatial grid as the asymmetric double well potential. Another way of modelling short-range interactions is by using finite-range model potentials such as a Gaussian interaction potential as in Ref. [120]. But as we shall see below for $N = 2$ bosons, renormalizing the strength of the contact potential is already sufficient to get good agreement between the results of the MCTDHB simulations and the Bose-Hubbard model with the unrenormalized contact parameter $4\pi\hbar^2 a_s/m$.

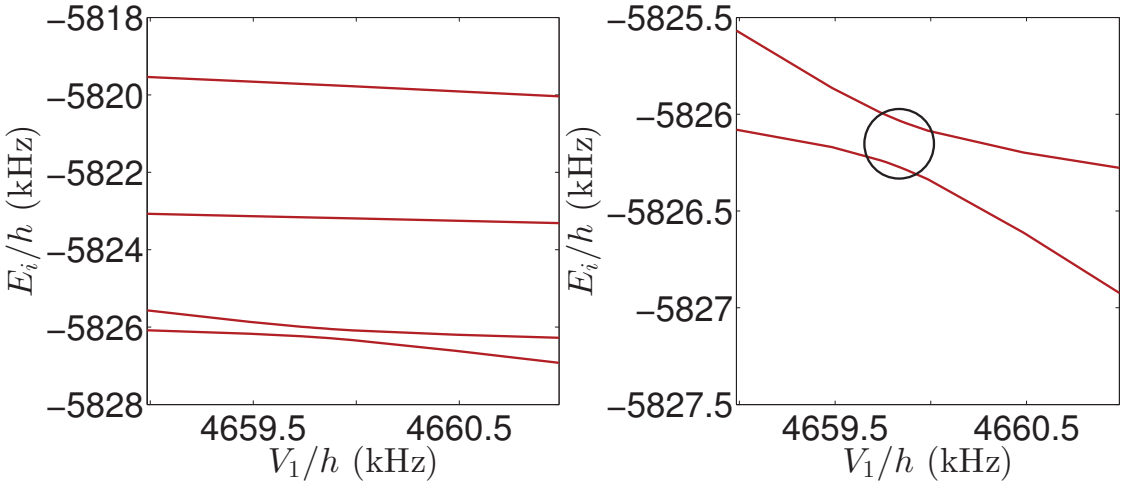

Figure 5.7: Single-particle energies in the asymmetric double well trap as a function of the left-most laser beam depth V_1: (left) First four single-particle energies and (right) Zoom-in of to the ground and first excited energies. The single-particle resonance identified from an avoided level crossing is indicated by the circle.

Now that the value of V_1 is fixed by the resonance condition for $N = 1$, we implement our protocol of varying V_3 to identify the avoided level crossing for $N > 1$. The results for the multi-particle eigenenergies are shown in Fig. 5.8. We have obtained energy splittings at the avoided level crossing of $\Delta E/h = 336.46$ Hz for $N = 2$ and $\Delta E/h = 395.62$ Hz for $N = 3$. Interestingly, the two lowest multi-particle energies from the effective Bose-Hubbard model are consistent with the corresponding MCTDHB results for the parameter space explored here. The deviation seen for the second-excited state energy can be explained by the fact that in our MCTDHB calculations only the ground or the first-excited state is variationally optimized and thus, the second-excited state energy is expected to be higher than the exact energy. We can then infer that the renormalization scheme from Ref. [119] and the MCTDHB method are both applicable for characterizing the energy gap between the two lowest energy states for the system considered here.

Due to the three-dimensional nature of the potential, it is imperative to ensure that the avoided level crossings in Fig. 5.8 correspond to the relevant states and

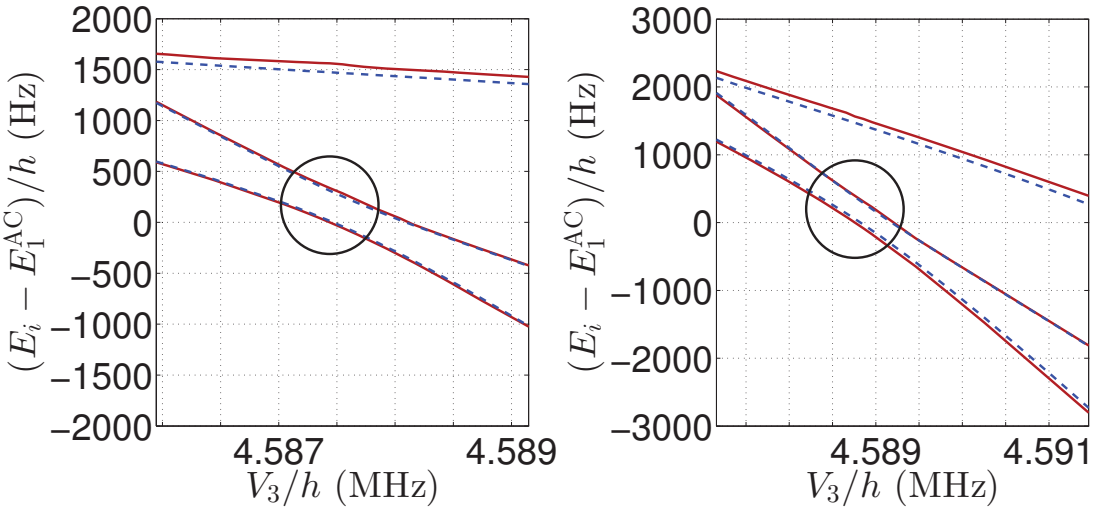

Figure 5.8: Ground, first-, and second-excited states as a function of V_3 for the asymmetric double well for (left) $N = 2$ and (right) $N = 3$. The reference ground-state energies are $E_1^{\mathrm{AC}}/h = -11.653$ MHz for $N = 2$ and $E_1^{\mathrm{AC}}/h = -17.480$ MHz for $N = 3$. Solid lines correspond to MCTDHB results. Broken lines correspond to diagonalization of the Bose-Hubbard Hamiltonian. Resonances are indicated in circles.

excitations along the axis of asymmetry. To this end, we show plots of the two-body wave function as depicted in Fig. 5.9. In these plots, it can be seen that the first-excited state has a node along the x-axis at the position where the effective barrier has a maximum. Features of the wave function of the first-excited state shown in the right panel of Fig. 5.9 are insightful in understanding the nature of the excited states at the avoided level crossing. On one hand, the positive amplitude of the wave function for positive values of x_1 and x_2 (upper-right quadrant) describes a state of two bosons sitting on the wide well. On the other hand, the negative amplitude in the remaining domain of negative x_1 with positive x_2 and vice versa depicts a state with one boson in each well. Therefore, this excited state $|\Psi_1\rangle$ represents the antisymmetric superposition of the localized wave functions $|\Psi_1\rangle = (|0,2\rangle - |1,1\rangle)/\sqrt{2}$. A similar analysis can be made for the ground-state wave function $|\Psi_0\rangle$ shown in the left panel of Fig. 5.9, leading to the conclusion that the ground state of the system corresponds to

the symmetric superposition state $|\Psi_0\rangle = (|0,2\rangle + |1,1\rangle)/\sqrt{2}$. Thus, the states which physically represent a single boson tunneling from one well to the other are manifested in the two lowest eigenstates of the system. In a similar fashion, we can also look at

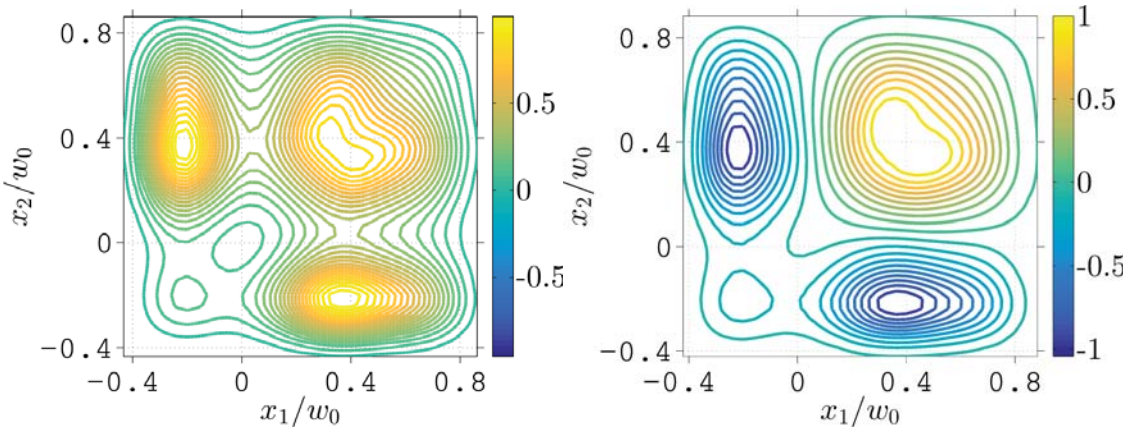

Figure 5.9: Slice of the two-particle wave function for $N = 2$ at $y_1 = y_2 = y_3 = z_1 = z_2 = z_3 = 0$ as a function of x_1 and x_2. Left: ground state; Right: first excited state.

the corresponding three-body wave function for $N = 3$. The important features of the isosurface plots shown in Fig. 5.10 can be regarded as simple three-dimensional (corresponding to three bosons $\{x_1, x_2, x_3\}$) extension of the contour plots in Fig. 5.9. We see that the two lowest energy states obtained are the relevant anti-crossing states in the numerical simulation for $N = 3$.

5.4.4 Fidelity calculation between MCTDHB wave functions

In order to ensure that the dynamics of an initial localized state will be restricted to the two-state subspace at the avoided level crossing, we must choose an initial state with strong overlap with the symmmetric superposition of two lowest few-body eigenstates $|1\rangle$ and $|2\rangle$ at the resonance. This can be quantified by the fidelity $\mathcal{F} = |\langle\Psi_R|\Psi_0\rangle|^2$ where $|\Psi_R\rangle = (|1\rangle + |2\rangle)/\sqrt{2}$.

In order to make sure that the suggested protocol in measuring the enhancement

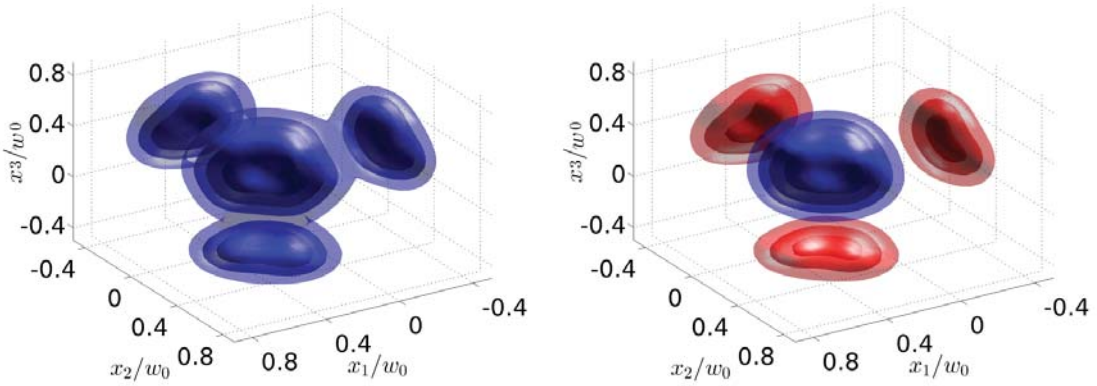

Figure 5.10: Three-particle wave function for $N = 3$ at $y_1 = y_2 = y_3 = z_1 = z_2 = z_3 = 0$. The blue surfaces correspond to positive values while the red surfaces correspond to negative values of the wave function. (left) ground state and (right) first-excited state.

factor is sensible, we have suggested to calculate the fidelity

$$\mathcal{F} = |\langle \Psi | \chi \rangle|^2. \tag{5.32}$$

For brevity, we will drop the time-dependence on the wave functions since we are only interested in overlaps between relaxed or stationary states. Moreover, we shall assume that both MCTDHB wave functions use the same number of single-particle modes M. In this case, the MCTDHB wave functions can be written as

$$|\Psi\rangle = \sum_n C_n |n\rangle \tag{5.33}$$
$$|\chi\rangle = \sum_m B_m |m\rangle,$$

where

$$|n\rangle = \prod_{k=1}^{M} \frac{[\hat{b}_k^\dagger]^{n_k}}{\sqrt{n_k!}} |0\rangle \tag{5.34}$$

and

$$|m\rangle = \prod_{k=1}^{M} \frac{[\hat{d}_k^\dagger]^{m_k}}{\sqrt{m_k!}} |0\rangle. \tag{5.35}$$

The bosonic creation operators create a boson in a single-particle function according to

$$\begin{aligned} \hat{b}_k^\dagger|\mathrm{vac}\rangle &= |\phi_k\rangle \\ \hat{d}_k^\dagger|\mathrm{vac}\rangle &= |\varphi_k\rangle. \end{aligned} \tag{5.36}$$

Obtaining the fidelity equates to calculation of the overlap

$$\langle\Psi|\chi\rangle = \sum_{m,n} C_n^* B_m \langle n|m\rangle \tag{5.37}$$

In general, we can easily access the variationally optimized expansion coefficients C_n and B_m. However, obtaining the overlaps $\langle n|m\rangle$ is not trivial because the basis functions between two different MCTDHB wave functions are in most cases not orthonormal, i.e., $\langle\phi_i|\varphi_k\rangle \neq \delta_{i,k}$. In order to proceed further, we expand both of the single-particle functions $|\phi_i\rangle$ for $|n\rangle$ and $|\varphi_i\rangle$ for $|m\rangle$ in terms of a primitive basis $\{\zeta_j\}$ defined by the chosen grid discretization scheme. Note that we are now assuming that the two wave functions are solved in the same underlying primitive basis. Then, we can write

$$|\phi_i\rangle = \sum f_{ij}|\zeta_j\rangle \tag{5.38}$$

and

$$|\varphi_i\rangle = \sum g_{ij}|\zeta_j\rangle. \tag{5.39}$$

Since each of the single-particle basis functions form an orthonormal set, we can then calculate the overlap matrix that can be used to expand one single-particle function in terms of the other

$$\begin{aligned} |\varphi_i\rangle &= \sum_k |\phi_k\rangle\langle\phi_k|\varphi_i\rangle = \sum_{k,\ell} f_{k\ell}^* g_{i\ell}|\phi_k\rangle \\ &= \sum_k A_{ki}|\phi_k\rangle, \end{aligned} \tag{5.40}$$

where we define the overlap matrix as

$$A_{ki} = \sum_\ell f_{k\ell}^* g_{i\ell}. \tag{5.41}$$

Using Eqs. (5.36) and (5.41), it is straightforward to obtain the corresponding commutation relation

$$[\hat{b}_j, \hat{d}_k^\dagger] = A_{jk}. \tag{5.42}$$

This commutation relation allows us to calculate overlaps for arbitrary number of modes M and number of bosons N. For $N = 2$, it can be shown that

$$\begin{aligned} \langle n|m\rangle &= \frac{1}{\mathcal{N}}\langle \mathrm{vac}|\hat{b}_i\hat{b}_j\hat{d}_k^\dagger\hat{d}_\ell^\dagger|\mathrm{vac}\rangle \\ &= \frac{1}{\mathcal{N}}\left(A_{ik}A_{j\ell} + A_{jk}A_{i\ell}\right), \end{aligned} \tag{5.43}$$

where $\mathcal{N} = \sqrt{n_i!n_j!m_k!m_\ell!}$. For $N = 3$, the associated overlap is

$$\begin{aligned} \langle n|m\rangle &= \frac{1}{\mathcal{N}}\langle \mathrm{vac}|\hat{b}_i\hat{b}_j\hat{b}_s\hat{d}_t^\dagger\hat{d}_k^\dagger\hat{d}_\ell^\dagger|\mathrm{vac}\rangle \\ &= \frac{1}{\mathcal{N}}[A_{it}(A_{jk}A_{s\ell} + A_{sk}A_{j\ell}) \\ &+ A_{jt}(A_{ik}A_{s\ell} + A_{sk}A_{i\ell}) + A_{st}(A_{ik}A_{j\ell} + A_{jk}A_{i\ell})], \end{aligned} \tag{5.44}$$

where now $\mathcal{N} = \sqrt{n_i!n_j!n_s!m_t!m_k!m_\ell!}$.

As an example, let us use the ground-state wave functions at the largest value of V_3 in Fig. 5.8 as the initial state $|\Psi_0\rangle$. For $N = 2$, the fidelity of this initial state with the symmetric superpositions at the avoided crossing $|\Psi_R\rangle$ is $\mathcal{F} = 0.9439$. While for $N = 3$, the corresponding fidelity is $\mathcal{F} = 0.9306$. These numbers suggest that this procedure is viable and the subsequent coherent oscillations will be dominated by the two lowest few-body energy states.

5.4.5 Dynamics for $N = 2$

We now proceed to a numerical demonstration of the time evolution of relevant observables for $N = 2$ following a trap quench from the ground state of the largest V_3 considered in Fig. 5.8 to the position of the avoided level crossing. The ensuing dynamics is expected to exhibit coherent oscillations with a period associated to the numerically obtained few-body energy splitting ΔE because of the large fidelity ($\mathcal{F} = 0.9439$) between the initial state and the symmetric superposition of

the two lowest energy states at the resonance. Indeed, we observe in Fig. 5.11 that both Bose-Hubbard and MCTDHB results exhibit oscillatory behavior of relevant observables, which are the mode occupation number in the wide well $\langle \hat{n}_R \rangle$ for the Bose-Hubbard model and the position of the center-of-mass $\langle x \rangle / w_0$ for the MCTDHB calculation. The presence of small amplitude oscillations in the MCTDHB results can be explained by the fact that the fidelity is not perfect. Nevertheless, the oscillation frequency of the center-of-mass position is consistent with the numerically calculated ΔE for $N = 2$. The difference in oscillation frequency when compared to the Bose-Hubbard results, which is about $\sim 10\%$, can be accounted for by the slight mismatch between the energy splittings obtained from the two methods. But more importantly, the time-dependent simulations presented in Fig. 5.11 corroborate the validity of the time-independent arguments based on the avoided level crossings.

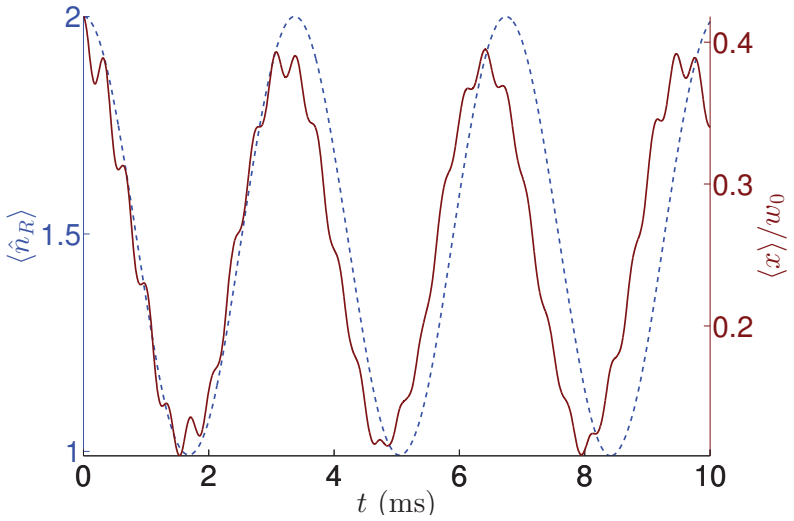

Figure 5.11: Dynamics for $N = 2$ following a quench to the position of the avoided crossing from the ground state at the largest value of V_3 in Fig. 5.8. Dashed-curve (left y-axis) denotes the dynamics of the expectation value of mode occupation number in the right (wide) well $\langle \hat{n}_R \rangle$ within the Bose-Hubbard model. Solid curve (right y-axis) depicts the dynamics of the average center-of-mass position in the axis of asymmetry $\langle x \rangle / w_0$ calculated from MCTDHB.

Finally, we compare the energy splittings for $N = 2$ and $N = 3$ with that for $N = 1$. Indeed, it can be seen from Fig. 5.12 that our numerical results for $\Delta E/2J$ closely follow the expected $\sqrt{N}$-behavior. For $N = 2$, we can directly compare our result $\Delta E/2J = 1.40$ with previous experimental observation [115], which is $\Delta E/2J = 2.37$. This clearly illustrates that our proposal of using an asymmetric double well should be able to capture the expected tunneling period in the interaction blockade regime, at least for the number of bosons presented here.

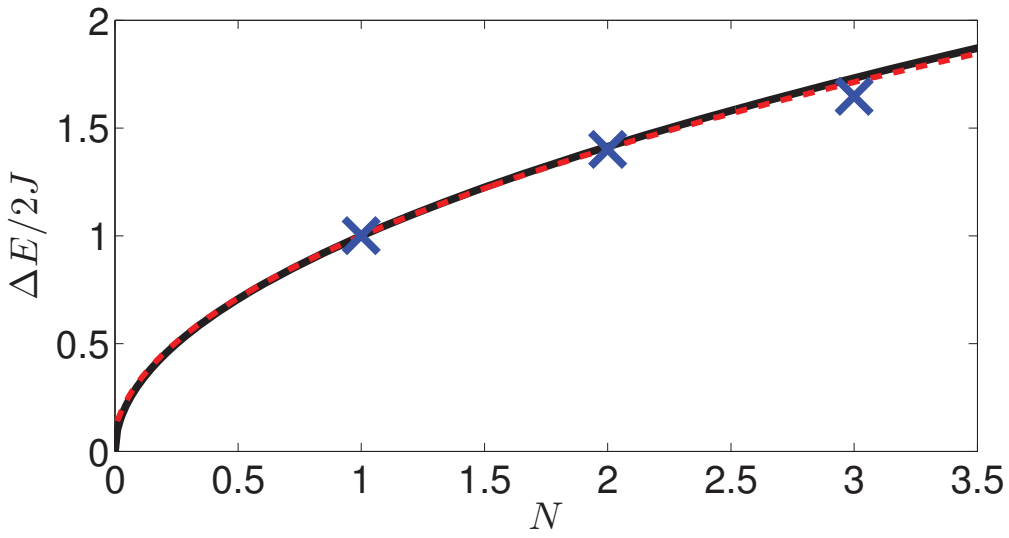

Figure 5.12: Multiple particle energy splittings as a function of N. Solid line corresponds to the expected $\sqrt{N}$ dependence. The dashed line corresponds to the first-order approximated splitting given by Eq. (5.15) for an effective Bose-Hubbard parameter of $U_L/J \approx 7$ and $U_R/J \approx 4$. Blue crosses correspond to the numerical results at the positions of resonance indicated by the circles in Figs. 5.7 and 5.8.

5.5 Discussion and Outlook

In this work, we have proposed a way to experimentally observe the $\sqrt{N}$ bosonic enhancement factor for the energy splitting in the interaction blockade regime of few

bosons. Our suggestion is to use an asymmetric double well configuration made from superimposing single-well potentials. This setup allows for tuning of energy levels by varying the depth of the well farthest away from the effective barrier. In doing so, the effect on the barrier that separates the left and the right wells becomes minimal as the avoided level crossing is being probed. To test our claim, we have done a series of numerical experiments using 3D optical tweezers and obtain the relevant energy splittings. We have shown that the $\sqrt{N}$ behavior of the energy gap between the tunneling resonance states manifests for $N = 2$ and $N = 3$. While good agreement can be seen for $N = 2$, there is already a slight deviation for the $N = 3$ results from the expected $\sqrt{N}$ prediction. Unfortunately, the correction according to Eq. (5.15) for finite U_L/J does not quantitatively capture the apparent decrease in the energy level splitting for $N = 3$ as seen in Fig. 5.12. The nature of this discrepancy can be studied in future works. In general, one might expect larger deviations for increasing N because the depth of the well farthest from the barrier needs to be tuned more in order to locate the resonance. Thus, probing the avoided level crossing for larger N might have more pronounced effects on the deformation of the effective barrier. The ideas in our proposed scheme can be extended to a system comprising of more laser beams than the three beams considered in this work. Of course, the complexity of the parameter space increases but in exchange, this consideration can improve the possibility of studying coherent transport phenomena without altering the tunneling barrier in systems with larger N.

In terms of experimental implementation, the multi-well potential of Eq. (5.27) can be realized by using for example spatial light modulator [128] or acousto-optical modulator [98,129] techniques. The avoided-level crossing for N bosons can be probed by initializing the experiment in a regime where the ground state corresponds to all the bosons occupying the right well, i.e., large values of V_3. Then, the trap depth of the right-most well is adiabatically decreased until one boson can tunnel to the left well, which first happens in the tunneling resonance. Once the avoided level crossing is identified, the next step would be to measure the period of coherent oscillations,

which can then be compared with the numerical results presented here.

It is quite interesting to point out that the ground-state single-particle energy for the states in Figs. 5.9 and 5.10 is above the classical saddle point of the external potential at $x = y = z = 0$. Thus, the coherent oscillations found in our numerical experiments can be regarded as some form of over-the-barrier tunneling dynamics. Interestingly, it was shown in Ref. [130] that a version of the Coulomb blockade phenomenon persists in the regime dominated by thermal activation of electrons over the tunnel barriers. In our case, even though the ground-state single-particle energy is above the barrier, we still observe the $\sqrt{N}$ prediction in the interaction blockade limit of the Bose-Hubbard model. This begs the question of how far above the barrier the single-particle energies can go before Eq. (5.2) breaks down. In the absence of any barrier, we can consider as an example a simple harmonic oscillator potential with equidistant energies. In this case, by virtue of symmetry in the wave function, symmetric and anti-symmetric superpositions of the ground and first-excited states will still produce localized functions. However, the conceptual equivalent of tilting the potential in this case would be a simple displacement of the harmonic trap. Therefore, the single-particle energy splitting remains unchanged and no avoided crossing appears. Perhaps more important, it becomes harder to justify in the absence of a barrier the use of only the two lowest single-particle states since the energy levels are now spaced equally. These factors suggest a breakdown of Eq. (5.2) in the complete absence of a barrier. A more systematic study of this crossover behavior as the classical barrier is decreased can be an interesting direction for future work.

Chapter 6

Quantum thermalization of ultracold bosons in a 1D double-well potential

6.1 Introduction

Motivated by experiments in ultracold atoms [6, 15], there has been a resurgence of interest to explore the fundamental aspects of statistical mechanics and whether statistical properties can emerge from unitary time evolution. To this end, recent attempts in describing thermalization in closed quantum systems focused on time-evolving observables that are local to a subsystem and how they approach thermal equilibrium described by Gibbs ensemble [16, 131]. One proposed mechanism in order to understand thermalization is the eigenstate thermalization hypothesis (ETH) [16, 38, 39].

The ETH conjectures that under certain conditions, the expectation value of a physically relevant observable will have a long-time average close to an appropriate microcanonical ensemble prediction. When testing the ETH, the system is usually driven out of equilibrium by a quantum quench in the parameters of the Hamiltonian.

The ETH was numerically tested against other hypotheses and it was shown that for initial states following the conditions of the ETH, thermalization is achieved within observables [16, 132]. To introduce basic ideas of the ETH, consider an initial state $|\phi_0\rangle$, which is not an eigenstate of some post-quench or final Hamiltonian $\hat{H}$ without any degeneracies. Then, the initial state can be expanded in terms of the eigenstates of $\hat{H}$ with eigenvalues E_k as

$$|\phi_0\rangle = \sum_k \alpha_k |k\rangle. \tag{6.1}$$

After the quench, the initial state will undergo time evolution as

$$|\phi(t)\rangle = e^{-i\hat{H}t/\hbar}|\phi_0\rangle \tag{6.2}$$

and therefore, the expectation value of an observable is given by

$$\langle\hat{\mathcal{O}}(t)\rangle = \sum_{k,l} \alpha_l^* \alpha_k e^{i(E_l - E_k)t/\hbar} \mathcal{O}_{lk} \tag{6.3}$$

with $\mathcal{O}_{lk} = \langle l|\hat{\mathcal{O}}|k\rangle$. Due to dephasing, (6.3) will relax to the infinite-time average,

$$\overline{\langle\hat{\mathcal{O}}\rangle} = \lim_{t\to\infty} \frac{1}{t} \int_0^t d\tau \langle\hat{\mathcal{O}}(\tau)\rangle = \sum_k |\alpha_k|^2 \mathcal{O}_{kk}. \tag{6.4}$$

This long-time average is commonly referred to as the diagonal ensemble prediction due to the diagonal ensemble, $\hat{\rho}_d = \sum_k |\alpha_k|^2 |k\rangle\langle k|$. According to the ETH, the diagonal ensemble average of an observable, Eq. (6.3), is close to an appropriate microcanonical average $\langle\hat{\mathcal{O}}\rangle_{\mathrm{ME}}$,

$$\begin{aligned} \langle\hat{\mathcal{O}}\rangle_{\mathrm{ME}} &= \mathcal{N}^{-1} \sum_{|E_k - E_0| < \Delta E} \mathcal{O}_{kk} \\ \overline{\langle\hat{\mathcal{O}}\rangle} &= \sum_k |\alpha_k|^2 \mathcal{O}_{kk} \\ \langle\hat{\mathcal{O}}\rangle_{\mathrm{ME}} &= \overline{\langle\hat{\mathcal{O}}\rangle} \end{aligned} \tag{6.5}$$

where $\mathcal{N}$ is the number of eigenstates within a narrow energy window ΔE around the initial mean energy of the system E_0. The last equality in Eq. (6.5) is true if

the eigenstate expectation value (EEV), $\mathcal{O}_{kk}$, is a smooth function of E_k, while the off-diagonal elements $\mathcal{O}_{kl}$ are negligible [16,39]. There is no rigorous analytical proof of the ETH but different numerical studies on spin systems and lattice models both for small and large system sizes support its validity [133–141].

Another important aspect of relaxation is the question of how local observables equilibrate. This is particularly important in the dynamics of nearly integrable systems, which may exhibit a two-stage equilibration process. Both theoretical and experimental studies have investigated the nature of the so-called prethermalized states in various physical set-ups [142–152]. These prethermalized states are quasi-stationary states where the dynamics of local operators in the system appear to be trapped for significant amount of time. However, as the name suggests, these prethermalized states are expected to eventually thermalize in the long-time limit.

The emergence of statistical relaxation can also be linked to the onset of quantum chaos as highlighted by previous studies [153–155]. In this context, particular emphasis is laid on the form of the energy distribution of an initial state and how it compares with predictions of quantum chaos. We will utilize this approach to demonstrate chaotic initial states even for energies far from the middle of the spectrum of eigenenergies, an extension of the findings in Ref. [156].

In this work, we will study the nonequilibrium dynamics of interacting bosons in a one-dimensional double-well potential, which can be modelled using a two-site multilevel Bose-Hubbard Hamiltonian [26,157]. Contrary to previous studies dealing with few atoms in multiple lattice sites, we study the other limit of having finite large number of bosons confined in few sites. As a matter of fact, it was checked that this system will thermalize due to the ergodicity of the associated mean-field trajectories in the semiclassical limit of large N [17]. Here, we will only consider $N = 35$ bosons and use exact diagonalization to access the eigenvalues and the eigenstates of the final Hamiltonian. Firstly, we determine the chaoticity of the post-quench Hamiltonian on the basis of spectral statistics. We will then verify the validity of the ETH in this system. Our results based on the distribution of EEV illustrate that not all

eigenstates are thermal. Using all possible initial product state configurations, we will compare the expectation values of local operators obtained using the diagonal and the microcanonical ensemble.

Most of the studies related to subsystem thermalization involve spatial partitioning of the system [137, 158–160]. Instead, we implement a different partitioning scheme where a subsystem will only consist of one mode, either the lower or the upper level in one of the wells. Since thermalization is a dynamical process, we will also compute the time evolution of local operators and the von Neumann entropy of a subsystem. We find that the relaxation dynamics of the von Neumann entropy is instructive in revealing prethermalization in the system. Moreover, we observe that fast relaxation of a local operator correlates with a rapid single-step growth of the von Neumann entropy as it approaches the Gibbs entropy. On the other hand, we observe a two stage relaxation process for initial states close to the middle of the spectrum. Finally, we discuss possible mechanism for the prethermalization in the system and the associated timescales.

This chapter is organized as follows. In Sec. 6.2, we first describe the model and the quench protocol used in this work. Sec. 6.3 contains results that characterize the spectrum and the chaoticity of the post-quench Hamiltonian. We investigate the requirements of the ETH in Sec. 6.4. The key results on relaxation and thermalization in the system are discussed in Sec. 6.5. In Sec 6.5.1, we compare the long-time and microcanonical averages of local operators. The presence of chaotic initial states across the spectrum is discussed in Sec. 6.5.2. Results for the actual time evolution of local properties in the system are presented in Sec 6.5.3 and Sec. 6.5.4. In Sec. 6.6, we discuss the relaxation timescales and the process of prethermalization in the system. Finally, we briefly summarize our findings in Sec. 6.7.

6.2 Model and Quench Dynamics

We study thermalization in a finite isolated quantum system with bosons trapped in a double-well potential shown in Fig. 6.1. A single boson can occupy four modes (two single-particle levels in each well), which can be described by the following two-level generalization of the Bose-Hubbard model [26, 157]:

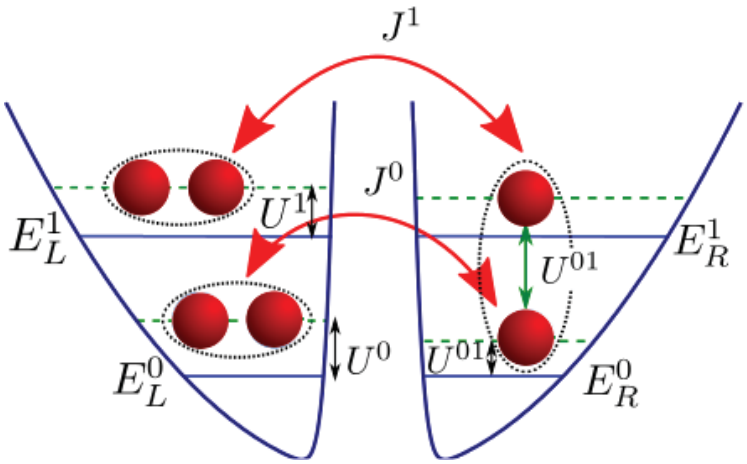

Figure 6.1: Schematic of the double-well potential with two energy levels. The inter-level coupling U^{01} adds another degree of freedom in the system, which is expected to break integrability.

$$\hat{H} = -\sum_{r\neq r',\ell} J^{\ell}\hat{b}_r^{\ell\dagger}\hat{b}_{r'}^{\ell} + \sum_{r,l} U^{\ell}\hat{n}_r^{\ell}(\hat{n}_r^{\ell}-1) + \sum_{r,\ell} E_r^{\ell}\hat{n}_r^{\ell} + U^{01}\sum_{r,\ell\neq\ell'}(2\hat{n}_r^{\ell}\hat{n}_r^{\ell'} + \hat{b}_r^{\ell\dagger}\hat{b}_r^{\ell\dagger}\hat{b}_r^{\ell'}\hat{b}_r^{\ell'}), \tag{6.6}$$

where $\hat{b}_r^{\ell\dagger}$ and $\hat{b}_r^{\ell}$ are the bosonic creation and annihilation operators of an atom in well r and energy level ℓ, respectively. The Hamiltonian in Eq. (6.6) can be derived from its second-quantized form after a tight-binding approximation [26]. The system is effectively mapped into a two-site lattice model with added "dimensionality" or degree-of-freedom due to the coupling with the first excited single particle level.

We consider an external harmonic potential with oscillator frequency ω_0, which is splitted by a focused laser beam located at the center of the trap and described by a Gaussian potential $V_0\exp(-x^2/2\sigma^2)$. The parameters in Eq. (6.6) can be easily evaluated for a specific realization of the double-well potential described by the single particle Hamiltonian [26],

$$\hat{H}_{\rm sp} = \frac{-\hbar^2}{2m}\frac{\partial^2}{\partial x^2} + \frac{m\omega^2 x^2}{2} + V_0\exp\left(-\frac{x^2}{2\sigma^2}\right). \tag{6.7}$$

The localized functions ϕ_r^ℓ in level $\ell \in \{0,1\}$ and site $r \in \{L,R\}$ are obtained by symmetric and antisymmetric superpositions of the eigenstates of the single particle Hamiltonian in Eq. (6.7). The corresponding eigenvalues are $E_r^\ell = \int dx \phi_r^{\ell *}(x)\hat{H}_{\rm sp}\phi_r^\ell(x)$. The tunnelling terms between wells are $J^\ell = -\int dx \phi_L^{\ell *}(x)\hat{H}_{\rm sp}\phi_R^\ell(x)$. The interaction terms between atoms in the same well and the same energy level are $U^\ell = g\int dx|\phi_r^\ell|^4$. There is also an interlevel coupling corresponding to the two-atom hopping term between energy levels in the same well given by $U^{01} = g\int dx(\phi_r^{0*}(x))^2(\phi_r^1(x))^2$. The limit of $U^{01} = 0$ is the integrable Bose-Hubbard dimer model for a double-well, which was extensively studied before in different contexts [121–124, 161, 162]. Integrability of the dimer can be broken by adding one or more degrees of freedom without changing the number of conserved quantities, which for the dimer model corresponds to the energy and the number of bosons [163, 164]. A finite value of U^{01} introduces additional degrees of freedom and thus breaks the integrability of the system. Note that upon choosing the trap parameters, the only free parameter in the system is the coupling constant g, which affects both U^ℓ and U^{01}. This is a subtle detail that we need to keep in mind as blindly increasing the interaction g (in hopes of increasing the integrability breaking term U^{01}) will actually push the system towards a strongly interacting regime dominated by quasidegeneracies [26].

We now discuss the quench protocol used in our study of the nonequilibrium dynamics in the system. We consider a partitioning of the system such that each mode is considered as a subsystem and the remaining three modes will act as an environment. Initially, the number of bosons in each mode is fixed, i.e. the tunnelling and the interlevel terms are set to zero, such that the system starts as a product

state of eigenstates of each subsystem. In particular, we choose a set of initial states corresponding to all possible Fock state configurations $|n\rangle = |n_0\rangle = |n_L^0, n_R^0, n_L^1, n_R^1\rangle$. The eigenstates $|k\rangle$ of the post-quench Hamiltonian $\hat{H}$ with eigenvalues E_k can be expressed in terms of the Fock basis

$$|k\rangle = \sum_n C_n^k |n\rangle. \tag{6.8}$$

This expansion is similar to how the mean-field or unperturbed (in our case uncoupled) basis is physically motivated in studies related to chaotic eigenstates and its connection to thermalization of isolated systems [153].

We do a sudden quench by turning on the tunnelling and the interlevel coefficients. The wavefunction unitarily evolves in time according to

$$|\psi(t)\rangle = e^{-i\hat{H}t/\hbar}|n_0\rangle = \sum_k C_{n_0}^{k*} e^{-iE_k t/\hbar}|k\rangle. \tag{6.9}$$

For brevity, we refer to the mean energy, which is conserved during the dynamics,

$$E_0 = \langle n_0|\hat{H}|n_0\rangle = \sum_k E_k |C_{n_0}^k|^2 \tag{6.10}$$

as simply the initial energy of the system.

For the post-quench Hamiltonian, the barrier height is chosen to be $V_0 = 5\hbar\omega_0$ with width $\sigma = 0.1 l_{ho}$, where the harmonic oscillator length is $l_{ho} = \sqrt{\hbar/m\omega_0}$. The interaction coupling g is chosen such that $NU^0/\hbar\omega_0 = \text{const}$. For this parameter space of the trap, the coefficients in the Hamiltonian are $J^0/\hbar\omega_0 = 0.26$, $J^1/\hbar\omega_0 = 0.34$, $E_r^0/\hbar\omega_0 = 1.25$, $E_r^1/\hbar\omega_0 = 3.17$, $NU^0/\hbar\omega_0 = \text{const.}$, $U^1 = 3U^0/4$, and $U^{01} = U^0/2$.

We use exact diagonalization to obtain the eigenvalues and the eigenvectors expressed in the Fock basis. To this end, we obtain the $D \times D$ Hamiltonian matrix in the Fock basis where the size of the Hilbert space is $D = (N+3)!/(N!)(3!) = 8436$. Alternatively, the time evolution of the wave function can be calculated from the time evolving expansion coefficients,

$$|\psi(t)\rangle = \sum_{\{n\}} c_n(t)|n\rangle \tag{6.11}$$

where $|n\rangle$ spans all possible Fock state configurations of the system. Temporal evolution of the expansion coefficients is computed using standard numerical integrator, e.g. seventh/eighth order Runge-Kutta method.

6.3 Ratio of Consecutive Level Spacings Distribution

An interesting question for finite quantum systems is the relevance of chaoticity of the Hamiltonian in the study of thermalization [156]. It was conjectured using a system of one-dimensional lattice with spin-1/2, that the occurrence of thermalization depends only on the level of delocalization of initial states [156]. Furthermore, this condition has been shown to be sufficient for initial states close to the middle of the spectrum irrespective of integrability (or chaoticity) in both pre-quench and post-quench Hamiltonian.

The level statistics of a chaotic Hamiltonian was found to possess similar spectral properties as random matrices [34, 165]. One common measure of level statistics is the level spacing distribution, $s_k = E_{k+1} - E_k$, where $\{E_k\}$ is the set of eigenenergies in ascending order [165]. In a Hamiltonian with time-reversal symmetry, the chaotic regime is identified by a level spacing distribution similar to the Gaussian orthogonal ensemble (GOE) [165]. The connection between nonintegrability and a GOE-like spectral behavior was pointed out in various works such as Refs. [155, 166–168] On the other hand, integrable models are expected to have a Poissonian level spacing distribution as demonstrated in Refs. [33, 155, 167, 168].

Due to the large interaction strengths involved in our quench dynamics, i.e. $NU^\ell/J^\ell > 1$ for both levels ℓ, it is convenient to avoid any unfolding procedure of the spectrum [167]. Note that the main objective of unfolding the spectrum is to ensure the mean level density of a new set of energies is unity. This is done to compare different systems on equal footing, i.e., varying interaction strength. Instead, we obtain the distribution of the ratio of consecutive gaps between adjacent levels,

$r_k = \min(s_k, s_{k-1})/\max(s_k, s_{k-1}) = \min(\frac{s_k}{s_{k-1}}, \frac{s_{k-1}}{s_k})$ [36, 37, 167]. We compare the numerically obtained distribution $P(r)$ with the analytical expressions for the Poisson and the GOE distributions [37]

$$P_{\rm P}(r) = \frac{2}{(1+r)^2}, \;\; P_{\rm GOE}(r) = \frac{27}{4}\frac{r+r^2}{(1+r+r^2)^{5/2}}. \tag{6.12}$$

A more quantitative comparison can be made using the mean value of r denoted as $\langle r \rangle$, which is $\langle r \rangle_{\rm P} = 2\ln 2 - 1 \approx 0.3863$ for the Poisson distribution and $\langle r \rangle_{\rm GOE} \approx 0.5359$ for the GOE [37].

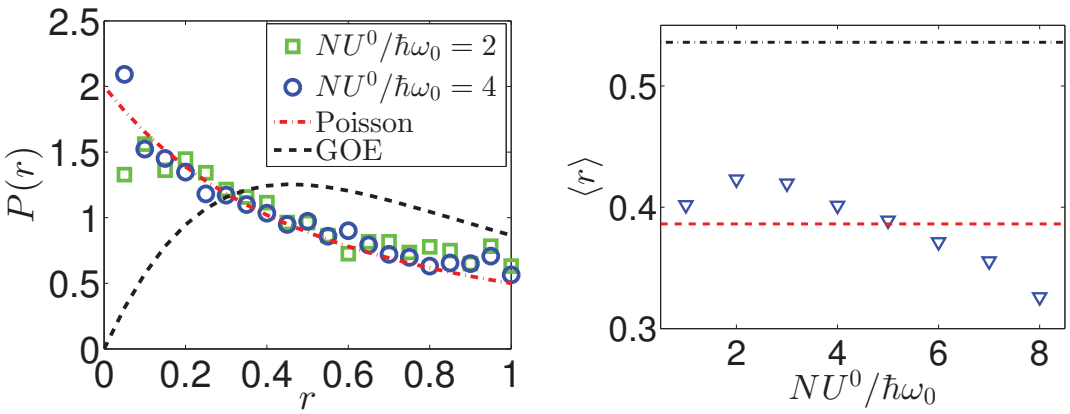

Figure 6.2: (Left) Distribution of the ratio of adjacent level spacings r (Right) Mean value $\langle r \rangle$ as a function of the interaction parameter. The GOE (dashed-dotted) and the Poissonian (dashed) averages are also shown.

There is parity or reflection symmetry about the center of the double-well system. In order to avoid mixing eigenenergies from different symmetry sector, we separate the eigenenergies according to its parity, i.e. even or odd eigenvectors in the Fock basis. We do this by constructing eigenstates with well-defined parity in Fock space [169]. For the analysis of spectral statistics presented in this section, we numerically diagonalize the Hamiltonian in the well-defined parity basis. We denote the reflection operator, which exchanges the Fock state from left to right or vice versa

as $\hat{\mathcal{P}}|n_L^0, n_R^0, n_L^1, n_R^1\rangle = |n_R^0, n_L^0, n_R^1, n_L^1\rangle$. Then, we use a set of basis states given by:

$$|\widetilde{n}\rangle_{\pm} = \frac{1}{\sqrt{2}}\Big(|n\rangle \pm \hat{\mathcal{P}}|n\rangle\Big). \tag{6.13}$$

The distribution of the ratio of adjacent energy gaps $P(r)$ for the even parity sector is illustrated in Fig. 6.2. First, we analyze the spectral statistics of the full spectrum. Notice how $\langle r\rangle$ increases with the interaction strength before reaching its maximum around $NU^0/\hbar\omega_0 = 2$. It then decreases as you further increase the interaction strength. Perhaps more interesting, the mean value of r becomes smaller than the Poisson distribution $\langle r\rangle_{\mathrm{P}}$ for $NU^0/\hbar\omega_0 > 5$. This level "clustering" can be explained by the appearance of quasi-degenerate eigenvectors (in each symmetry sector) when the interaction terms U^ℓ become sufficiently larger than the tunnelling terms J^ℓ [26]. Specifically, these quasi-degenerate pairs appear as high-lying excited states of the system. Nevertheless, our results for the distribution of the ratio of consecutive level gaps imply that the post-quench Hamiltonian is non-chaotic in the chosen parameter space of the trap. Even though the final Hamiltonian is nonintegrable, the spectral statistics of the final Hamiltonian is actually closer to the Poisson distribution than the GOE for the interaction strengths considered here. This indicates that the system is still close to an integrable point after the quench.

In the following section, we demonstrate that thermalization is still viable, in the context of the ETH, for the non-chaotic Hamiltonian considered here. We will also argue later on that the presence of quasi-degeneracies in the spectrum has important implications to the process of relaxation in the system.

6.4 Eigenstate Thermalization Hypothesis

The microcanonical ensemble can describe the long-time averages if the requirements of the ETH are satisfied. Specifically, the diagonal ensemble prediction for a local operator $\overline{\langle \hat{A}\rangle}$ will be close to a value predicted by a thermal or microcanonical ensemble if the EEV is a smooth function of E_k. This requirement is fulfilled if the vertical

width of the EEV at a chosen energy is small [137]. We now calculate the eigenstate expectation values of the mode occupation number, $\langle k|\hat{n}_r^\ell|k\rangle$, and check how they are distributed in the eigenenergies of the system for different interaction strengths.

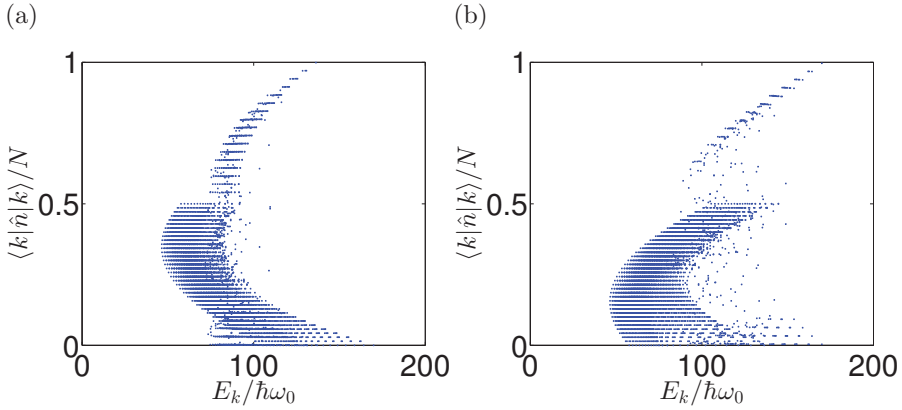

Figure 6.3: Distributions of EEV for $NU^0/\hbar\omega_0 = 4$ but $U^{01} = 0$. (a) $\hat{n}_L^0$ (b) $\hat{n}_L^1$.

First, we consider the integrable limit of uncoupled Bose-Hubbard dimers when the interlevel coupling is absent, $U^{01} = 0$. We plot in Fig. 6.3(a) the EEV of the dimer with the lower on-site energy while Fig. 6.3(b) shows the EEV of the dimer with higher on-site energy. The overall structure of the distribution of EEV appears similar in both dimers. That is, the expectation values of the mode occupation seemingly appear separated in flat bands, which then prohibits the EEV from being a smooth function of the energy. Physically, this is a direct consequence of $NU^\ell/J^\ell \gg 1$. There is large range of possible EEV at a given energy E_k and hence thermalization must be absent in this limit.

We plot the distribution of EEV for different interaction strengths $NU^0/\hbar\omega_0$ and finite integrability breaking $U^{01} = U^0/2$ in Fig. 6.4. For $NU^0/\hbar\omega_0 = 2$, the distribution of EEV is still regular and structured similar to the integrable case. Even though the EEV starts to clump together, separated bands are still noticeable specially in low energies. The behavior of the distribution of EEV, in particular its smoothness, improves as the interaction strength is increased from $NU^0/\hbar\omega_0 = 2$ to $NU^0/\hbar\omega_0 = 3$. For $NU^0/\hbar\omega_0 = 4$, the vertical width of the distribution of EEV in the lower half of

the spectrum is narrower than that in the remaining half. Note, however, that eigenstates that are very close to the ground state energy will always violate the ETH, at least for interactions considered here, since the distribution is quite sparse in this region. This implies the absence of thermalization for initial energies close to the ground state. We point out that relaxation close to an infinite temperature state can be considered as a borderline case for which the ETH is still satisfied as seen from the solid vertical line in Fig. 6.4(e)-(f).

A more quantitative description of the smoothness of the EEV can be drawn from the distribution of gaps between consecutive EEV [139],

$$|\lambda_k| = \Big|\langle k+1|\hat{O}|k+1\rangle - \langle k|\hat{O}|k\rangle\Big|. \tag{6.14}$$

If EEV is a smooth function of the eigenenergies, the distribution of $|\lambda_k|$ denoted by $P(|\lambda_k|)$ will be sharply peaked near $|\lambda_k| = 0$. Accordingly, the width of $P(|\lambda_k|)$ decreases as the distribution of EEV smoothens. It is clear from Fig. 6.4 that the ETH works only for the bulk of the spectrum, i.e. in the lower half of the spectrum. Similar to Ref. [139], we consider only a part of the full spectrum by removing the lowest 10% and the highest 25% of the eigenstates. This choice is motivated by the general features of the distributions of EEV shown in Fig. 6.4 wherein strong fluctuations are seen for high energies which justifies the removal of the upper 25% of the spectrum for the subsequent analysis. Moreover, we are not interested in initial states with energies somewhere in the edges of the spectrum since random matrix theory is not expected to work in those regions [32]. More importantly, our main goal is to study thermalization dynamics and from the results shown in Fig. 6.4, we can narrow down our search for relevant initial states by looking at only the central region of the energy spectrum where the distributions of EEV start to smoothen. In Fig. 6.5, we plot $P(|\lambda_k|)$ for the rescaled occupation number in the lower mode of the left well $\hat{n}_L^0/\sqrt{N}$. As we decrease the interaction strength, the distribution of $|\lambda_k|$ broadens and the peak increases. This is consistent with the qualitative picture presented in Fig. 6.4.

Our results in this section suggest that despite the final Hamiltonian being near

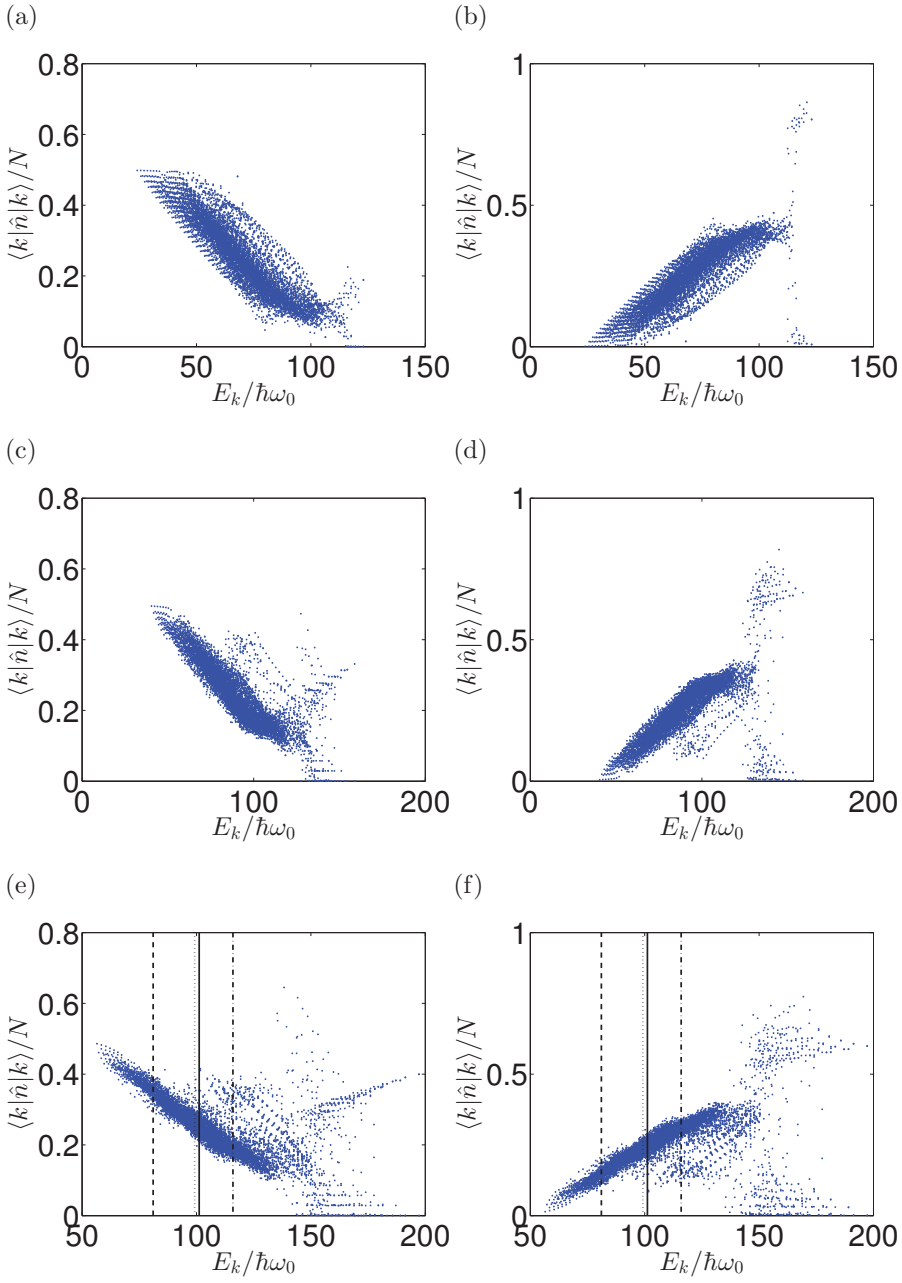

Figure 6.4: Distributions of EEV of $\hat{n}_L^0$ (left) and $\hat{n}_L^1$ (right) for (a)-(b) $NU^0/\hbar\omega_0 = 2$, (c)-(d)$NU^0/\hbar\omega_0 = 3$, and (e)-(f) $NU^0/\hbar\omega_0 = 4$. Vertical lines mark the mean energies of initial states for the dynamics in the subsequent sections: (dashed) $E_0/\hbar\omega_0 = 81.053$, (dotted) $E_0/\hbar\omega_0 = 99.202$, (solid) $E_0/\hbar\omega_0 = 101.181$, and (dashed-dotted) $E_0/\hbar\omega_0 = 115.9409$

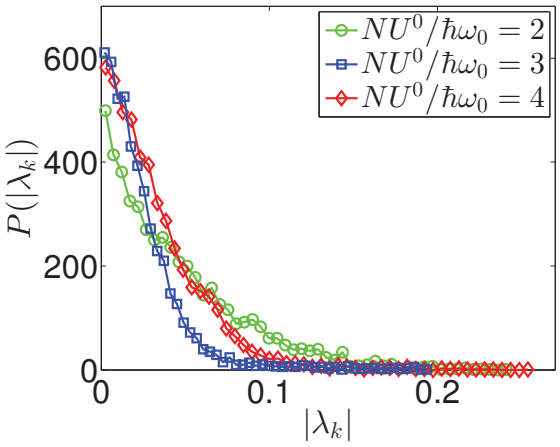

Figure 6.5: Distributions of consecutive EEV gaps of $\hat{n}_L^0$ for different interaction strengths.

integrability, the fact that it is still nonintegrable permits the fulfilment of the ETH but not for all eigenstates. Therefore, the condition for an initial state to properly thermalize will largely depend on which part of the spectrum the energy of an initial state is located. This is indeed the case, as we shall see later.

6.5 Quench Dynamics

6.5.1 Comparison of Diagonal to Microcanonical Expectation Values

We are interested in the relaxation dynamics if the system starts out as a product state of each mode. At long times, local operators in the system are expected to fluctuate around the mean value predicted by the diagonal ensemble

$$\overline{\langle \hat{A} \rangle} = \sum_k |C_{n_0}^k|^2 A_{kk} \tag{6.15}$$

where $A_{kk} = \langle k|\hat{A}|k\rangle$. Clearly, the diagonal ensemble will depend on the initial state through $|C_{n_0}^k|^2$. On the other hand, the microcanonical average depends only on the initial energy and for finite system will also be a function of the energy window

ΔE. The energy window is chosen such that it is small enough to approximate the mean energy of the system but still large enough to contain significant number of eigenstates. The appropriate microcanonical prediction of a local operator is obtained by averaging over all eigenstates within a small window of energy $[E_0 - \Delta E, E_0 + \Delta E]$

$$\langle A \rangle_{\mathrm{ME}} = \frac{1}{\mathcal{N}_{E,\Delta E}} \sum_{|E_k - E_0| < \Delta E} A_{kk} \tag{6.16}$$

where $E_0 = \langle n_0 | \hat{H} | n_0 \rangle$ is the initial energy of the system and $\mathcal{N}_{E,\Delta E}$ corresponds to the number of eigenstates within the chosen window.

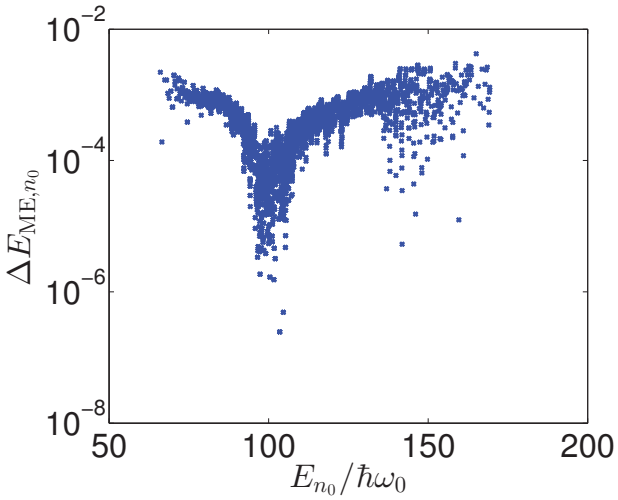

Figure 6.6: Relative deviations between the microcanonical and the mean energy of all possible initial Fock states for $NU^0/\hbar\omega_0 = 4$.

Normally, for every initial state, one will have to first calculate $\langle \hat{H} \rangle_{\mathrm{ME}} = E_{\mathrm{ME}}$ over a range of ΔE and then choose ΔE that best approximates E_0. For computational efficiency, we simply fix the energy window by choosing $\Delta E = 0.02 E_0$. Although we checked that the microcanonical averages obtained this way are still weakly dependent on other choices of ΔE. To keep track of how close the microcanonical energy is to the energy of the system, we define the relative deviation

$$\Delta E_{\mathrm{ME},n_0} = \frac{|E_0 - E_{\mathrm{ME}}|}{E_0}. \tag{6.17}$$

The plot presented in Fig. 6.6, which shows the relative deviations of microcanonical averages in the case $NU^0/\hbar\omega_0 = 4$, underpins our choice of ΔE.

The post-quench Hamiltonian Eq. (6.6) has parity or reflection symmetry about the center of the trap and so, a thermalized state is expected to respect this symmetry. That is, the stationary properties in the left well must be the same to those in the right well. This is indeed the case for both the microcanonical and the diagonal ensemble predictions shown in Figs. 6.7 and 6.8. In each plots, both ensemble averages in the left well are sitting on top of the corresponding values in the right well.

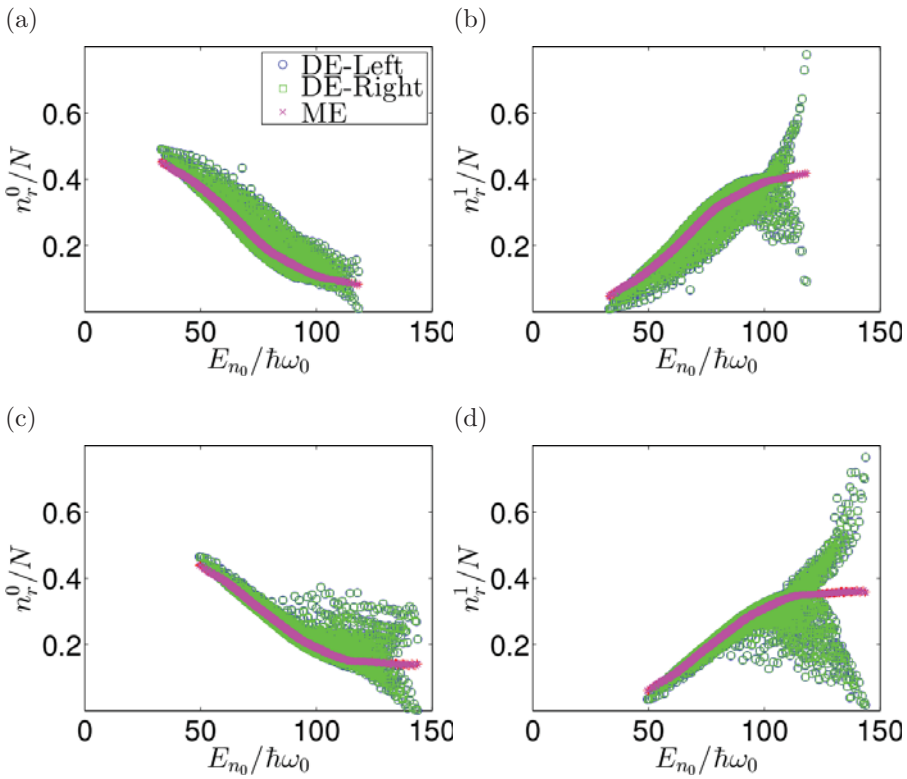

Figure 6.7: Diagonal Ensemble (DE) vs Microcanonical Ensemble (ME) averages of local operators for all possible initial Fock states. (a) $\hat{n}_r^0$ for $NU^0/\hbar\omega_0 = 2$; (b) $\hat{n}_r^1$ for $NU^0/\hbar\omega_0 = 2$; (c) $\hat{n}_r^0$ for $NU^0/\hbar\omega_0 = 3$; and (d) $\hat{n}_r^1$ for $NU^0/\hbar\omega_0 = 3$.

In Fig. 6.7 and Fig. 6.8, we compare the microcanonical and the diagonal ensemble values calculated using Eq. (6.15) and Eq. (6.16), respectively, for all initial Fock state

configurations. Similar to the distribution of the EEV, thermalization is only viable if the distribution of the diagonal ensemble averages is smooth and monotonous across the range of possible initial energies. This is an alternative way of describing another

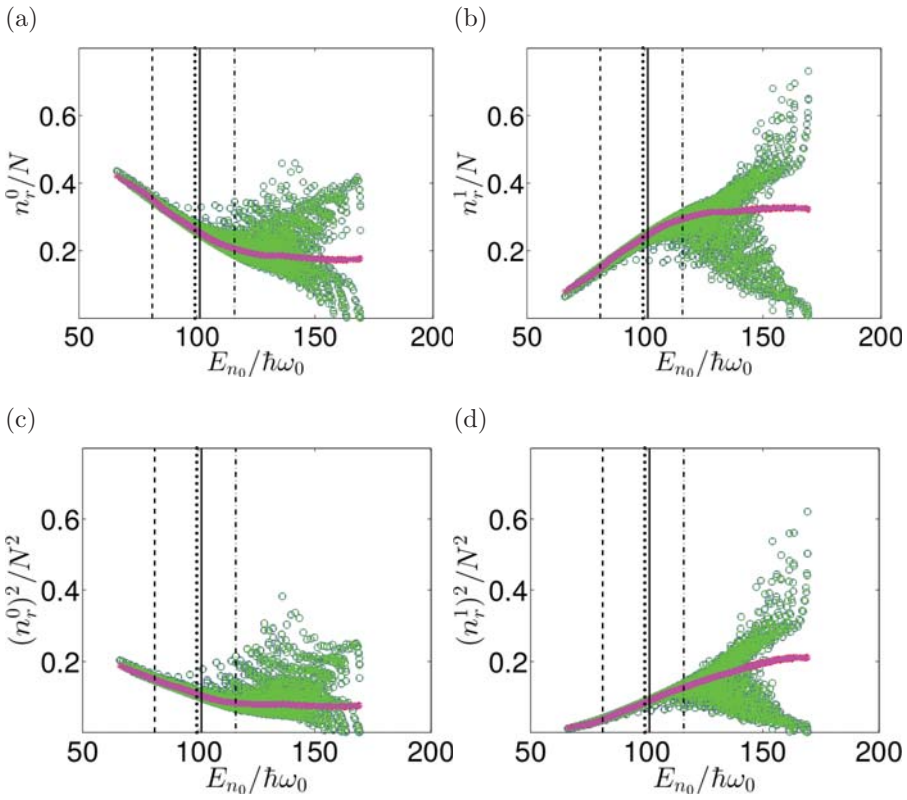

Figure 6.8: Similar to Fig. 6.7 but $NU^0/\hbar\omega_0 = 4$. (a) $\langle\hat{n}_r^0\rangle$. (b) $\langle\hat{n}_r^1\rangle$. (c) $\langle(\hat{n}_r^0)^2\rangle$. (d) $\langle(\hat{n}_r^1)^2\rangle$. Vertical lines mark the energies similar to Fig. 6.4.

signature of thermalization, which is the independence of the equilibrium state on the details of initial states. The results shown in Fig. 6.7 and Fig. 6.8 are consistent with the prediction of thermalization in the context of the ETH as discussed in Sec. 6.4. That is, the microcanonical ensemble works well in predicting the long-time average of an initial state with energy somewhere in the smooth region of the EEV distribution. Recall that in Fig. 6.4(a)-(b), the vertical width of the EEV is large for $NU^0/\hbar\omega_0 = 2$. This explains why the microcanonical averages are drastically different from the diagonal ensemble values for most of the initial states shown in

Fig. 6.7(a)-(b). Following the same line of reasoning, we find improvements in the behavior of the diagonal ensemble and its agreement with the microcanonical average when the interaction strength is increased to $NU^0/\hbar\omega_0 = 3$ and $NU^0/\hbar\omega_0 = 4$. These are shown in Fig. 6.7(c)-(d)and Fig. 6.8(a)-(b). We stress that there is a discrepancy found between the microcanonical and the long-time predictions for initial states with sufficiently low energies, in agreement with observations drawn from the EEV near the ground state.

Aside from the local one-body operator $\hat{n}_r^\ell$, we also calculate the ensemble averages for the local two-body operator $\langle(\hat{n}_r^\ell)^2\rangle$. We plot the results in Fig 6.8(c)-(d). This quantity is essential in calculating the average energy of a mode, which will be further investigated in Sec. 6.5.4.

6.5.2 Delocalized Initial States

In the spirit of the energy shell approach, consider a set of unperturbed basis states $|n\rangle$. When a finite interaction is turned on, this perturbation will couple some of these states $|n\rangle$. The exact eigenstates of the final Hamiltonian can be expressed as superpositions of the unperturbed states $|k\rangle = \sum_n C_n^k |n\rangle$. It was conjectured that the overlap coefficients C_n^k become random variables from a Gaussian distribution defined by the "energy shell" [170, 171]. For systems with only two-body interaction and sufficiently strong perturbations, regardless of integrability, the shape of the energy shell follows a Gaussian profile centered at the initial mean energy and its width is equal to the energy variance [154]. A statistical description of the system is viable if the shape of the local density of states (LDoS) or strength function resembles a Gaussian of the same mean and variance as the energy shell [155]. Recently, it was conjectured that for initial states in the middle of the spectrum, thermalization is guaranteed if the initial state ergodically fills the area defined by the energy shell, irrespective of integrability (or chaoticity) of the final Hamiltonian [156]. These initial states are referred to as chaotic, which can be viewed as delocalization of the initial unperturbed state with respect to the eigenstates of the final Hamiltonian. Although,

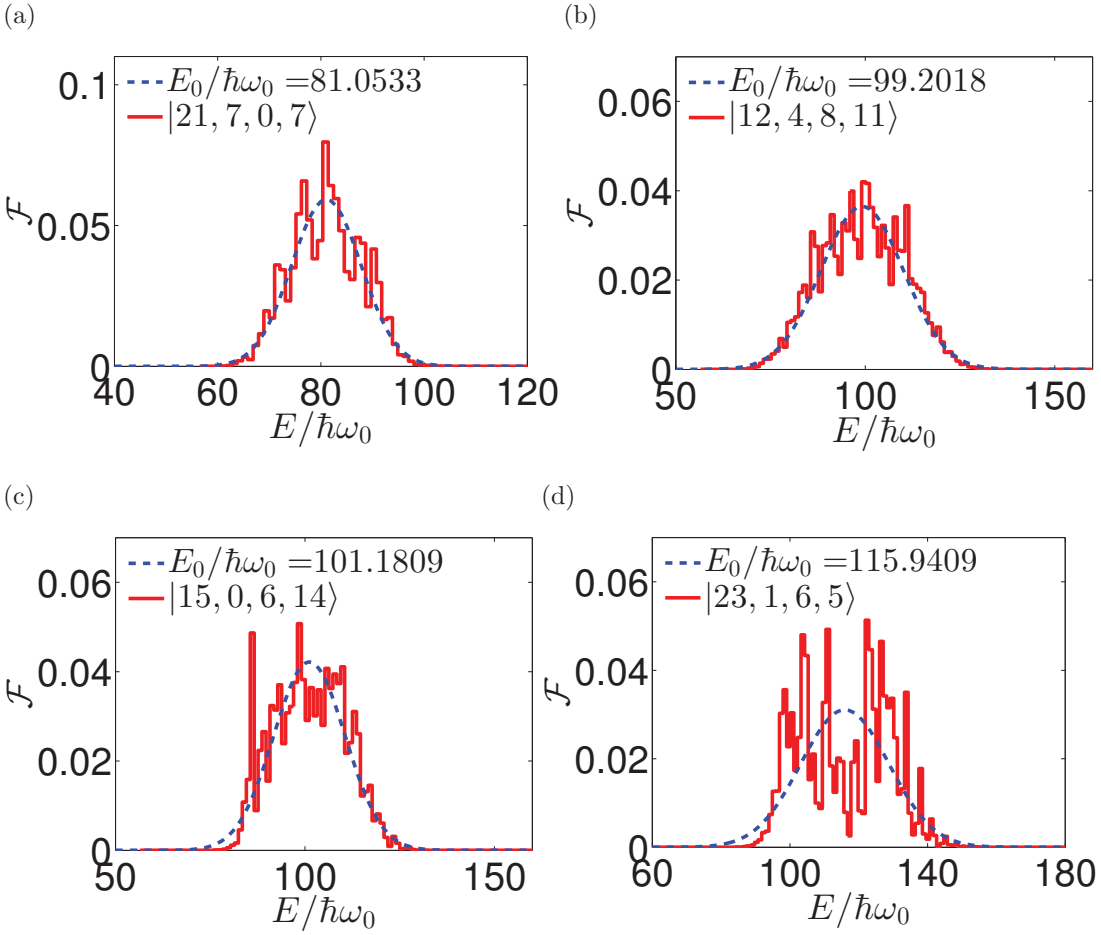

Figure 6.9: LDoS of different initial states for $NU^0/\hbar\omega_0 = 4$. The dashed lines correspond to the energy shell.

it was left as a question whether this phenomenon can occur for other models and more importantly for initial states not too close to the center of the spectrum [156]. Here, we respond to this query by demonstrating delocalization of initial states with energy away from the middle of the spectrum even though our post-quench Hamiltonian is far from having a chaotic spectrum.

The LDoS or energy distribution is defined by the distribution of $|C^k_{n_0}|^2$ in the

eigenvalues E_k

$$\mathcal{F}_{n_0}(E) = \sum_k |C^k_{n_0}|^2 \delta(E - E_k). \tag{6.18}$$

In practice, the LDoS is numerically obtained by dividing the whole spectrum of the final Hamiltonian then taking $\sum_k |C^k_{n_0}|^2$ in each bin [172]. In the limit of strong perturbation, the shape of the LDoS for finite closed system with two-body interactions follows a Gaussian distribution defined by the energy shell centered at E_0 and width $\sigma = \sqrt{\sum_k |C^k_{n_0}|^2 (E_k - E_0)^2}$ (see Refs. [173–175], and references therein),

$$\mathcal{F}_G(E) = \frac{1}{\sqrt{2\pi\sigma^2}} \exp\left[-\frac{(E - E_0)^2}{2\sigma^2}\right]. \tag{6.19}$$

We now investigate delocalization of initial states in the eigenstates of the final Hamiltonian and check if it coincides with the onset of thermalization found in the previous sections. We focus on the case $NU^0/\hbar\omega_0 = 4$ in which the distribution of the EEV has the most narrow support and thus is expected to most likely exhibit thermalization dynamics. In Fig. 6.4 and Fig. 6.8, we find smooth and monotonic behavior of the EEV and diagonal ensemble average in the lower half of the spectrum while the remaining half suffer from strong fluctuations. Following this observation, we choose four different initial energies $E_0/\hbar\omega_0 = \{81.05, 99.20, 101.18, 115.94\}$. Specifically, we choose representative initial Fock states with the aforementioned set of energies indicated by the vertical lines in Fig. 6.4 and also in Fig. 6.8.

We use 140 bins in the numerical calculation of LDoS shown in Fig. 6.9. We determine whether the initial state is chaotic with respect to the exact eigenstates by checking if the shape of its LDoS is close to the shape of the energy shell. In Fig. 6.9(a)-(c), we confirm the existence of chaotic initial states in the system by showing that for these initial states, most areas defined by the energy shell are nicely filled. More importantly, these delocalized initial states display thermal behavior as shown in Fig. 6.8. Due to the system being finite, strong fluctuations around the mean energy is visible. Nevertheless, the behavior in the tails of the energy distribution is still quite close to the Gaussian tail of the energy shell. This is consistent with observations in other finite systems such as those found in Ref. [176].

Also shown in Fig. 6.9(d) is an initial state close to the middle but already in the upper half of the spectrum, $E_0/\hbar\omega_0 = 115.94$. Clearly, this state no longer has a Gaussian profile and its LDoS exhibits multiple peaks. It is possible that the energy distribution of this state can be described by a bimodal Lorentzian distribution similar to the one in Ref. [172] but a more careful numerical analysis is needed. Note that this particular case, $E_0/\hbar\omega_0 = 115.94$, reflects the failure of the ETH in the system since the distribution of the EEV for this choice of energy is quite broad as seen in Fig. 6.4. Moreover, there are significantly stronger fluctuations in the diagonal ensemble averages of initial states around this energy as depicted in Fig. 6.8. Thus, this initial state is not expected to thermalize.

6.5.3 Relaxation of Mode Occupation Number

Our observable of interest that is local to a subsystem is the occupation number of a mode $\hat{n}_r^\ell$. In this section, we study the relaxation dynamics from the subsequent time evolution of the mode occupation number $\langle \hat{n}_r^\ell \rangle$ after the proposed quench.

In Fig. 6.10, we illustrate how the dynamics of the integrable dimer $U^{01} = 0$ differ from the nonintegrable case with finite interlevel coupling $NU^{01}/\hbar\omega_0 = 2$. The initial Fock state is the same in both cases. In addition to strong fluctuations, recurrences occur during the time evolution of the mode occupation number in the integrable case. In contrast, we observe relaxation of the mode occupation number to the value predicted by the diagonal ensemble for the nonintegrable system. Henceforth, we shall focus on the nonintegrable case of finite interlevel coupling $U^{01} = U^0/2$.

To demonstrate thermalization, or the lack thereof, we calculate the dynamics of $\langle \hat{n}_r^\ell \rangle$ for pairs of initial Fock states. The initial states in each pair have the same energy E_0. As mentioned before, an important signature of thermalization is the independence of thermal predictions on the details of the initial state apart from conservation laws. The conserved quantities in our system are the total number of bosons and the total energy. For our calculations, we focus on $NU^0/\hbar\omega_0 = 4$ and we use the same set of energies as those in Sec. 6.5.2. The system is said to thermalize if

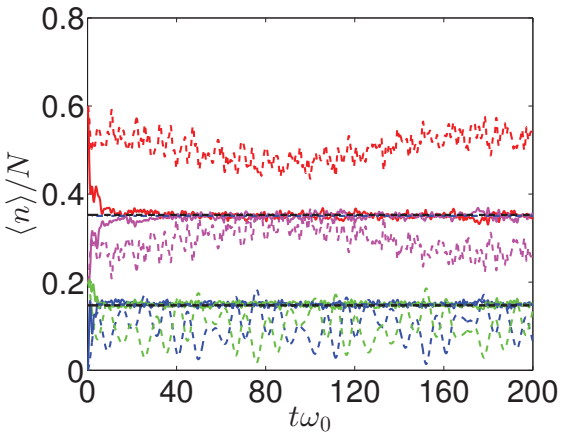

Figure 6.10: (Color online) Relaxation dynamics of occupation number for $NU^0/\hbar\omega_0 = 4$. Integrable case $U^{01}/\hbar\omega_0 = 0$ (dashed line) and finite $NU^{01}/\hbar\omega_0 = 2$ (solid line). The diagonal ensemble average is shown in black solid lines for $NU^{01}/\hbar\omega_0 = 2$. Colors denote: (red) $\hat{n}_L^0$, (magenta) $\hat{n}_R^0$, (blue) $\hat{n}_L^1$, and (green) $\hat{n}_R^1$.

the mode occupation numbers in each pair of initial states tend to the same stationary values and if these values are similar to a corresponding microcanonical ensemble.

In Fig. 6.11(a), we present the time evolution of $\langle \hat{n}_r^\ell \rangle$ for initial states not too close to the ground state energy. For this pair of initial states, the exact relaxation dynamics of the mode occupation numbers settle around their diagonal ensemble values. Moreover, the corresponding microcanonical predictions are practically indistinguishable from the stationary value of $\langle \hat{n}_r^\ell \rangle$. In general, we find that initial states in this region of the spectrum satisfy initial-state independence. These observations are corroborated by the smooth distribution of diagonal ensemble averages in Fig. 6.8(a)-(b).

We proceed to characterization of the relaxation dynamics for initial states around the center of the spectrum. We find that initial states in the lower half but closer to the center of the spectrum will still exhibit thermalization. Typical results for the relaxation dynamics around this energy are shown in Fig. 6.11(b). As expected for initial states in the first half of the spectrum, the long-time averaged occupation number in the lower modes are greater than those in the upper modes. This will

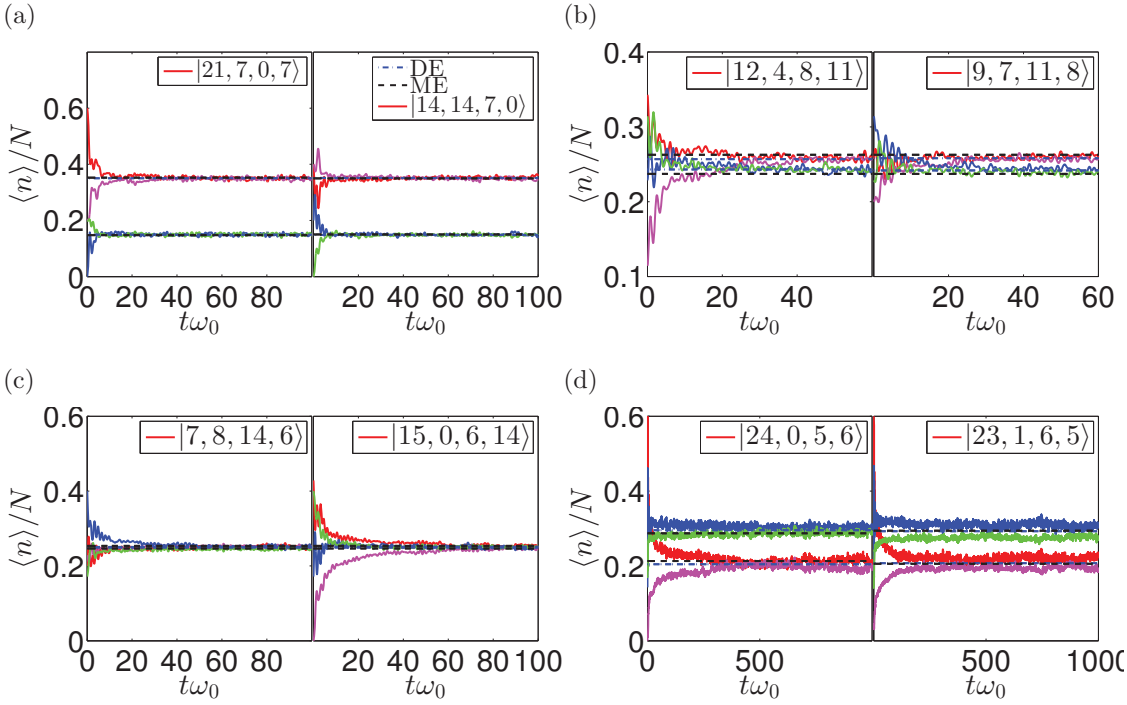

Figure 6.11: (Color online) Dynamics of occupation number for Fock states with the same initial energy (a-d) $E_0/\hbar\omega_0 = 81.053$, $E_0/\hbar\omega_0 = 99.202$, $E_0/\hbar\omega_0 = 101.181$, and $E_0/\hbar\omega_0 = 115.9409$. The dashed-dotted lines correspond to the diagonal ensemble (DE) averages. The dashed lines correspond to the microcanonical ensemble (ME) averages. An initial product state is denoted as $|n_L^0, n_R^0, n_L^1, n_R^1\rangle$. Colors denote: (red) $\hat{n}_L^0$, (magenta) $\hat{n}_R^0$, (blue) $\hat{n}_L^1$, and (green) $\hat{n}_R^1$.

continue to be valid as we increase the initial energy until we finally reach the middle of the spectrum where the system should now relax towards an infinite temperature state. Due to the left-right symmetry of the post-quench Hamiltonian, the infinite temperature state is characterized by having equal mean occupation number between the lower modes and the upper modes, i.e. $\langle \hat{n}_r^0 \rangle = \langle \hat{n}_r^1 \rangle = 0.25N$. This situation is quite similar to a two-level system, with energy spacing $E_2 - E_1$, coupled to an external heat bath at infinite temperature $1/T = \beta = 0$ such that the ratio between the average occupation numbers is $\langle n_2 \rangle / \langle n_1 \rangle = \exp(-\beta(E_2 - E_1)) = 1$. We present in Fig. 6.11(c) examples of time evolution towards a thermal state with almost infinite

temperature.

Even though the mode occupation numbers relax to their diagonal ensemble values in Fig. 6.11(b), there is a slight deviation between the microcanonical ensemble and the stationary values. This failure of the microcanonical ensemble in describing the long-time average can be explained by the fact that the energy distributions in the middle of the spectrum are quite broad as seen in Fig. 6.9(b) and Fig. 6.9(c). It is also possible that the discrepancy can be traced back from finite size effects but further investigation is required in this direction. Nonetheless, we loosely identify the stationary state in Fig. 6.11(b) as thermal state since the exact temporal evolutions of the mode occupancies still relax to the long-time average and, more importantly, this state respects the parity symmetry of the system as the bosons are evenly distributed among the wells. Although, we point out some hints of intermediate relaxation in Fig. 6.11(b) and Fig. 6.11(c). This is clearly seen from the time evolution of $\langle \hat{n}^0_R \rangle$ (blue curve) in the left panel of Fig. 6.11(c) and similarly from $\langle \hat{n}^1_L \rangle$ (magenta curve) in the right panel of the same figure.

Examples of dynamics in the upper half of the spectrum are presented in Fig. 6.11(d) for $E_0/\hbar\omega_0 = 115.94$. Typically, the time evolution of mode occupation numbers will have strong temporal fluctuations in this region of energy. It is also quite obvious from this plot that the exact time evolution of the mode occupation number do not approach neither the diagonal nor the microcanonical ensemble averages. Instead, the steady-state values of the occupation number of the modes in each levels, are no longer equal $\overline{\langle \hat{n}^\ell_L \rangle} \neq \overline{\langle \hat{n}^\ell_R \rangle}$. The stationary states in Fig. 6.11(d) break the reflection symmetry of the system and therefore, we identify these equilibrium states as non-thermal. This is a concrete example of prethermalization dynamics in the system. The apparent absence of thermalization is elucidated by the behavior of the EEV shown in Fig. 6.4. Around $E_0/\hbar\omega_0 \approx 115.94$, the distribution of $\langle k|\hat{n}^\ell_r|k\rangle$ is no longer a smooth function of E_k. However, it is worth mentioning that the violation of the ETH does not guarantee the emergence of prethermalized metastable states. We will further investigate this prethermalization dynamics below.

6.5.4 Subsystem Thermalization and Prethermalization

In order to study subsystem thermalization, we use a mode partitioning scheme different from the usual spatial or site partitioning. For our purpose, a subsystem consists of only of one mode in the system. We calculate the dynamics of the von Neumann entropy S_{vN} of a subsystem in each level. The von Neumann entropy characterizes the degree of entanglement between a mode and the rest of the system. Moreover, this choice of partitioning simplifies the numerical calculation of S_{vN} since the reduced density matrix of a subsystem is already diagonal in the Fock basis. This can be seen if we write the many-body wavefunction in terms of the Fock basis

$$\begin{aligned} |\psi(t)\rangle &= \sum_{n} c_n(t)|n\rangle \\ &= \sum_{m=0}^{N} \sum_{\{p\}=N-m} c_{m,\{p\}}(t)|m\rangle \otimes |p\rangle \end{aligned} \tag{6.20}$$

where $|m\rangle$ is the Fock state of one mode, and $|p\rangle$ is the product state of the possible occupation number in the other three modes. The second sum over the index $\{p\}$ is restricted by the conservation of total number of bosons in the system. We can trace out the environment degrees of freedom $|p\rangle$ and obtain the reduced density matrix of one mode

$$\begin{aligned} \hat{\rho}_s(t) &= \sum_{m=0}^{N} \Bigg(\sum_{\{p\}=N-m} |c_{m,\{p\}}(t)|^2 \Bigg) |m\rangle\langle m| \\ &= \sum_{m=0}^{N} \lambda_m(t)|m\rangle\langle m|. \end{aligned} \tag{6.21}$$

Hence, the von Neumann entropy of a subsystem is

$$S_{\mathrm{vN}}(t) = -\mathrm{tr}[\rho \log \rho] = -\sum_{m=0}^{N} \lambda_m(t) \log \lambda_m(t). \tag{6.22}$$

We are only concerned with the time evolution of initial product state and so, the von Neumann entropy will always start at zero. Following the quench, the von Neumann entropy is expected to increase as the time evolution couples the modes

with one another. We now study the dynamics of the von Neumann entropy for the same set of parameters and initial states used in Sec. 6.5.3. If the $S_{\rm vN}$ were to equilibrate, it should saturate at a value predicted by a Gibbs ensemble. Since the number of bosons and the energy are both not conserved in the subsystem, the appropriate Gibbs ensemble must be the grand canonical one. The number of bosons and the energy in a subsystem are obtained using the local operators

$$\hat{n}_s = \hat{n}_r^\ell; \;\; \hat{H}_s = U^\ell \hat{n}_r^\ell (\hat{n}_r^\ell - 1) + E_r^\ell \hat{n}_r^\ell, \tag{6.23}$$

respectively. Therefore, the density matrix of the grand canonical ensemble is

$$\hat{\rho}_{\rm GC} = \frac{1}{Z} e^{-\beta(\hat{H}_s - \mu \hat{n}_s)} |m\rangle\langle m|, \tag{6.24}$$

where $Z = {\rm tr}(\hat{\rho}_{\rm GC})$. The inverse temperature β and the chemical potential μ are fixed by the conditions: (i) $\overline{\langle \hat{H}_s \rangle} = {\rm tr}(\hat{H}_s \hat{\rho}_{\rm GC})$ and (ii)$\overline{\langle \hat{n}_s \rangle} = {\rm tr}(\hat{n}_s \hat{\rho}_{\rm GC})$ where the overline denotes the expectation value obtained from the diagonal ensemble. To calculate $\overline{\langle \hat{H}_s \rangle}$, we need the long-time average of the two-body local operator $\langle (\hat{n}_r^\ell)^2 \rangle$ obtained in Sec. 6.5.1.

Typical time evolution of the von Neumann entropy is shown in Fig. 6.12. We focus on the long-time dynamics and the general features of relaxation towards the steady-state values (or quasi-steady-state). After the rapid growth in the von Neumann entropy, the behavior of the ensuing dynamics largely depends on the energy of the initial product state. For initial energy near the ground state energy, the von Neumann entropy quickly approaches the Gibbs entropy in a single-step relaxation. Furthermore, the thermalization time is roughly equal to that of the mode occupation number. This is exemplified in Fig. 6.12(a).

For initial states still in the lower half but closer to the middle of the spectrum, we observe a two-step relaxation process such as those presented in Fig. 6.12(b) and Fig. 6.12(c). The von Neumann entropy will first relax to a quasi-stationary value different from the thermal entropy. The metastable states manifest as prethermalization plateaus in the dynamics of the von Neumann entropy. We have observed that not all of the modes will exhibit such prethermalization dynamics. For example in

Fig. 6.12(b), the modes in the upper level of both wells (blue and green) are already fluctuating close to the grand canonical entropy while the mode in the lower level of the right well (magenta) is still trapped in a prethermalized state. The physical reason for why this is the case is unclear at the moment but this is an interesting topic that can be explored in the future. Similar behavior is seen in Fig. 6.12(c), but here the lifetime of the prethermalized state is longer. The lifetime of the prethermalization plateau for $E_0/\hbar\omega_0 = 99.20$ is $t\omega_0 \sim 10$ while for $E_0/\hbar\omega_0 = 101.18$ it is $t\omega_0 \sim 20$. In general, we find that the timescale of the prethermalized regimes increases as the initial energy of the system increases. Consequently, the thermalization time in Fig. 6.12(b) ($t\omega_0 \sim 39$) is smaller than that in Fig. 6.12(c) ($t\omega_0 \sim 103$). The prethermalized states in this part of the spectrum can be physically interpreted as metastable states that temporarily break the parity symmetry of the post-quench Hamiltonian. The plateaus observed in the dynamics of the von Neumann entropy reveal the disagreement between the prethermalized entropy of a mode in one well and its counterpart on the other well. The symmetry is later restored as the system evolves towards parity-conserving thermal states.

Initial states found in the upper half of the spectrum, such as those in Fig. 6.12(d), appear to get trapped in extremely long-lived prethermalized states, at least within the numerically accessible timescales. In Fig. 6.12(d), the von Neumann entropies of each mode in the left well have already reached the Gibbs prediction but the modes in the right well still fluctuate around a non-thermal value. It is worth noting that the metastable states found in this energy region do not show clear signs of any drift towards thermal equilibrium. This behavior seemingly contradicts known results for prethermalization in other nearly integrable models (see Refs. [143, 151]) but there is no reason to rule out with certainty the possibility of such metastable states to decay after sufficient time. This issue is left for future work.

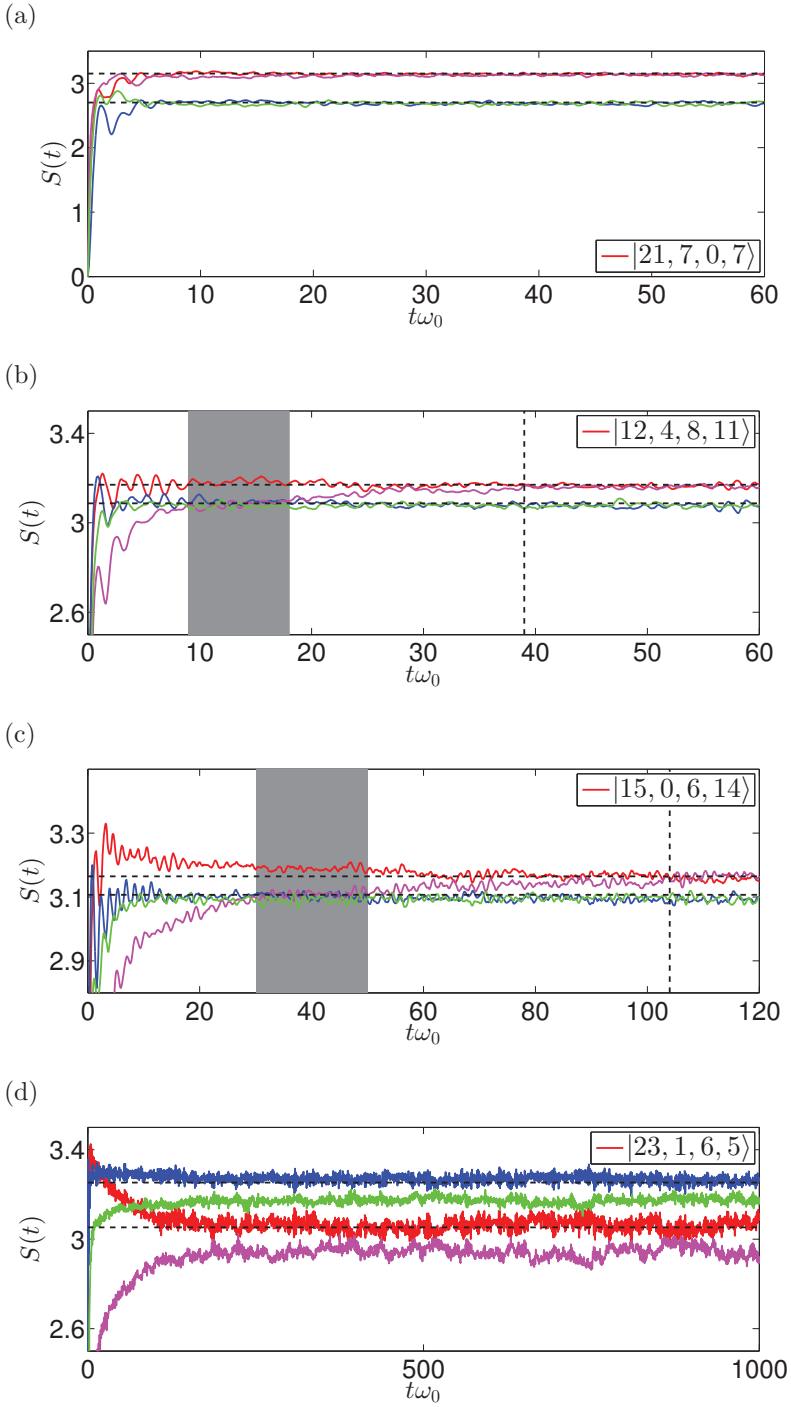

Figure 6.12: (Color online) Time evolution of the von Neumann entropy (solid lines) compared to grand canonical entropy (dashed lines) for (a) $E_0/\hbar\omega_0 = 81.05$, (b) $E_0/\hbar\omega_0 = 99.20$, (c) $E_0/\hbar\omega_0 = 101.18$, and (d) $E_0/\hbar\omega_0 = 115.94$. The shaded area emphasizes the prethermalization plateaus. The vertical dashed lines correspond to the thermalization time after the prethermalized regimes in (b) and (c). Colors denote: (red) $\hat{n}_L^0$, (magenta) $\hat{n}_R^0$, (blue) $\hat{n}_L^1$, and (green) $\hat{n}_R^1$.

6.6 Prethermalization and Timescales

In this section, we use similar arguments as in [147] to understand the emergence of prethermalized states in the system. We split the expression for the time evolution of a generic local operator into three contributions,

$$\langle \hat{A} \rangle = \sum_{k \neq l, \{k,l\} \notin \{a,b\}} C^{k*}_{n_0} C^{l}_{n_0} A_{lk} e^{i(E_l - E_k)t/\hbar} + \sum_{a \neq b} C^{a*}_{n_0} C^{b}_{n_0} A_{ba} e^{i\delta_{ab} t/\hbar} + \sum_{k} |C^{k}_{n_0}|^2 A_{kk} \tag{6.25}$$

where $\{a, b\}$ is a set of indices corresponding to the pairs of quasi-degenerate eigenstates with energy difference $\{\delta_{ab} = E_b - E_a\}$. Written this way, it is possible to associate two different timescales due to the first two sums in Eq. (6.25). For brevity, we shall refer to each sum in Eq. (6.25), in order of its appearance, as the non-degenerate, the quasi-degenerate, and the diagonal contributions. The non-degenerate contribution is associated with a thermalization timescale due to dephasing as shown in Eq. (6.4). It is worth mentioning that the ETH already puts a strong restriction on the off-diagonal elements, $A_{kk'} = \langle k|\hat{A}|k'\rangle$, being exponentially small compared to its diagonal counterpart. Recall that this is the nature of the ETH ansatz given by Eq. (2.61) as discussed in Chapter 2.3.2. And so, we instead turn our attention on possible interplay between the structure of the spectrum and the coefficients $C^{k}_{n_0}$.

The energy distribution of an initial state plays an important role in understanding the stages of relaxation dynamics in our system as they provide crucial information on the chaoticity or sparsity of the coefficients $C^{k}_{n_0}$. The width of the energy shell measures the connectivity of an initial state to the eigenstates of the final Hamiltonian. An initial state that thermalizes will never be fully extended with respect to the eigenstates as seen in Fig. 6.9 and therefore, the width of the LDoS will limit contributions in Eq. (6.25) of eigenstates with energies far from the initial energy. This naturally justifies a separation of the spectrum into different sectors. We can then analyze the structure of the eigenenergies within each sector.

We divide the full spectrum into three sectors in accordance to the choice of initial

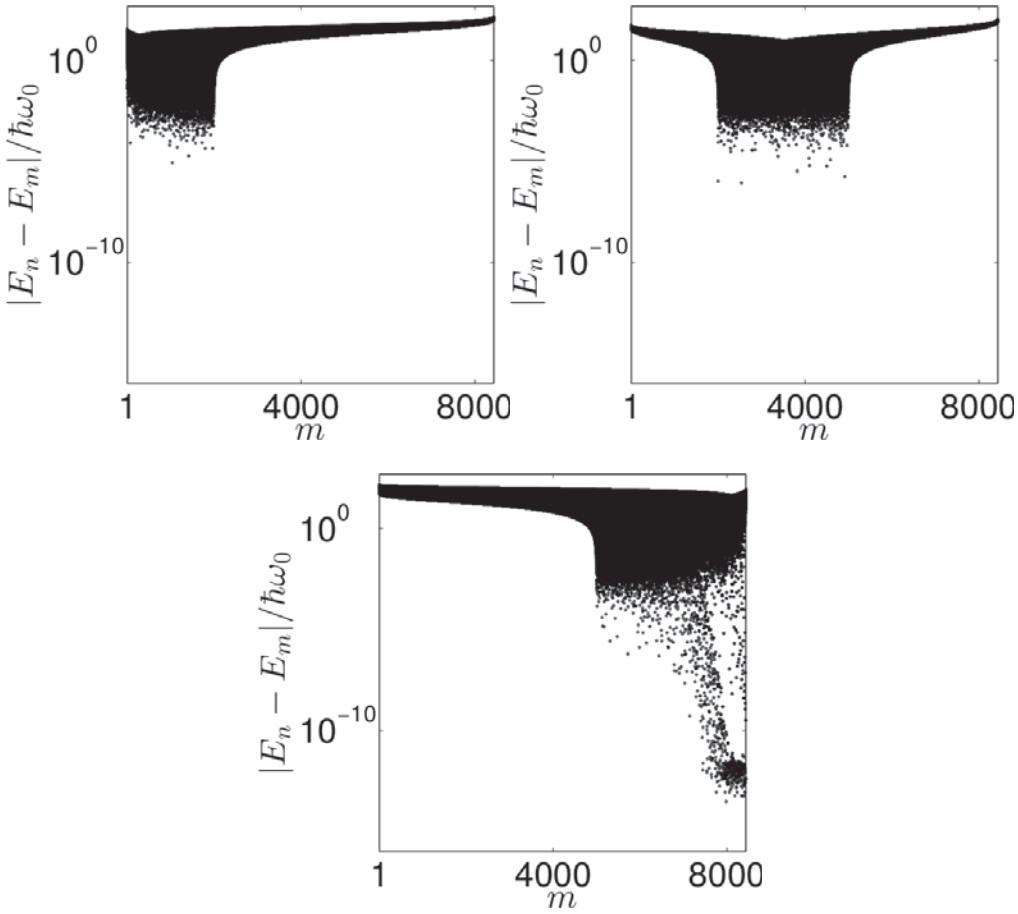

Figure 6.13: Energy differences across the spectrum. The eigenenergies E_n are arranged in increasing order $n \in [1, D]$ where D is the dimension of the Hilbert space. (Top-Left) Low energy sector $n \in [1, 2000]$. (Top-Right) Middle energy sector $n \in [2001, 5000]$. (Bottom) High energy sector $n \in [5001, D]$.

energies in Sec. 6.5.2 and Sec. 6.5.3, i.e. $E_0/\hbar\omega_0 = 81.05$ is in the low energy sector; both $E_0/\hbar\omega_0 = \{99.20,\ 101.18\}$ are in the middle energy sector; and $E_0/\hbar\omega_0 = 115.94$ is in the high energy sector. The results are presented in Fig. 6.13. The outliers in each plots represent quasi-degeneracies of pairs of even and odd eigenstates. The energy differences, in general, decrease from $\sim 10^{-5}$ in the low energy sector to $\sim 10^{-6}$ in the middle sector. This explains the increase in the observed thermalization time from $t \lesssim 10^1$ for initial states with low energy to $t \sim 10^2$ for initial energies in the mid-spectrum. Also, there is perceivable increase in the prevalence of quasi-degenerate pairs as you go to higher energies. This means that for sufficiently high initial energies, the quasi-degenerate contribution in Eq. (6.25) becomes more dominant and an intermediate timescale may emerge. Thus, we conjecture that the presence of quasi-degeneracies led to the prethermalization observed in the system. Moreover, the width of the energy shell restricts the connectivity among the $C^k_{n_0}$ such that only the eigenenergies near an initial energy will contribute significantly to the relaxation dynamics. For this reason, initial states in the low energy sector are unaffected by the quasi-degeneracies in the high energy sector and we only find fast and single-stage relaxation for such initial states (see Fig. 6.11(a) and Fig. 6.12(a)). In contrast, metastable states start to appear during the relatively slower relaxation dynamics of initial states in the middle sector (see Fig. 6.11(b)-(c) and Fig. 6.12(b)-(c)). One of the main results of this work is this crossover behavior from single-stage to two-stage relaxation process without changing the parameters of the Hamiltonian. Instead, we can probe this transition just by increasing the energy of the initial product state. On the other hand, most of the quasi-degeneracies are situated in the high energy sector. In addition to this, the energy difference can reach as low as $\sim 10^{-15}$ in this sector, which is several orders of magnitude lower than the other sectors. These two factors combined may explain why initial states in the high energy sector exhibit long-lived prethermalization plateaus (see Fig. 6.11(d) and Fig. 6.12(d)).

6.7 Summary and Conclusion

In this work, we have numerically investigated the relaxation dynamics following an integrability breaking quench in a double-well system. We obtained the distribution of consecutive level spacings in order to characterize the spectral statistics of the system. Then, we identified the post-quench Hamiltonian as non-chaotic over a wide range of interaction parameters due to the absence of level repulsion. The enhanced level clustering for strong interactions is attributed to the increase in the amount of quasi-degenerate pairs. Thus, for the chosen trap parameters, the non-integrable post-quench Hamiltonian is close to an integrable point.

In order to check the requirements for the validity of the ETH in our system, we obtained the distribution of the EEV for various interaction parameters. In general, smooth distributions of the EEV are found in the lower half of the spectrum. By changing the interaction strength, we observed that the distribution of the EEV broadens as the number of quasi-degenerate energy levels increases. At the moment, we only provided numerical evidence that the ETH holds for the system, albeit having a spectral statistics akin to integrable models. It would be interesting to see whether the weak ETH scenario studied in Refs. [141, 177] can be observed in our system. This can be a subject of future study involving careful scaling analysis of the model.

We compared the long-time averages of local operators calculated using the diagonal ensemble and their microcanonial values for a set of initial product states spanning all possible combinations of Fock states in each mode. The range of energy where the diagonal ensemble averages are well described by the microcanonial ensemble is consistent with that for which the ETH is satisfied. Therefore, we have numerically verified that it is possible for the system to thermalize. We computed the LDoS of typical initial states with energy within the first half of the energy spectrum and we classified them as chaotic since they ergodically fill the energy shell. These results allowed us to extend the scope of the main conclusion in Ref. [156], to include chaotic initial states away from the middle of the spectrum that thermalize under time evolution of a non-chaotic Hamiltonian.

Using generic initial product states, we found that the system may exhibit thermalization in the sense that the exact time evolution of local operators relax to the diagonal ensemble predictions and these values are close to corresponding Gibbs ensemble predictions. In particular, we demonstrated that the mode occupation numbers of certain initial states would dynamically approach the diagonal ensemble averages. The energy of such initial state is within the range of energy for which initial states are delocalized and the ETH is valid. Observables for initial states in the high energy region are shown to relax but not towards the diagonal ensemble values. This led us to think about the possibility of having two-stage relaxation dynamics in the system. In fact, the emergence of prethermalized states became clear when we examined the time evolution of the von Neumann entropy in each mode. Specifically, we have observed intermediate relaxation to metastable states for initial energies close to the middle of the spectrum. Finally, we have argued that delocalization of initial states together with the details of the energy spectrum such as quasi-degeneracies play vital roles in understanding prethermalization and the relaxation timescales of the system. One of the key contributions of this work is the possibility of probing, by simply changing initial product states, the continuous transition from single-step to two-step relaxation at fixed Hamiltonian parameters.

One possible direction of future work is a careful study on how finite-size effects may affect the phenomenon observed in this work including the emergence of prethermalization and the behavior of the EEV as the size of the system is increased. Also, the question whether an initial state with LDoS different from the energy shell but still has some kind of structure, as in Fig. 6.9(d), will eventually thermalize remains an open issue for future study.

Chapter 7

Semiclassical perspective on thermalization of ultracold bosons in a 1D double-well potential

7.1 Introduction

In Chapter 6, we have shown that the system described by a multilevel Bose-Hubbard model can exhibit signatures of quantum thermalization in the level of local observables. The same out-of-equilibrium dynamics investigated in the previous chapter can be also studied in a different perspective using phase space methods. Here, we can look at properties and statistics of single trajectories used to approximate expectation values of relevant observables instead of analyzing properties of the full spectrum or individual eigenstates as done in the previous chapter. More specifically, we employ a phase-space representation called the Wigner representation. Calculating the time-evolution semiclassically by means of the truncated Wigner approximation enables us to gain insight on how observables equilibrate through the lens of the associated quasiprobability distributions. We show that the long-time marginal distribution of the Wigner function agrees with both the quantum mechanical prediction according

to the so-called diagonal ensemble and also to the corresponding microcanonical distribution in phase-space satisfying the appropriate contraints given by the energy and the total number of particles.

7.2 Truncated Wigner Approximation

In the classical limit of large occupation in each mode, $N \to \infty$, we proceed by making use of a phase-space method called the truncated Wigner Approximation. This method amounts to solving the semi-classical counterpart of the Heisenberg equation of motion for the Hamiltonian in Eq. (6.6) with different initial conditions, which accurately samples the quantum noise in the system, then averaging afterwards.

The operators $\hat{b}_r^{l\dagger}$ and $\hat{b}_r^l$ can be treated as complex c-numbers. The semi-classical form of the Heisenberg equation of motion or equivalently the Gross-Pitaevskii equation reads:

$$i\hbar\frac{\partial b_r^l}{\partial t} = \left\{ b_r^l, H_W \right\}_C = \frac{\partial H_W}{\partial b_r^{l*}} \tag{7.1}$$

where $\{\cdots\}_C$ is the Poisson bracket and H_W is the Weyl ordering of the Hamiltonian operator which is calculated by replacing $\hat{b}_r^l \to \left(b_r^l + \frac{1}{2}\frac{\partial}{\partial b_r^{l*}} \right)$ and $\hat{b}_r^{l\dagger} \to \left(b_r^{l*} - \frac{1}{2}\frac{\partial}{\partial b_r^l} \right)$ [55]. This is called the Bopp representation of the operators. We apply this to the annihilation and creation operators in the two-band Bose Hubbard Hamiltonian (6.6)

$$\begin{aligned} H_W = &- \sum_{r\neq r',l} J^l b_r^{l*} b_{r'}^l + \sum_{r,l} U^l \left[(b_r^{l*})^2 (b_r^l)^2 - b_r^{l*} b_r^l + \frac{1}{2} \right] \\ &+ \sum_{r,l} E_r^l (b_r^{l*} b_r^l - \frac{1}{2}) + U^{01} \sum_{r,l\neq l'} \Bigg[\\ &(b_r^{l*})^2 b_r^{l'} b_r^{l'} + 2\left(b_r^{l*} b_r^l b_r^{l'*} b_r^{l'} - \frac{1}{2} b_r^{l'*} b_r^{l'} - \frac{1}{2} b_r^{l*} b_r^l + \frac{1}{4} \right) \Bigg] \end{aligned} \tag{7.2}$$

Then, for our system, Eq. (7.1) simplifies as

$$\begin{aligned} i\hbar\frac{\partial b_s^m}{\partial t} = &- J_m b_{s'}^m + (E_s^m - U^m) b_s^m + 2U^m |b_s^m|^2 b_s^m \\ &+ 4U^{01} b_s^m |b_s^{m'}|^2 + 2U^{01} b_s^{m*} (b_s^{m'})^2 - 2U^{01} b_s^m \end{aligned} \tag{7.3}$$

where s' and m' mean different well and energy level respectively. Depending on the initial state, we use the appropriate sampling for the initial conditions when solving the coupled differential equations Eq. (7.3) [54, 178]. For coherent state, which corresponds to a condensed state of bosons, the initial conditions are sampled as $b = b_0 + \frac{1}{2}(\nu_1 + i\nu_2)$ where $|b_0|^2 = n + 1/2$ and ν_i are Gaussian random variables. It is appropriate to consider the sampling for Fock state as well. Fock state is sampled as $b = (p + q\nu)e^{i2\pi\xi}$ where ν is a Gaussian random variable and ξ is a uniform random variable in the interval $[0, 1]$, $p = \frac{1}{2}(2N + 1 + 2\sqrt{N^2 + N})^{1/2}$ and $q = 1/(4p)$.

7.3 Thermalization from semiclassical dynamics

In order to compare with results obtained in Chap. 6, we use the same Bose-Hubbard parameters as discussed in Sec. 6.2 for the following numerical simulations. We study the dynamics from initial Fock and coherent states with the same energy $E_0/N \approx 2.25\hbar\omega_0$, which corresponds to the lowest energy considered in the time evolution found in Sec. 6.5.3. Before we study the quantum dynamics, it is insightful to first look at two realizations of initial conditions and compare them from another. This amounts to solving the set of coupled Gross-Pitaevskii equations above using a deterministic initial condition. In Fig. 7.1, we present a qualitative picture of trajectories for two different initial conditions with one differing from the other by one atom added to the $|n_L^1\rangle$ and one atom subtracted from $|n_L^0\rangle$. In the integrable limit of $U^{01} = 0$, regular motion is seen from the nearly periodic oscillation of $|b_L^0|^2$ as function of time. On the other hand, for finite U^{01} chaotic or irregular trajectories are obtained.

The relaxation dynamics from TWA calculations is shown in Fig. 7.2. The final relaxed values of the occupation numbers are in excellent agreement with the quantum diagonal ensembles prediction. For the two different initial conditions the upper and lower modes thermalize at $n_L^0 \approx n_R^0 \approx 0.4N, n_L^1 \approx n_R^1 \approx 0.1N$. Independence on the details of the initial state apart from constraints such as energy is one criterion for thermalization. The Wigner trajectories exhibit chaotic behavior by quickly filling

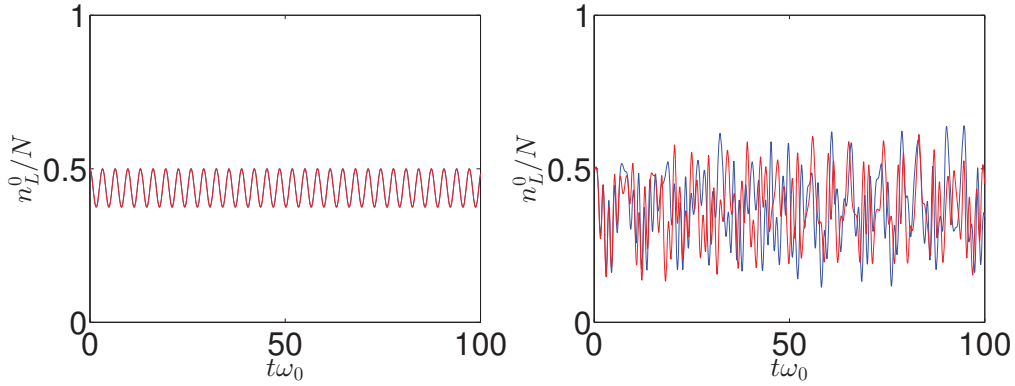

Figure 7.1: Comparison of two different trajectories with slightly different initial states (difference of only one boson being transferred from the lower level to the upper level of the left well). (Left) In the integrable limit of the single band model, the trajectory of a slightly perturbed initial condition is almost indistinguishible to the original. (Right) While for finite U^{01}, chaotic behavior is observed for slight mismatch of initial conditions.

the available phase space, as shown in Fig. 7.3. Good agreement between the TWA results and the diagonal ensemble predictions suggest that the marginal distributions of a phase-space distribution, in this particular case the Wigner function, are consistent with the corresponding microcanonical distributions. This is in agreement with previous results found in Refs. [179,180] where it was conjectured that thermalization is manifested in uniformly distributed quasiprobability distributions as they spread over the available energy shell.

In the context of full quantum simulations, the diagonal ensemble $\hat{\rho}_m$ contains all necessary information about the relaxed state. Our aim is to calculate the population distribution in a mode P_n and compare it with the analogous distribution derived from the TWA approximation. This quantity simply gives the occupancy of that mode, $\langle \hat{n} \rangle = \sum_{n'} n' P_{n'}$, and the reduced density matrix of that mode, $\sum_{n'} P_{n'} |n'\rangle\langle n'|$. To calculate this density distribution we express $\hat{\rho}_m$ via the Fock basis $\hat{\rho}_m = \sum_{k,m,n} |C^k_{n_0}|^2 C^k_n C^{k*}_m |n\rangle\langle m|$ yielding $P_n = \sum_k |C^k_{n_0}|^2 |C^k_n|^2$. We found a very good agreement with the analogous distribution obtained from the TWA calculations, as it is shown in Fig. 7.4. The later is obtained by noting that $n^l_r \to |b^l_r|^2$.

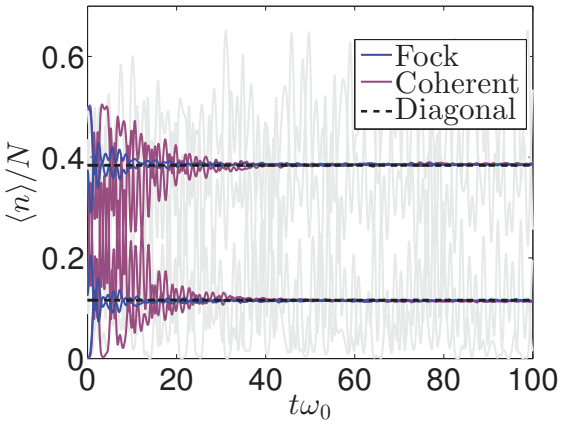

Figure 7.2: TWA dynamics of the occupation numbers in each mode from Fock and coherent initial states with the same energy $E_0/N \approx 2.25\hbar\omega_0$ and narrow energy variances $\Delta E_0/E_0 = 0.09$ and 0.02 respectively. They equilibrate at values which are in excellent agreement with the quantum diagonal ensembles prediction for $N = 40$. This diagonal ensemble value has been calculated in the same manner described in Chapter 6 A single TWA trajectory is shown in semitransparent gray; it exhibits chaotic behavior. Only averaging over many such trajectories leads to the correct relaxed values of the occupation numbers.

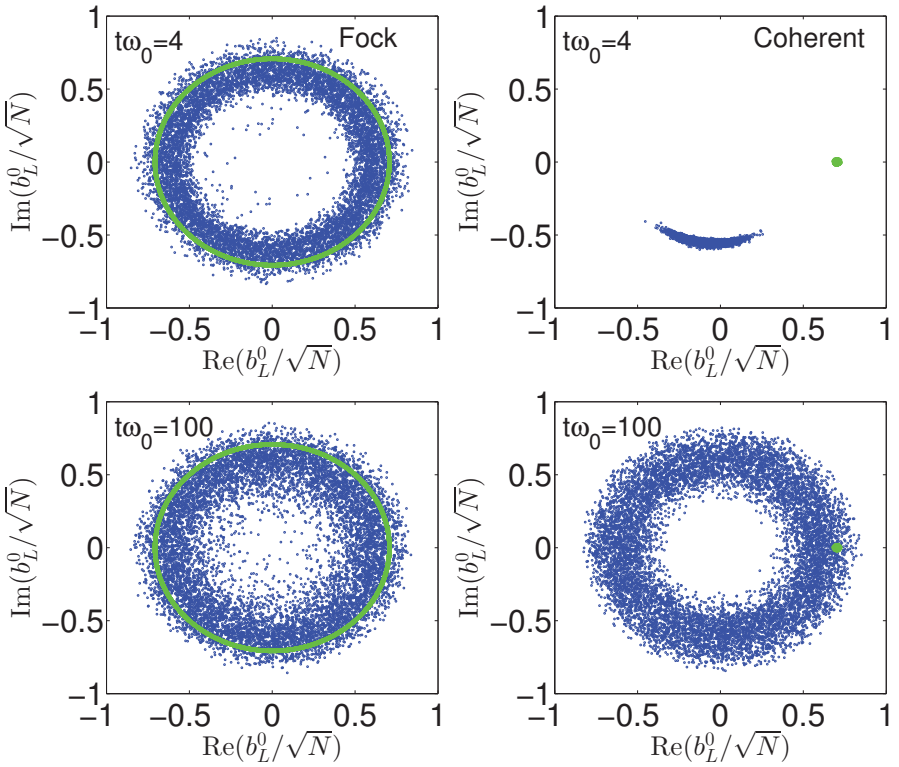

Figure 7.3: Ergodicity in TWA. As an example we show Wigner distributions of one of the lower levels. Initially the system is prepared in the Fock state (green cycle shown on the left) or in the coherent state (green bump shown on the right). Trajectories sampled from the initial states fill the available phase space as time evolves (blue dots). The distributions become essentially the same at some time and after that they do not change, which suggests thermalization is reached within TWA. In this sense, quantum fluctuations of the initial state turn into thermal fluctuations in the course of evolution.

The resulting population distributions can be inferred from the ergodicity of the Wigner trajectories originating from the initial sampling which is narrow in energy. The Wigner distribution function of the entire system can thus be represented as some sharply peaked function $\bar{\delta}(H_W - E_0)$, the microcanonical analog of the quantum case. We approximate it with the Gaussian $\bar{\delta}(x) = \frac{1}{\sigma\sqrt{\pi}}\exp(-x^2/\sigma^2)$ with $\sigma \sim \Delta E_0$. The Wigner distribution of a mode b_r^l is then given by integrating out over all modes but one, $W_m(b_r^l, b_r^{l*}) = \int \bar{\delta}(H_W - E_0)\bar{\delta}((\sum b_r^{l*} b_r^l) - N) \prod_{l' \neq l,\ r' \neq r} db_{r'}^{l'\,*} db_{r'}^{l'}$, which is numerically evaluated using Monte Carlo integration upon the change of variables $\{b_r^{l*}, b_r^l\} \rightarrow \{|b_r^l|, \theta_r^l\}$. Specifically, we set $b_r^{l*} = |b_r^l|e^{-i\theta_r^l}$ and $b_r^l = |b_r^l|e^{i\theta_r^l}$. Then marginal probability after changing variable is given by

$$P(b_r^{l*}, b_r^l) db_r^{l*} db_r^l = |\mathcal{J}_r^l| P(|b_r^l|, \theta_r^l) d|b_r^l| d\theta_r^l, \tag{7.4}$$

where the Jacobian of the transformation is given by

$$|\mathcal{J}_r^l| = \begin{vmatrix} \frac{\partial b_r^l}{\partial |b_r^l|} & \frac{\partial b_r^l}{\partial \theta_r^l} \\ \frac{\partial b_r^{l*}}{\partial |b_r^l|} & \frac{\partial b_r^{l*}}{\partial \theta_r^l} \end{vmatrix} = 2|b_r^l|. \tag{7.5}$$

The Weyl-transformed Hamiltonian expressed in terms of the new phase-space variables becomes

$$\begin{aligned} H_W = &- \sum_{r \neq r', l} J^l |b_r^l||b_{r'}^l| e^{i(\theta_{r'}^l - \theta_r^l)} + \sum_{r,l} U^l \left[|b_r^l|^4 - |b_r^l|^2 + \frac{1}{2} \right] \\ &+ \sum_{r,l} E_r^l (|b_r^l|^2 - \frac{1}{2}) + U^{01} \sum_{r, l \neq l'} \Bigg[\\ &|b_r^l|^2 |b_r^{l'}|^2 e^{2i(\theta_r^{l'} - \theta_r^l)} + 2\left(|b_r^l|^2 |b_r^{l'}|^2 - \frac{1}{2}|b_r^{l'}|^2 - \frac{1}{2}|b_r^l|^2 + \frac{1}{4} \right) \Bigg]. \end{aligned} \tag{7.6}$$

The microcanonical marginal distribution will then read as

$$P(|b_r^l|, \theta_r^l) = \int \frac{8}{\sigma^2 \pi} e^{-(H_W - E)^2/\sigma^2} e^{-(\sum |b_r^l|^2 - N)/\sigma^2} \prod_{l' \neq l,\ r' \neq r} |b_{r'}^{l'}| d|b_{r'}^{l'}| d\theta_{r'}^{l'}. \tag{7.7}$$

The evaluation of the above integral is done using Markov-Chain Monte-Carlo method by choosing an arbitrary proposal distribution from the integrand, which is sampled

to satisfy detailed balance condition. Upon evaluation of the integral, we found good agreement between the microcanonical marginal distribution of a particular mode and the corresponding Wigner distributions obtained from TWA as shown in Fig. 7.4.

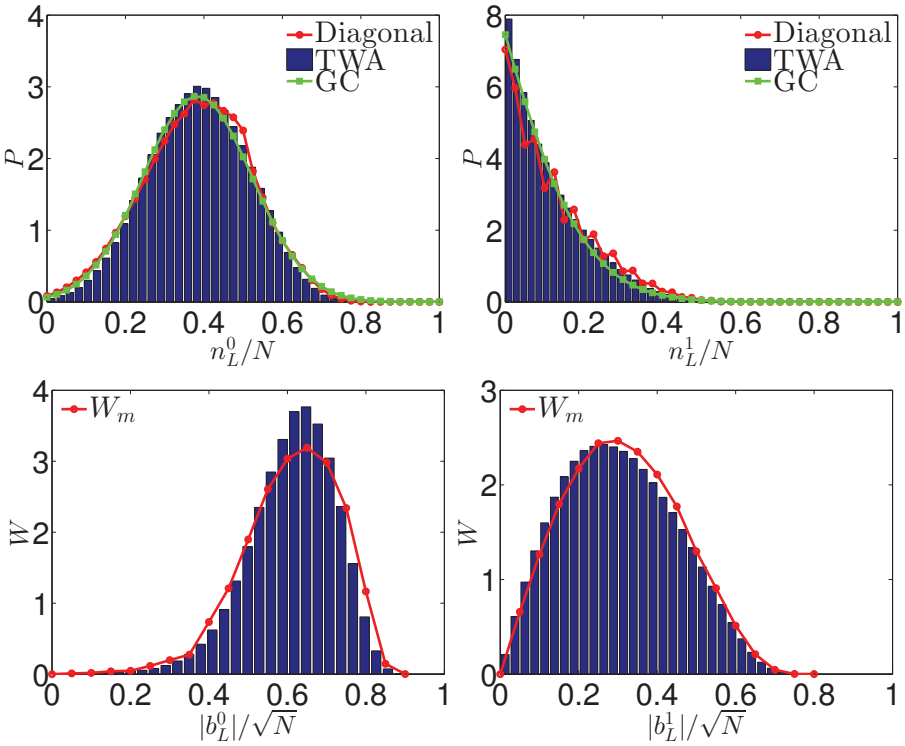

Figure 7.4: (Upper panels) Comparison of the distributions P_n derived from the diagonal ensemble with the corresponding distributions derived from the grand-canonical ensembles. Both are compared with the corresponding data extracted from TWA. (Lower panels) The good agreement between the exact Wigner distribution and the distribution W_m.

Having observed equilibration in each of the four modes, we now examine the states of each mode in more detail. Our aim is to demonstrate that the equilibrium states are thermal. In studying thermalization in closed quantum systems, the Hamiltonian of a system is usually split into several parts, $\hat{H} = \hat{H}_S + \hat{H}_B + \hat{H}_{int}$, representing the subsystem, the bath, and interactions between them leading to their mutual thermalization. Equation (6.6) represents such a situation: Each of the four modes can be regarded as a subsystem ($= \hat{H}_S$) coupled to the rest of the system

($= \hat{H}_B$), via the tunneling and coupling terms ($= \hat{H}_{int}$). The modes may exchange energy and particles via tunneling; therefore thermal states of each mode are expected to be described by grand-canonical ensembles $\hat{\rho}_{GC} \sim e^{-\beta(\hat{H}_S - \mu\hat{n}_S)}$, where for a given mode $\hat{H}_S = U^l \hat{n}_r^l(\hat{n}_r^l - 1) + E_r^l \hat{n}_r^l$ and $\hat{n}_S = \hat{n}_r^l$. To ensure that the resulting distributions are thermal, we fitted them with the grand-canonical distribution $\hat{\rho}_{GC}$.

7.4 Summary

We have demonstrated that each of the four modes thermalizes with the rest of the system. We did this as follows: each mode is weakly coupled to the other modes via tunneling and interaction terms in the Hamiltonian so that they can exchange particles and energy. As a result, the corresponding distributions are expected (and were shown) to be well described by the grand-canonical ensembles with appropriate temperatures and chemical potentials. Moreover, initial state independence of the relaxed states provides further evidence of thermalization in each mode. Finally, the relaxed distribution of trajectories in each mode can be inferred from a microcanonical counterpart of the Wigner distribution of the whole system.

We have also shown that the semiclassical truncated Wigner approach and full quantum description agree in reproducing the states of each mode after they have been thermalized. While the quantum description of thermalization has been elucidated extensively in the literature [16, 38, 39, 181, 182], in this work we analyzed the semiclassical approach in order to seek further insights into the physics of quantum thermalization.

Chapter 8

Conclusions

In this thesis we have studied various nonequilibrium dynamics of few- to many-body interacting bosons. In particular, we have considered as few as two bosons but we have also investigated the semiclassical limit of large occupation number. Our work in essence can be divided into two parts: (1) many-body dynamics according to the MCTDHB method and (2) quantum ergodicity in a double-well system.

In suggesting a new convergence test based on the center-of-mass motion, we have uncovered the shortcomings of the MCTDHB method. We have specifically demonstrated the inability of one usual criterion to detect non-convergence in the numerical results produced by the MCTDHB. We have also shown a pathologically slow convergence problem for attractively interacting bosons released from harmonic confinement. The same convergence issue is eventually linked back to previously published MCTDHB results on the creation of the so-called fragmentons which in this thesis we show are nothing but numerical artefacts from unconverged MCTDHB wave functions. Despite the limitations of MCTDHB, it can still be considered a useful many-body numerical method especially for few bosons and in cases where only few single-particle energy states are relevant in the problem. This is exactly the type of system that we have considered in our investigation of interaction blockade of up to three bosons. Our numerical results based on converged MCTDHB simulations corroborate our experimental proposal for observing interaction blockade and the

expected bosonic enhancement factor using asymmetric double-well configurations.

In the second half of thesis, we have investigated quantum ergodicity in a double-well system. Nonintegrability is considered as a key ingredient for the validity of the ETH which predicts the dynamical equilibration of observables towards a microcanonical prediction. And in our double-well system, integrability can be broken by going beyond the one-level approximation and allowing states in the next energy level to participate in the rich dynamics after a quantum quench. This type of system gives us a unique opportunity to study mode partitioned subsystems and how they can thermalize in the context of the ETH. This is in contrast to the usual space-partitioned subsystems of having multiple lattice sites considered in previous numerical experiments. We have shown that indeed the two-level double well system can exhibit signatures of chaoticity and thermalization dynamics in the quantum level. We then took another step forward by taking the semiclassical limit of large N in the system and this made the quantum dynamics amenable to the TWA. This semiclassical perspective allowed us to construct marginal distributions of the Wigner function and we show that they compare well with corresponding distributions predicted by other ensemble which include the diagonal, grand-canonical, and microcanonical ensemble.

Appendix A

Parity symmetry

The reflection symmetry about the center of the single particle potential as shown in Fig. 6.1 allows for eigenstates which are combination of symmetric/antisymmetric pairing of Fock states, i.e. $|20, 15, 0, 5\rangle \longleftrightarrow |15, 20, 5, 0\rangle$. We label an eigenstate as even/odd (+/-) when

$$|k\rangle_{\pm} = \sum_{\{n\}} (C_n^k |n\rangle \pm C_n^k \hat{P}|n\rangle)/2 \tag{A.1}$$

where we sum over all combination of Fock states $\{n\}$ and the parity operator $\hat{P}|n_L^0, n_R^0, n_L^1, n_R^1\rangle = |n_L^1, n_R^1, n_L^0, n_R^0\rangle$. Examples of even and odd eigenstates are shown in Fig. A.1. Notice the sizeable amount of nonzero C_n^k and how they fluctuate around zero. This can be used to introduce the concept of chaotic eigenstate which is not to be confused with chaotic initial state discussed in Chapter 6. Chaotic eigenstates are characterized by delocalization in a particular basis.

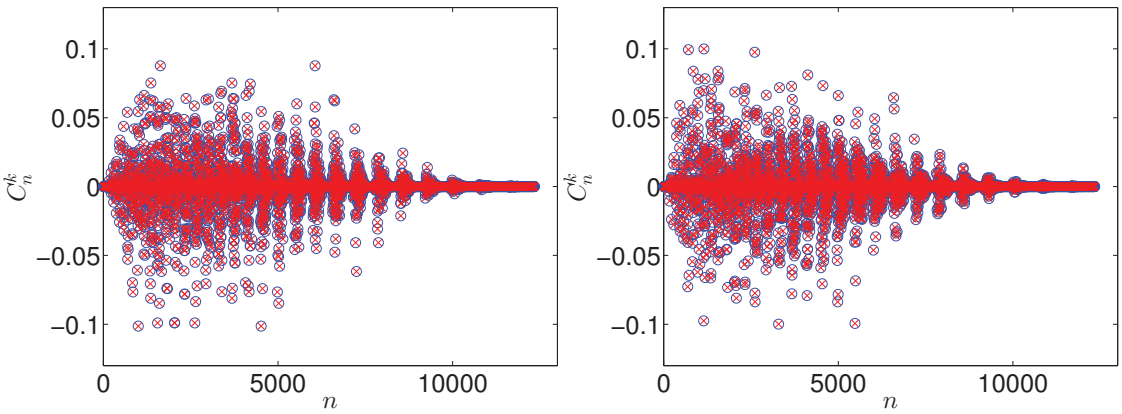

Figure A.1: The red crosses denote the overlap coefficient C_n^k of the corresponding pair of the blue circles. When the two coincide with each other, the eigenstate has a definite parity. (Left) Even-parity eigenstate. (Right) Odd-parity eigenstate in which the red crosses are now $-C_n^k$.

Appendix B

Imaginary time propagation

When initializing the MCTDHB simulation according to some initial ground state, the time evolution equations for the single-particle functions and the expansion coefficients are both propagated in imaginary time, i.e., $\tau = -it$. Here, we briefly review the basic ideas of imaginary time propagation scheme. Consider the time-evolution equation in imaginary time for an arbitrary wave function,

$$\frac{\partial \psi(\vec{x}, \tau)}{\partial \tau} = H\psi(\vec{x}, \tau). \tag{B.1}$$

An initial guess state $\psi(\vec{x}, 0)$ can then be propagated according to

$$\psi(\vec{x}, \tau) \propto e^{(-\tau H)}\psi(\vec{x}, 0) \tag{B.2}$$

which can be expanded in terms of the eigenstates $\phi_i(\vec{x})$of the Hamiltonian H with corresponding eigenvalues ϵ_i

$$\psi(\vec{x}, \tau) \propto \sum_i C_i \phi_i(\vec{x}) e^{(-\tau \epsilon_i)}. \tag{B.3}$$

Clearly from Eq. (B.3), the imaginary time-evolution leads to an exponential decay of all terms in the series expansion. In the limit as $\tau \to \infty$, the term associated to the ground-state $\phi_0(\vec{x})\exp(-\epsilon_0 \tau)$ decays the slowest and eventually becomes the most dominant contribution.

Appendix C

Improved relaxation

We briefly outline the improved relaxation scheme used to obtain the excited energy eigenstates in Chapter 5. Firstly, initialize the scheme by guessing a set of single-particle functions. Then, the expansion coefficients or the $\vec{C}$-vectors are propagated by obtaining the eigenvalues and eigenvectors of the time-dependent Hamiltonian matrix $\mathbf{H}$ expressed in the basis of the aforementioned single-particle functions

$$H_{nn'}(t) = \langle n_1, n_2, \ldots, n_M; t|\hat{H}|n'_1, n'_2, \ldots, n'_M; t\rangle. \tag{C.1}$$

Choose the nth eigenvector (state of interest) of H and propagate the single-particle functions in imaginary time with finite time interval according to this new eigenvector. Update the single-particle functions and repeat the whole process iteratively until convergence to the energy of the state of interest is achieved.

Appendix D

Discrete variable representations

We now briefly discuss the discrete variable representation (DVR) that we have used in Chapter 5 to obtain the effective Hubbard parameters for a three dimensional system. Note that the following discussion is based on Ref. [28].

Before proceeding to actual details of the DVR, let us first give a general overview of advantages of the DVR over other numerical methods. It can be argued that DVR-based methods are comparatively simpler that pure spectral methods since DVR methods only require diagonalization of matrices whose elements are analytically known. This is in contrast to spectral methods wherein Hamiltonian matrices are built from integrals which either have to be evaluated analytically or often times numerically. The efficiency of DVR methods gives it an advantage over its grid-based counterparts. For example in standard finite difference methods, the error scales as a power of the number of grid points, while DVR methods have exponential convergence with the grid points.

The DVR can be defined as follows [28, 183]. Let us consider a domain $\mathcal{D} \subseteq \mathbb{R}$ and a Hilbert space $\mathcal{H}$ of functions on $\mathcal{D}$. We intend to find a subspace $\mathcal{S}_K$ of $\mathcal{H}$ with refinement parameter K that captures the part of $\mathcal{H}$ spanned by low-energy eigenstates of the potential. We then introduce a Hermitian projection operator $\mathcal{P}_K$ that projects states into the subspace $\mathcal{S}_K$. Let us also select some set of N grid points $\{x_n\}$ where $N = \dim\mathcal{S}_K$. If the projected delta functions $|x_n\rangle = \mathcal{P}_K\delta(x - x_n)$

are orthogonal, then we the set of $\mathcal{P}_K$ and $\{x_n\}$ can be called a *discrete variable representation*. In this representation, the wave function is expanded in the basis formed by a normalized set of these projected delta functions $|\Delta_n\rangle = \mathcal{P}_K|x_n\rangle/\sqrt{N_n}$, where N_n is a normalization factor. The key advantages of DVR can be seen from how external potentials $V(x) \in \mathcal{S}_K$ have diagonal matrix representation and an analytic representation of the kinetic energy operator. It also has exponential convergence in N.

We now move on to a discussion of a specific type of DVR basis which is the so-called sinc DVR [184]. A much more detailed discussion and derivation of important properties of this type of DVR can be found in Ref. [28]. For the sinc DVR, we consider a domain spanned by the real line $\mathcal{D} = (-\infty, \infty)$. We choose the projection operator $\mathcal{P}_K$ to project into the subspace of wave functions with momentum cutoff given by K.

$$\mathcal{P}_K = \int_{-K}^{K} dk|k\rangle\langle k|, \tag{D.1}$$

where $\langle x|k\rangle = e^{ikx}/\sqrt{2\pi}$ are plane waves with delta-function normalization and N equally spaced grid points, $x_n = n\pi/k$. In doing so, we are essentially projecting into a subspace of the Hilbert space spanned by non-interacting states with energy less than $E_K = \hbar^2K^2/2M$ where M is the mass. Then the delta functions projected into $\mathcal{S}_K$ are sinc functions

$$\langle x|\Delta_n\rangle = \frac{1}{\sqrt{\Delta x}}\text{sinc}(\pi(x - x_n)/\Delta x), \tag{D.2}$$

where $\Delta x = \pi/K$ is the grid spacing. These functions have a nice property that they are nonzero only at a single grid point and they vanish on all others. This property automatically satisfies the orthonormality requirement for a DVR. It also has another remarkable property such that the overlap between two states is

$$\int dx\langle\Delta_n|x\rangle\langle x|\Delta_{n'}\rangle = \sum_{i=-\infty}^{\infty}\frac{\Delta x}{\Delta x}\text{sinc}(\pi(i-n))\text{sinc}(\pi(i-n')) = \delta_{n,n'}. \tag{D.3}$$

Exponential accuracy of this DVR with the number of grid points N allows for a

diagonal matrix representation of the external potential

$$\langle \Delta_n | V(x) \Delta_{n'} \rangle \equiv V_{nn'} \approx V(x_n) \delta_{n,n'}. \tag{D.4}$$

While the kinetic energy operator in the DVR basis can be written as

$$\begin{aligned} T_{nn'} &\equiv \langle \Delta_n | - \frac{\hbar^2}{2M} \frac{\partial^2}{\partial x^2} | \Delta_{n'} \rangle \\ &= \frac{\hbar^2}{2M\Delta x^2} \begin{cases} \frac{\pi^2}{3}, & n = n' \\ \frac{2(-1)^{n-n'}}{(n-n')^2}, & \text{otherwise} \end{cases} \end{aligned} \tag{D.5}$$

Notice how the kinetic energy matrix is no longer sparse at least in one dimensional problems (tri-diagonal in the case of first-order finite difference scheme) in this representation. One can view this representation as the N-th order finite difference approximation to the second derivative as $N \to \infty$ [184]. However, for three dimensional systems the kinetic energy matrix is block diagonal along each dimension. While finite-order finite difference schemes have sparse kinetic energy matrices, the convergence is only polynomial with the number of grid points. On the other hand, the kinetic energy representation in Eq. (D.5) will have exponential convergence. As pointed out in Ref. [28], another nice advantage of using sinc DVR is the exponential convergence for evaluating integrals of products of eigenfunctions and possibly their corresponding derivatives. Such integrals are relevant to us in obtaining effective Hubbard parameters in Chapter 5.

For three dimensional systems in Cartesian coordinates, the single-particle (or non-interacting) Hamiltonian $\hat{h}$ written in the sinc DVR basis is

$$\begin{aligned} \langle \Delta_x \Delta_y \Delta_z | \hat{h} | \Delta_x^{'} \Delta_y^{'} \Delta_z^{'} \rangle &= \delta_{y,y'} \delta_{z,z'} T_{xx'} + \delta_{x,x'} \delta_{z,z'} T_{yy'} \\ &\quad + \delta_{y,y'} \delta_{x,x'} T_{zz'} + \delta_{x,x'} \delta_{y,y'} \delta_{z,z'} V(x,y,z). \end{aligned} \tag{D.6}$$

Therefore, the Hamiltonian in this representation can be applied to a state vector expanded in the sinc DVR basis using $\mathcal{O}(N_x^2 N_y N_z + N_x N_y^2 N_z + N_x N_y N_z^2)$ operation which is significantly fewer than the $\mathcal{O}(N_x^2 N_y^2 N_z^2)$ operations for a dense matrix representation of $\hat{h}$. We numerically implement the construction as well as exact

diagonalization of Eq. (D.6) for the effective Hubbard parameters in Chapter 5. Convergence properties of the sinc DVR as applied in non-separable Gaussian-type optical potentials are discussed in Ref. [28].

Bibliography

[1] A. Einstein. Quantentheorie des einatomigen idealen gases. *Sitzungsber. Preuss. Akad. Wiss.*, page 261, 1924.

[2] A. Einstein. Quantentheorie des einatomigen idealen gases: Zweite abhandlung. *Sitzungsber. Preuss. Akad. Wiss.*, page 3, 1925.

[3] S. N. Bose. Plancks gesetz und lichtquantenhypothese. *Z. Phys.*, 26:178, 1924.

[4] M. H. Anderson, J. R. Ensher, M. R. Matthews, C. E. Wieman, and E. A. Cornell. Observation of Bose-Einstein Condensation in a Dilute Atomic Vapor. *Science*, 269:198–201, July 1995.

[5] K. B. Davis, M. O. Mewes, M. R. Andrews, N. J. van Druten, D. S. Durfee, D. M. Kurn, and W. Ketterle. Bose-einstein condensation in a gas of sodium atoms. *Phys. Rev. Lett.*, 75:3969–3973, Nov 1995.

[6] I. Bloch, J. Dalibard, and W. Zwerger. Many-body physics with ultracold gases. *Rev. Mod. Phys.*, 80:885, 2008.

[7] H. Feshbach. A unified theory of nuclear reactions. II. *Annals of Physics*, 19:287–313, August 1962.

[8] S. L. Cornish, N. R. Claussen, J. L. Roberts, E. A. Cornell, and C. E. Wieman. Stable ^{85}Rb bose-einstein condensates with widely tunable interactions. *Phys. Rev. Lett.*, 85:1795–1798, Aug 2000.

[9] M. Greiner, O. Mandel, T. Esslinger, T. W. Hänsch, and I. Bloch. Quantum phase transition from a superfluid to a Mott insulator in a gas of ultracold atoms. *Nature*, 415:39–44, January 2002.

[10] M. Greiner, O. Mandel, T. W. Hänsch, and I. Bloch. Collapse and revival of the matter wave field of a Bose-Einstein condensate. *Nature*, 419:51–54, September 2002.

[11] D. Jaksch, C. Bruder, J. I. Cirac, C. W. Gardiner, and P. Zoller. Cold Bosonic Atoms in Optical Lattices. *Physical Review Letters*, 81:3108–3111, October 1998.

[12] T. Grünzweig, A. Hilliard, M. McGovern, and M. F. Andersen. Near-deterministic preparation of a single atom in an optical microtrap. *Nature Phys.*, 6:951–954, December 2010.

[13] A. N. Wenz, G. Zürn, S. Murmann, I. Brouzos, T. Lompe, and S. Jochim. From Few to Many: Observing the Formation of a Fermi Sea One Atom at a Time. *Science*, 342:457–460, October 2013.

[14] S. Murmann, A. Bergschneider, V. M. Klinkhamer, G. Zürn, T. Lompe, and S. Jochim. Two Fermions in a Double Well: Exploring a Fundamental Building Block of the Hubbard Model. *Phys. Rev. Lett.*, 114:080402, Feb 2015.

[15] T. Kinoshita, T. Wenger, and D.S. Weiss. A quantum Newton's cradle. *Nature (London)*, 440:900, 2006.

[16] M. Rigol, V. Dunjko, and M. Olshanii. Thermalization and its mechanism for generic isolated quantum systems. *Nature (London)*, 452:854–858, 2008.

[17] J. G. Cosme and O. Fialko. Thermalization in closed quantum systems: Semi-classical approach. *Phys. Rev. A*, 90:053602, 2014.

[18] J. G. Cosme and O. Fialko. Relaxation dynamics of ultracold bosons in a double-well potential: Thermalization and prethermalization in a nearly integrable model. *Phys. Rev. A*, 92:033607, Sep 2015.

[19] J. G. Cosme, C. Weiss, and J. Brand. Center-of-mass motion as a sensitive convergence test for variational multimode quantum dynamics. *Phys. Rev. A*, 94(4):043603, October 2016.

[20] J. G. Cosme, M. F. Andersen, and J. Brand. Interaction blockade for bosons in an asymmetric double well. *Phys. Rev. A*, 96:013616, Jul 2017.

[21] C. J. Pethick and H. Smith. *Bose-Einstein Condensation in Dilute Gases*. Cambridge University Press, Cambridge, 2008.

[22] E. Fermi. On the Motion of Neutrons in Hydrogenous Substances. *Ricerca Sci.*, 7:13, 1936.

[23] Kerson Huang and C. N. Yang. Quantum-mechanical many-body problem with hard-sphere interaction. *Phys. Rev.*, 105:767–775, Feb 1957.

[24] T. D. Lee, Kerson Huang, and C. N. Yang. Eigenvalues and eigenfunctions of a bose system of hard spheres and its low-temperature properties. *Phys. Rev.*, 106:1135–1145, Jun 1957.

[25] Oliver Penrose and Lars Onsager. Bose-einstein condensation and liquid helium. *Phys. Rev.*, 104:576–584, Nov 1956.

[26] M. A. Garcia-March, D. R. Dounas-Frazer, and L. D. Carr. *Frontiers of Physics*, 7:131–145, 2012.

[27] O. Svelto and D. C. Hanna. *Principles of Lasers*. Plenum Press, New York, 1989.

[28] M. L. Wall, K. R. A. Hazzard, and A. M. Rey. Effective many-body parameters for atoms in nonseparable gaussian optical potentials. *Phys. Rev. A*, 92:013610, Jul 2015.

[29] M. Olshanii. Atomic Scattering in the Presence of an External Confinement and a Gas of Impenetrable Bosons. *Phys. Rev. Lett.*, 81(5):938–941, aug 1998.

[30] H. J. Lipkin, N. Meshkov, and A. J. Glick. Validity of many-body approximation methods for a solvable model:(i). exact solutions and perturbation theory. *Nuclear Physics*, 62(2):188–198, 1965.

[31] J. V. Neumann. Beweis des Ergodensatzes und des H-Theorems in der neuen Mechanik. *Zeitschrift fur Physik*, 57:30–70, January 1929.

[32] L. D'Alessio, Y. Kafri, A. Polkovnikov, and M. Rigol. From quantum chaos and eigenstate thermalization to statistical mechanics and thermodynamics. *Advances in Physics*, 65:239–362, May 2016.

[33] Michael V Berry and Michael Tabor. Level clustering in the regular spectrum. In *Proceedings of the Royal Society of London A: Mathematical, Physical and Engineering Sciences*, volume 356, pages 375–394. The Royal Society, 1977.

[34] O. Bohigas, M. J. Giannoni, and C. Schmit. Characterization of chaotic quantum spectra and universality of level fluctuation laws. *Phys. Rev. Lett.*, 52:1–4, Jan 1984.

[35] T. Guhr, A. Müller-Groeling, and H. A. Weidenmüller. Random-matrix theories in quantum physics: common concepts. *Physics Reports*, 299:189–425, June 1998.

[36] V. Oganesyan and D. A. Huse. Localization of interacting fermions at high temperature. *Phys. Rev. B*, 75:155111, 2007.

[37] Y. Y. Atas, E. Bogomolny, O. Giraud, and G. Roux. Distribution of the Ratio of Consecutive Level Spacings in Random Matrix Ensembles. *Phys. Rev. Lett*, 110:084101, 2013.

[38] J. M. Deutsch. Quantum statistical mechanics in a closed system. *Phys. Rev. A*, 43:2046–2049, Feb 1991.

[39] M. Srednicki. Chaos and quantum thermalization. *Phys. Rev. E*, 50:888–901, Aug 1994.

[40] M. Srednicki. Does Quantum Chaos Explain Quantum Statistical Mechanics? *arXiv:cond-mat/9410046v2*, October 1994.

[41] M. Srednicki. The approach to thermal equilibrium in quantized chaotic systems. *Journal of Physics A Mathematical General*, 32:1163–1175, February 1999.

[42] R. Nandkishore and D. A. Huse. Many-Body Localization and Thermalization in Quantum Statistical Mechanics. *Annual Review of Condensed Matter Physics*, 6:15–38, March 2015.

[43] O. E. Alon, A. I. Streltsov, and L. S. Cederbaum. Multiconfigurational time-dependent Hartree method for bosons: Many-body dynamics of bosonic systems. 77:033613, 2008.

[44] S. Zöllner, H.-D. Meyer, and P. Schmelcher. Few-Boson Dynamics in Double Wells: From Single-Atom to Correlated Pair Tunneling. *Phys. Rev. Lett.*, 100(4):040401, jan 2008.

[45] K. Sakmann, A. I. Streltsov, O. E. Alon, and L. S. Cederbaum. Exact Quantum Dynamics of a Bosonic Josephson Junction. *Phys. Rev. Lett.*, 103:220601, Nov 2009.

[46] K. Sakmann, A. I. Streltsov, O. E. Alon, and L. S. Cederbaum. Quantum dynamics of attractive versus repulsive bosonic Josephson junctions: Bose-Hubbard and full-Hamiltonian results. *Phys. Rev. A*, 82:013620, Jul 2010.

[47] A. I. Streltsov, K. Sakmann, O. E. Alon, and L. S. Cederbaum. Accurate multi-boson long-time dynamics in triple-well periodic traps. *Phys. Rev. A*, 83:043604, Apr 2011.

[48] K. Sakmann, A.I. Streltsov, O.E. Alon, and L.S. Cederbaum. Universality of fragmentation in the Schrödinger dynamics of bosonic Josephson junctions. *Phys. Rev. A*, 89(2):023602, feb 2014.

[49] K. Sakmann, A. I. Streltsov, O. E. Alon, and L. S. Cederbaum. Universality of fragmentation in the Schrödinger dynamics of bosonic Josephson junctions. *Phys. Rev. A*, 89:023602, Feb 2014.

[50] Ioannis Brouzos, Alexej I. Streltsov, Antonio Negretti, Ressa S. Said, Tommaso Caneva, Simone Montangero, and Tommaso Calarco. Quantum speed limit and optimal control of many-boson dynamics. *Phys. Rev. A*, 92:062110, Dec 2015.

[51] S. I. Mistakidis, L. Cao, and P. Schmelcher. Negative-quench-induced excitation dynamics for ultracold bosons in one-dimensional lattices. *Phys. Rev. A*, 91(3):033611, March 2015.

[52] G. M. Koutentakis, S. I. Mistakidis, and P. Schmelcher. Quench-induced resonant tunneling mechanisms of bosons in an optical lattice with harmonic confinement. *Phys. Rev. A*, 95:013617, Jan 2017.

[53] G. M. Koutentakis, S. I. Mistakidis, and P. Schmelcher. Quench-induced resonant tunneling mechanisms of bosons in an optical lattice with harmonic confinement. *Phys. Rev. A*, 95:013617, Jan 2017.

[54] P. B. Blakie, A. S. Bradley, M. J. Davis, R. J. Ballagh, and C. W. Gardiner. Dynamics and statistical mechanics of ultra-cold bose gases using c-field techniques. *Adv. Phys.*, 57(5):363–455, 2008.

[55] A. Polkovnikov. Phase space representation of quantum dynamics. *Ann. Phys.*, 325(8):1790 – 1852, 2010.

[56] E. Wigner. On the quantum correction for thermodynamic equilibrium. *Phys. Rev.*, 40:749–759, Jun 1932.

[57] Q.-Y. He, M. D. Reid, B. Opanchuk, R. Polkinghorne, L. E. C. Rosales-Zárate, and P. D. Drummond. Quantum dynamics in ultracold atomic physics. *Frontiers Phys.*, 7(1):16–30, jan 2012.

[58] A. J. Daley, C. Kollath, U. Schollwöck, and G Vidal. Time-dependent density-matrix renormalization-group using adaptive effective Hilbert spaces. *J. of Stat. Mech.*, 2004(04):P04005, 2004.

[59] H.-D. Meyer, U. Manthe, and L.S. Cederbaum. The multi-configurational time-dependent Hartree approach. *Chem. Phys. Lett.*, 165(1):73, jan 1990.

[60] M. H. Beck, A. Jäckle, G. A. Worth, and H.-D. H.-D. Meyer. The multiconfiguration time-dependent Hartree (MCTDH) method: a highly efficient algorithm for propagating wavepackets. *Physics Reports*, 324:1–105, January 2000.

[61] J. Caillat, J. Zanghellini, M. Kitzler, O. Koch, W. Kreuzer, and A. Scrinzi. Correlated multielectron systems in strong laser fields: A multiconfiguration time-dependent Hartree-Fock approach. *Phys. Rev. A*, 71(1):012712, jan 2005.

[62] D. K. Faust and W. P. Reinhardt. Analysis of a Bose-Einstein Condensate Double-Well Atom Interferometer. *Phys. Rev. Lett.*, 105(24):240404, dec 2010.

[63] L. Pitaevskii and S. Stringari. *Bose-Einstein Condensation*. Clarendon, Oxford, 2003.

[64] W. Kohn. Cyclotron Resonance and de Haas-van Alphen Oscillations of an Interacting Electron Gas. *Phys. Rev.*, 123(4):1242, aug 1961.

[65] G.W. Gibbons and C.N. Pope. Kohn's theorem, Larmor's equivalence principle and the Newton-Hooke group. *Ann. Phys. (N. Y).*, 326(7):1760, jul 2011.

[66] L. Khaykovich, F. Schreck, G. Ferrari, T. Bourdel, J. Cubizolles, L. D. Carr, Y. Castin, and C. Salomon. Formation of a matter-wave bright soliton. *Science*, 296:1290, 2002.

[67] K. E. Strecker, G. B. Partridge, A. G. Truscott, and R. G. Hulet. Formation and propagation of matter-wave soliton trains. *Nature (London)*, 417:150, 2002.

[68] P. Medley, M. A. Minar, N. C. Cizek, D. Berryrieser, and M. A. Kasevich. Evaporative production of bright atomic solitons. *Phys. Rev. Lett.*, 112:060401, 2014.

[69] G. D. McDonald, C. C. N. Kuhn, K. S. Hardman, S. Bennetts, P. J. Everitt, P. A. Altin, J. E. Debs, J. D. Close, and N. P. Robins. Bright solitonic matter-wave interferometer. *Phys. Rev. Lett.*, 113:013002, 2014.

[70] J. H. V. Nguyen, P. Dyke, D. Luo, B. A. Malomed, and R. G. Hulet. Collisions of matter-wave solitons. *Nat. Phys.*, 10:918, 2014.

[71] A. L. Marchant, T. P. Billam, M. M. H. Yu, A. Rakonjac, J. L. Helm, J. Polo, C. Weiss, S. A. Gardiner, and S. L. Cornish. Quantum reflection of bright solitary matter-waves from a narrow attractive potential. *ArXiv e-prints*, July 2015.

[72] Y. Castin and C. Herzog. Bose-Einstein condensates in symmetry breaking states. *C. R. Acad. Sci. Paris, Ser. IV*, 2:419, 2001.

[73] J. B. McGuire. Study of Exactly Soluble One-Dimensional N-Body Problems. *J. Math. Phys.*, 5:622, 1964.

[74] F. Calogero and A. Degasperis. Comparison between the exact and Hartree solutions of a one-dimensional many-body problem. *Phys. Rev. A*, 11:265, 1975.

[75] A. I. Streltsov, O. E. Alon, and L. S. Cederbaum. Formation and Dynamics of Many-Boson Fragmented States in One-Dimensional Attractive Ultracold Gases. *Phys. Rev. Lett.*, 100(13):130401, apr 2008.

[76] A. I. Streltsov, O. E. Alon, and L. S. Cederbaum. Scattering of an attractive Bose-Einstein condensate from a barrier: Formation of quantum superposition states. *Phys. Rev. A*, 80:043616, Oct 2009.

[77] A. I. Streltsov, O. E. Alon, and L. S. Cederbaum. Swift loss of coherence of soliton trains in attractive Bose-Einstein condensates. *Phys. Rev. Lett.*, 106:240401, 2011.

[78] L. Cao, S. Krönke, O. Vendrell, and P. Schmelcher. The multi-layer multi-configuration time-dependent Hartree method for bosons: Theory, implementation, and applications. *J. Chem. Phys.*, 139(13):134103, oct 2013.

[79] S. Klaiman and O. E. Alon. Variance as a sensitive probe of correlations. *Phys. Rev. A*, 91:063613, Jun 2015.

[80] X.-J. Liu, H. Hu, and P. D. Drummond. Three attractively interacting fermions in a harmonic trap: Exact solution, ferromagnetism, and high-temperature thermodynamics. *Phys. Rev. A*, 82:023619, Aug 2010.

[81] Thomas Busch, Berthold-Georg Englert, Kazimierz Rzazewski, and Martin Wilkens. Two cold atoms in a harmonic trap. *Found. Phys.*, 28:549, 1998.

[82] S. Flügge. *Rechenmethoden der Quantentheorie*. Springer, Berlin, 1990.

[83] T. Ernst and J. Brand. `http://github.com/Qiwib/qiwib`, 2011.

[84] A. I. Streltsov and O. I. Streltsova. MCTDHB-Lab v1.5. `http://bbb.jinr.ru`, 2015.

[85] R. Beinke, S. Klaiman, L. S. Cederbaum, A. I. Streltsov, and O. E. Alon. Many-body tunneling dynamics of Bose-Einstein condensates and vortex states in two spatial dimensions. *ArXiv e-prints*, 2015.

[86] S. I. Mistakidis, L. Cao, and P. Schmelcher. Negative-quench-induced excitation dynamics for ultracold bosons in one-dimensional lattices. *Phys. Rev. A*, 91(3):033611, March 2015.

[87] J. M. Schurer, A. Negretti, and P. Schmelcher. Capture dynamics of ultracold atoms in the presence of an impurity ion. *New J. Phys.*, 17(8):083024, aug 2015.

[88] K.-S. Lee and U. R. Fischer. Truncated many-body dynamics of interacting bosons: A variational principle with error monitoring. *Int. J. Mod. Phys. B*, 28:1550021, November 2014.

[89] U. Manthe, H.-D. Meyer, and L. S. Cederbaum. Wave-packet dynamics within the multiconfiguration Hartree framework: General aspects and application to NOCl. *J. Chem. Phys.*, 97(5):3199, 1992.

[90] A. U. J. Lode, K. Sakmann, O. E. Alon, L. S. Cederbaum, and A. I. Streltsov. Numerically exact quantum dynamics of bosons with time-dependent interactions of harmonic type. *Phys. Rev. A*, 86:063606, Dec 2012.

[91] E. H. Lieb and W. Liniger. Exact Analysis of an Interacting Bose Gas. I. The General Solution and the Ground State. *Phys. Rev.*, 130:1605, 1963.

[92] R. Schmitz, S. Krönke, L. Cao, and P. Schmelcher. Quantum breathing dynamics of ultracold bosons in one-dimensional harmonic traps: Unraveling the pathway from few- to many-body systems. *Phys. Rev. A*, 88:043601, Oct 2013.

[93] T. Grining, M. Tomza, M. Lesiuk, M. Przybytek, M. Musiał, P. Massignan, M. Lewenstein, and R. Moszynski. Many interacting fermions in a one-dimensional harmonic trap: a quantum-chemical treatment. *New J. Phys.*, 17(11):115001, November 2015.

[94] A. U. J. Lode, A. I. Streltsov, O. E. Alon, H.-D. Meyer, and L. S. Cederbaum. Exact decay and tunnelling dynamics of interacting few-boson systems. *J. Phys. B At. Mol. Opt. Phys.*, 42(4):044018, feb 2009.

[95] A. U. J. Lode, A. I. Streltsov, K. Sakmann, O. E. Alon, and L. S. Cederbaum. How an interacting many-body system tunnels through a potential barrier to open space. *Proc. Natl. Acad. Sci.*, 109(34):13521, aug 2012.

[96] A. M. Kaufman, B. J. Lester, and C. A. Regal. Cooling a Single Atom in an Optical Tweezer to Its Quantum Ground State. *Phys. Rev. X*, 2:041014, Nov 2012.

[97] P. Sompet, Y. H. Fung, E. Schwartz, M. D. J. Hunter, J. Phrompao, and M. F. Andersen. Zeeman–Insensitive Cooling of a Single Atom to its 2D Quantum Ground State. *ArXiv e-prints*, December 2016.

[98] A. M. Kaufman, B. J. Lester, C. M. Reynolds, M. L. Wall, M. Foss-Feig, K. R. A. Hazzard, A. M. Rey, and C. A. Regal. Two-particle quantum interference in tunnel-coupled optical tweezers. *Science*, 345(6194):306–309, 2014.

[99] J. Lambe and R. C. Jaklevic. Charge-quantization studies using a tunnel capacitor. *Phys. Rev. Lett.*, 22(25):1371, 1969.

[100] D. V. Averin and K. K. Likharev. Coulomb blockade of single-electron tunneling, and coherent oscillations in small tunnel junctions. *J. Low Temp. Phys.*, 62:345–373, February 1986.

[101] U. Meirav, M. A. Kastner, M. Heiblum, and S. J. Wind. One-dimensional electron gas in GaAs: Periodic conductance oscillations as a function of density. *Phys. Rev. B*, 40:5871–5874, September 1989.

[102] S. M. Reimann and M. Manninen. Electronic structure of quantum dots. *Rev. Mod. Phys.*, 74:1283–1342, November 2002.

[103] M. D. Lukin, M. Fleischhauer, R. Cote, L. M. Duan, D. Jaksch, J. I. Cirac, and P. Zoller. Dipole Blockade and Quantum Information Processing in Mesoscopic Atomic Ensembles. *Phys. Rev. Lett.*, 87:037901, Jun 2001.

[104] T. A. Johnson, E. Urban, T. Henage, L. Isenhower, D. D. Yavuz, T. G. Walker, and M. Saffman. Rabi Oscillations between Ground and Rydberg States with Dipole-Dipole Atomic Interactions. *Phys. Rev. Lett.*, 100(11):113003, March 2008.

[105] E. Urban, T. A. Johnson, T. Henage, L. Isenhower, D. D. Yavuz, T. G. Walker, and M. Saffman. Observation of Rydberg blockade between two atoms. *Nature Phys.*, 5:110–114, February 2009.

[106] M. Saffman, T. G. Walker, and K. Mølmer. Quantum information with Rydberg atoms. *Rev. Mod. Phys.*, 82:2313–2363, July 2010.

[107] A. Browaeys, D. Barredo, and T. Lahaye. Experimental investigations of dipole-dipole interactions between a few Rydberg atoms. *J. Phys. B*, 49(15):152001, August 2016.

[108] A. Micheli, A. J. Daley, D. Jaksch, and P. Zoller. Single Atom Transistor in a 1D Optical Lattice. *Phys. Rev. Lett.*, 93(14):140408, October 2004.

[109] K. Capelle, M. Borgh, K. Kärkkäinen, and S. M. Reimann. Energy Gaps and Interaction Blockade in Confined Quantum Systems. *Phys. Rev. Lett.*, 99(1):010402, July 2007.

[110] B. T. Seaman, M. Krämer, D. Z. Anderson, and M. J. Holland. Atomtronics: Ultracold-atom analogs of electronic devices. *Phys. Rev. A*, 75(2):023615, February 2007.

[111] D. R. Dounas-Frazer, A. M. Hermundstad, and L. D. Carr. Ultracold Bosons in a Tilted Multilevel Double-Well Potential. *Phys. Rev. Lett.*, 99(20):200402, November 2007.

[112] C. Lee, L.-B. Fu, and Y. S. Kivshar. Many-body quantum coherence and interaction blockade in Josephson-linked Bose-Einstein condensates. *Europhys. Lett.*, 81:60006, March 2008.

[113] P. Schlagheck, F. Malet, J. C. Cremon, and S. M. Reimann. Transport and interaction blockade of cold bosonic atoms in a triple-well potential. *New J. Phys.*, 12(6):065020, June 2010.

[114] P. Cheinet, S. Trotzky, M. Feld, U. Schnorrberger, M. Moreno-Cardoner, S. Fölling, and I. Bloch. Counting atoms using interaction blockade in an optical superlattice. *Phys. Rev. Lett.*, 101:090404, Aug 2008.

[115] P. M. Preiss, R. Ma, M. E. Tai, J. Simon, and M. Greiner. Quantum gas microscopy with spin, atom-number, and multilayer readout. *Phys. Rev. A*, 91:041602, Apr 2015.

[116] F. Meinert, M. J. Mark, E. Kirilov, K. Lauber, P. Weinmann, A. J. Daley, and H.-C. Nägerl. Quantum Quench in an Atomic One-Dimensional Ising Chain. *Phys. Rev. Lett.*, 111:053003, Jul 2013.

[117] P. A. Altin, N. P. Robins, D. Döring, J. E. Debs, R. Poldy, C. Figl, and J. D. Close. ^{85}Rb tunable-interaction Bose-Einstein condensate machine. *Review of Scientific Instruments*, 81(6):063103–063103, June 2010.

[118] C. Chin, R. Grimm, P. Julienne, and E. Tiesinga. Feshbach resonances in ultracold gases. *Rev. Mod. Phys.*, 82:1225–1286, Apr 2010.

[119] M. Rontani, G. Eriksson, S. Åberg, and S. M. Reimann. On the renormalization of contact interactions for the configuration-interaction method in two dimensions. *J. Phys. B*, 50(6):065301, 2017.

[120] V. J. Bolsinger, S. Krönke, and P. Schmelcher. Beyond mean-field dynamics of ultra-cold bosonic atoms in higher dimensions: facing the challenges with a multi-configurational approach. *J. Phys. B*, 50(3):034003, February 2017.

[121] A. Smerzi, S. Fantoni, S. Giovanazzi, and S. R. Shenoy. *Phys. Rev. Lett.*, 79:4950, 1997.

[122] G. J. Milburn, J. Corney, E. M. Wright, and D. F. Walls. *Phys. Rev. A*, 55:4318, 1997.

[123] M. Albiez, R. Gati, J. Folling, S. Hunsmann, M. Cristiani, and M. K. Oberthaler. *Phys. Rev. Lett.*, 95:010402, 2005.

[124] S. Levy, E. Lahoud, I. Shomroni, and J. Steinhauer. *Nature*, 449:579, 2007.

[125] D. Masiello, S. B. McKagan, and W. P. Reinhardt. Multiconfigurational hartree-fock theory for identical bosons in a double well. *Phys. Rev. A*, 72:063624, Dec 2005.

[126] J. R. Armstrong, S. Åberg, S. M. Reimann, and V. G. Zelevinsky. Complexity of quantum states in the two-dimensional pairing model. *Phys. Rev. E*, 86(6):066204, December 2012.

[127] P. D'Amico and M. Rontani. Pairing of a few Fermi atoms in one dimension. *Phys. Rev. A*, 91(4):043610, April 2015.

[128] D. Barredo, S. de Léséleuc, V. Lienhard, T. Lahaye, and A. Browaeys. An atom-by-atom assembler of defect-free arbitrary two-dimensional atomic arrays. *Science*, 354:1021–1023, November 2016.

[129] M. Endres, H. Bernien, A. Keesling, H. Levine, E. R. Anschuetz, A. Krajenbrink, C. Senko, V. Vuletic, M. Greiner, and M. D. Lukin. Atom-by-atom assembly of defect-free one-dimensional cold atom arrays. *Science*, 354:1024–1027, November 2016.

[130] K. A. Matveev and L. I. Glazman. Coulomb blockade of activated conduction. *Phys. Rev. B*, 54:10339–10341, Oct 1996.

[131] Anatoli Polkovnikov, Krishnendu Sengupta, Alessandro Silva, and Mukund Vengalattore. Colloquium: Nonequilibrium dynamics of closed interacting quantum systems. *Reviews of Modern Physics*, 83(3):863–883, 2011.

[132] M. Rigol and M. Srednicki. Alternatives to Eigenstate Thermalization. *Physical Review Letters*, 108(11):110601, March 2012.

[133] M. Rigol. Quantum quenches and thermalization in one-dimensional fermionic systems. *Phys. Rev. A*, 80:053607, Nov 2009.

[134] L. F. Santos and M. Rigol. Localization and the effects of symmetries in the thermalization properties of one-dimensional quantum systems. *Phys. Rev. E*, 82:031130, Sep 2010.

[135] S. Genway, A. F. Ho, and D. K. K. Lee. Thermalization of local observables in small Hubbard lattices. *Physical Review A*, 86(2):023609, August 2012.

[136] R. Steinigeweg, A. Khodja, H. Niemeyer, C. Gogolin, and J. Gemmer. Pushing the Limits of the Eigenstate Thermalization Hypothesis towards Mesoscopic Quantum Systems. *Physical Review Letters*, 112(13):130403, April 2014.

[137] S. Sorg, L. Vidmar, L. Pollet, and F. Heidrich-Meisner. *Physical Review A*, 90:033606, 2014.

[138] M. Rigol. *Physical Review Letters*, 112:170601, 2014.

[139] Hyungwon Kim, Tatsuhiko N. Ikeda, and David A. Huse. Testing whether all eigenstates obey the eigenstate thermalization hypothesis. *Phys. Rev. E*, 90:052105, Nov 2014.

[140] Abdellah Khodja, Robin Steinigeweg, and Jochen Gemmer. Relevance of the eigenstate thermalization hypothesis for thermal relaxation. *Phys. Rev. E*, 91:012120, Jan 2015.

[141] Vincenzo Alba. *Physical Review B*, 91:155123, 2015.

[142] Michael Moeckel and Stefan Kehrein. Interaction quench in the hubbard model. *Phys. Rev. Lett.*, 100:175702, May 2008.

[143] Marcus Kollar, F. Alexander Wolf, and Martin Eckstein. Generalized Gibbs ensemble prediction of prethermalization plateaus and their relation to nonthermal steady states in integrable systems. *Physical Review B*, 84(5):054304, 2011.

[144] M. Gring, M. Kuhnert, T. Langen, T. Kitagawa, B. Rauer, M. Schreitl, I. Mazets, D. A. Smith, E. Demler, and J. Schmiedmayer. *Science*, 337:1318–1322, 2012.

[145] Matteo Marcuzzi, Jamir Marino, Andrea Gambassi, and Alessandro Silva. Prethermalization in a nonintegrable quantum spin chain after a quench. *Phys. Rev. Lett.*, 111:197203, Nov 2013.

[146] D Adu Smith, M Gring, T Langen, M Kuhnert, B Rauer, R Geiger, T Kitagawa, I Mazets, E Demler, and J Schmiedmayer. Prethermalization revealed by the relaxation dynamics of full distribution functions. *New Journal of Physics*, 15(7):075011, 2013.

[147] Zhe Xuan Gong and L. M. Duan. Prethermalization and dynamic phase transition in an isolated trapped ion spin chain. *New Journal of Physics*, 15(11):113051, 2013.

[148] F. H. L. Essler, S. Kehrein, S. R. Manmana, and N. J. Robinson. Quench dynamics in a model with tuneable integrability breaking. *Phys. Rev. B*, 89:165104, Apr 2014.

[149] N. Nessi, A. Iucci, and M. A. Cazalilla. Quantum quench and prethermalization dynamics in a two-dimensional fermi gas with long-range interactions. *Phys. Rev. Lett.*, 113:210402, Nov 2014.

[150] I. Salazar Landea and N. Nessi. Prethermalization and glassiness in the bosonic Hubbard model. *Physical Review A*, 91(6):063601, 2015.

[151] B. Bertini, F. H. L. Essler, S. Groha, and N. J. Robinson. Prethermalization and thermalization in models with weak integrability breaking. *ArXiv e-prints*, 2015.

[152] T. Langen, S. Erne, R. Geiger, B. Rauer, T. Schweigler, M. Kuhnert, W. Rohringer, I. E. Mazets, T. Gasenzer, and J. Schmiedmayer. Experimental observation of a generalized Gibbs ensemble. *Science*, 348:207–211, 2015.

[153] V. V. Flambaum and F. M. Izrailev. Statistical theory of finite Fermi systems based on the structure of chaotic eigenstates. *Physical Review E*, 56:5144–5159, November 1997.

[154] L. F. Santos, F. Borgonovi, and F. M. Izrailev. Chaos and Statistical Relaxation in Quantum Systems of Interacting Particles. *Phys. Rev. Lett.*, 108:094102, Mar 2012.

[155] L. F. Santos, F. Borgonovi, and F. M. Izrailev. Onset of chaos and relaxation in isolated systems of interacting spins: Energy shell approach. *Phys. Rev. E*, 85:036209, Mar 2012.

[156] E. J. Torres-Herrera and L. F. Santos. Effects of the interplay between initial state and Hamiltonian on the thermalization of isolated quantum many-body systems. *Physical Review E*, 88(4):042121, October 2013.

[157] O. Fialko and D. W. Hallwood. Isolated quantum heat engine. *Physical Review Letters*, 108:085303, 2012.

[158] L. F. Santos, A. Polkovnikov, and M. Rigol. Weak and strong typicality in quantum systems. *Physical Review E*, 86(1):010102, July 2012.

[159] S. Khlebnikov and M. Kruczenski. Locality, entanglement, and thermalization of isolated quantum systems. *Physical Review E*, 90(5):050101, November 2014.

[160] Liangsheng Zhang, Hyungwon Kim, and David A. Huse. Thermalization of entanglement. *Phys. Rev. E*, 91:062128, Jun 2015.

[161] S. Aubry, S. Flach, K. Kladko, and E. Olbrich. Manifestation of classical bifurcation in the spectrum of the integrable quantum dimer. *Phys. Rev. Lett.*, 76:1607–1610, Mar 1996.

[162] J. Gillet, M. A. Garcia-March, Th. Busch, and F. Sols. Tunneling, self-trapping, and manipulation of higher modes of a Bose-Einstein condensate in a double well. *Phys. Rev. A*, 89:023614, Feb 2014.

[163] D. Hennig, H. Gabriel, M. F. Jørgensen, P. L. Christiansen, and C. B. Clausen. Homoclinic chaos in the discrete self-trapping trimer. *Phys. Rev. E*, 51:2870–2876, Apr 1995.

[164] S. Flach and V. Fleurov. Tunnelling in the nonintegrable trimer-a step towards quantum breathers. *Journal of Physics: Condensed Matter*, 9(33):7039, 1997.

[165] T. A. Brody, J. Flores, J. B. French, P. A. Mello, A. Pandey, and S. S. M. Wong. Random-matrix physics: spectrum and strength fluctuations. *Rev. Mod. Phys.*, 53:385–479, Jul 1981.

[166] Gilles Montambaux, Didier Poilblanc, Jean Bellissard, and Clément Sire. Quantum chaos in spin-fermion models. *Phys. Rev. Lett.*, 70:497–500, Jan 1993.

[167] C. Kollath, G. Roux, G. Biroli, and A. M. Lauchli. Statistical properties of the spectrum of the extended BoseHubbard model. *J. Stat. Mech.*, 2010:P08011, 2010.

[168] M. Rigol and L. F. Santos. Quantum chaos and thermalization in gapped systems. *Phys. Rev. A*, 82:011604, Jul 2010.

[169] Jesse Mumford, Jonas Larson, and D. H. J. O'Dell. Impurity in a bosonic Josephson junction: Swallowtail loops, chaos, self-trapping, and Dicke model. *Physical Review A*, 89(2):023620, 2014.

[170] G. Casati, B. V. Chirikov, I. Guarneri, and F. M. Izrailev. Band-random-matrix model for quantum localization in conservative systems. *Physical Review E*, 48:R1613–R1616, September 1993.

[171] G. Casati, B. V. Chirikov, I. Guarneri, and F. M. Izrailev. Quantum ergodicity and localization in conservative systems: the Wigner band random matrix model. *Physics Letters A*, 223:430–435, February 1996.

[172] E. J. Torres-Herrera and L. F. Santos. Nonexponential fidelity decay in isolated interacting quantum systems. *Physical Review A*, 90(3):033623, September 2014.

[173] V. V. Flambaum and F. M. Izrailev. Unconventional decay law for excited states in closed many-body systems. *Physical Review E*, 64(2):026124, August 2001.

[174] F. M. Izrailev and A. Castañeda Mendoza. Return probability: Exponential versus Gaussian decay. *Physical Letters A*, 350:355, 2006.

[175] E. J. Torres-Herrera, M. Vyas, and L. F. Santos. General features of the relaxation dynamics of interacting quantum systems. *New Journal of Physics*, 16(6):063010, June 2014.

[176] L. F. Santos, A. Polkovnikov, and M. Rigol. Entropy of Isolated Quantum Systems after a Quench. *Physical Review Letters*, 107(4):040601, July 2011.

[177] Giulio Biroli, Corinna Kollath, and Andreas M. Läuchli. Effect of rare fluctuations on the thermalization of isolated quantum systems. *Phys. Rev. Lett.*, 105:250401, Dec 2010.

[178] M. K. Olsen and A. S. Bradley. Numerical representation of quantum states in the positive-P and Wigner representations. *Opt. Commun.*, 282(19):3924 – 3929, 2009.

[179] A. Altland and F. Haake. Quantum chaos and effective thermalization. *Phys. Rev. Lett.*, 108(7):073601, 2012.

[180] A. Altland and F. Haake. Equilibration and macroscopic quantum fluctuations in the dicke model. *New J. Phys.*, 14(7):073011, 2012.

[181] S. Goldstein, J. L. Lebowitz, R. Tumulka, and N. Zanghì. Canonical Typicality. *Physical Review Letters*, 96(5):050403, February 2006.

[182] S. Popescu, A. J. Short, and A. Winter. Entanglement and the foundations of statistical mechanics. *Nature Physics*, 2:754–758, 2006.

[183] R. G. Littlejohn, M. Cargo, T. Carrington, K. A. Mitchell, and B. Poirier. A general framework for discrete variable representation basis sets. *The Journal of Chemical Physics*, 116:8691–8703, May 2002.

[184] D. T. Colbert and W. H. Miller. A novel discrete variable representation for quantum mechanical reactive scattering via the S-matrix Kohn method. *The Journal of Chemical Physics*, 96:1982–1991, February 1992.

DRC 16

MASSEY UNIVERSITY
GRADUATE RESEARCH SCHOOL

STATEMENT OF CONTRIBUTION
TO DOCTORAL THESIS CONTAINING PUBLICATIONS

(To appear at the end of each thesis chapter/section/appendix submitted as an article/paper or collected as an appendix at the end of the thesis)

We, the candidate and the candidate's Principal Supervisor, certify that all co-authors have consented to their work being included in the thesis and they have accepted the candidate's contribution as indicated below in the *Statement of Originality*.

Name of Candidate: Jayson G. Cosme

Name/Title of Principal Supervisor: Prof. Joachim Brand

Name of Published Research Output and full reference:

Center-of-mass motion as a sensitive convergence test for variational multi-mode quantum dynamics, Physical Review A, 94, 043603, (2016).

In which Chapter is the Published Work: Chapter 4

Please indicate either:

- The percentage of the Published Work that was contributed by the candidate:

  and / or

- Describe the contribution that the candidate has made to the Published Work:

1. Performed all of the numerical simulations
2. Prepared all of the figures
3. Major contributions in writing the paper

Candidate's Signature — 28 June 2017 — Date

Principal Supervisor's signature — 28 June 2017 — Date

GRS Version 3– 16 September 2011

DRC 16

MASSEY UNIVERSITY
GRADUATE RESEARCH SCHOOL

STATEMENT OF CONTRIBUTION
TO DOCTORAL THESIS CONTAINING PUBLICATIONS

(To appear at the end of each thesis chapter/section/appendix submitted as an article/paper or collected as an appendix at the end of the thesis)

We, the candidate and the candidate's Principal Supervisor, certify that all co-authors have consented to their work being included in the thesis and they have accepted the candidate's contribution as indicated below in the *Statement of Originality*.

Name of Candidate: Jayson G. Cosme

Name/Title of Principal Supervisor: Prof. Joachim Brand

Name of Published Research Output and full reference:

Interaction blockade for bosons in an asymmetric double well, arXiv:1704.06437, (2017). (in press for Physical Review A)

In which Chapter is the Published Work: Chapter 5

Please indicate either:

- The percentage of the Published Work that was contributed by the candidate:
  and / or
- Describe the contribution that the candidate has made to the Published Work:

1. Performed all of the numerical simulations
2. Prepared all of the figures
3. Major contributions in writing the paper

Candidate's Signature — 28 June 2017 — Date

Principal Supervisor's signature — 28 June 2017 — Date

GRS Version 3– 16 September 2011

DRC 16

MASSEY UNIVERSITY
GRADUATE RESEARCH SCHOOL

STATEMENT OF CONTRIBUTION
TO DOCTORAL THESIS CONTAINING PUBLICATIONS

(To appear at the end of each thesis chapter/section/appendix submitted as an article/paper or collected as an appendix at the end of the thesis)

We, the candidate and the candidate's Principal Supervisor, certify that all co-authors have consented to their work being included in the thesis and they have accepted the candidate's contribution as indicated below in the *Statement of Originality*.

Name of Candidate: Jayson G. Cosme

Name/Title of Principal Supervisor: Prof. Joachim Brand

Name of Published Research Output and full reference:

J. G. Cosme, O. Fialko, Relaxation dynamics of ultracold bosons in a double-well potential: Thermalization and prethermalization in a nearly integrable model, Physical Review A, 92, 033607, (2015).

In which Chapter is the Published Work: Chapter 6

Please indicate either:

- The percentage of the Published Work that was contributed by the candidate:
  and / or
- Describe the contribution that the candidate has made to the Published Work:

1. Performed all of the numerical simulations
2. Wrote most of the paper
3. Prepared all of the figures except for one

Candidate's Signature — Date: 28 June 2017

Principal Supervisor's signature — Date: 28 June 2017

GRS Version 3– 16 September 2011

DRC 16

MASSEY UNIVERSITY
GRADUATE RESEARCH SCHOOL

STATEMENT OF CONTRIBUTION
TO DOCTORAL THESIS CONTAINING PUBLICATIONS

(To appear at the end of each thesis chapter/section/appendix submitted as an article/paper or collected as an appendix at the end of the thesis)

We, the candidate and the candidate's Principal Supervisor, certify that all co-authors have consented to their work being included in the thesis and they have accepted the candidate's contribution as indicated below in the *Statement of Originality*.

Name of Candidate: Jayson G. Cosme

Name/Title of Principal Supervisor: Prof. Joachim Brand

Name of Published Research Output and full reference:

J. G. Cosme, O. Fialko, Thermalization in closed quantum systems: Semiclassical approach, Physical Review A, 90, 053602, (2014).

In which Chapter is the Published Work: Chapter 7

Please indicate either:

- The percentage of the Published Work that was contributed by the candidate:
  and / or
- Describe the contribution that the candidate has made to the Published Work:

1. Performed all of the numerical simulations
2. Prepared all of the figures except for one
3. Major contributions in writing the paper

Candidate's Signature — 28 June 2017 — Date

Principal Supervisor's signature — 28 June 2017 — Date

GRS Version 3– 16 September 2011